IMAGE RECONSTRUCTION AND GEOMETRICAL MODELING OF BONE CROSS SECTIONS FROM LIMITED ANGLE DUAL ENERGY PROJECTION DATA

by

Alia S. Khaled

A dissertation submitted to The Johns Hopkins University in conformity with the requirements for the degree of Doctor of Philosophy.

Baltimore, Maryland

July, 2014

© 2014 Alia Khaled

All rights reserved

Abstract

Osteoporosis, the most common bone disease is characterized by reduced mechanical strength leading to increased bone fragility and fracture. Because susceptible bones tend to be less dense, clinical diagnosis is currently based on bone density measured typically by Dual-Energy X-ray Absorptiometry (DXA) or Quantitative Computed Tomography (QCT). Unfortunately, density criteria identify less than half of people at risk of osteoporotic fracture and do not adequately characterize the mechanical basis of fracture susceptibility. Identification of fragility could be greatly improved by the use of advanced 3D mechanical engineering analysis based on CT data. CT scanners, however, are expensive and its radiation doses are too high for routine screening of asymptomatic populations. To address these issues, a low dose multi-projection DXA scanner system is proposed that can develop a valid bone model for mechanical analysis from limited angle dual energy projection data. The proposed system presents multiple technical challenges addressed by this dissertation.

The technical approach is based on image reconstruction constrained to three DXA distinguishable tissues present in human extremities: bone, adipose and lean tissues. Because DXA principles can discriminate only two tissues at once, we developed an algorithm to estimate the missing tissues in regions where three tissues are present. Next, using a small number of DXA projections over a rotational angle of 90˚ an algorithm was developed to reconstruct high quality discrete cross-sections. We can then construct 3D models of an extremity from a stack of multiple 2D DXA images to perform a 3D mechanical analysis.

A critical aspect of the methods developed in this dissertation is the application of engineering analyses to 2D and 3D bone data. To demonstrate feasibility, engineering analysis was applied to previously acquired DXA and CT data from several clinical research studies of the femoral neck.

The methods developed in this work, together with the reported applications in bone studies, constitute a frame work wherein low-dose imaging is combined with geometrical modeling to provide a more rational alternative to existing bone-density techniques, both in patient safety and analysis accuracy. The proposed methods could have many applications in the study of osteoporosis.

Advisor and first reader: Benjamin M. W. Tsui, A.M., Ph.D.

Russell H. Morgan Professor of Radiology, Department of Radiology And Radiological Sciences, School of Medicine, Johns Hopkins University

Second reader: Thomas J. Beck, Sc.D.

Department of Radiology And Radiological Sciences, School of Medicine, Johns Hopkins University.

To my parents, my husband Refaat and my son Yusuf ..

Acknowledgements

First of all I thank Allah the most merciful, and the most gracious.

I would like to express thanks to everyone who has helped me during my studies and research. I am grateful to Prof. Benjamin Tsui and Dr. Thomas J. Beck, my advisors, for trusting me and for strong support during my PhD work. Without their patience, invaluable assistance and encouragement, constructive and valuable comments, this dissertation would not have been possible.

My thanks are due to Prof. Gerard Meyer for his valuable time, useful discussions and suggestions to improve this work. Special thanks to Dr. Katsuyuki Taguchi from whom I have learned a lot on the scientific and professional levels.

I would like to thank my colleagues in the Division of Medical Imaging Physics (DMIP) for useful discussions and thoughtful insights during the regular DMIP seminar sessions that were of great help to me.

I also wish to thank Debbie Race, the senior academic program coordinator in Electrical and Computer Engineering department for all the help she provided.

Finally, my special thanks to my family for their love, care, cooperation and continuous support.

Table of Contents

Abstract ..... **ii**

Acknowledgements ..... **v**

List of Tables ..... **ix**

List of Figures ..... **x**

Abbreviations ..... **xiv**

1 Introduction **1**

1.1. Osteoporosis 1

1.2. The role of engineering analysis in osteoporosis 2

1.3. Dissertation Contributions 3

1.3.1. Image reconstruction from limited number of DXA projections 3

1.3.2. Material decomposition of bone cross sections from limited number of DXA projections 3

1.3.3. Geometrically-equivalent models of bone cross sections 4

1.3.4. Clinical studies using different modalities 4

1.4. Dissertation Organization 5

2 Background **7**

2.1. Bone anatomy 7

2.2. Bone remodeling and modeling 8

2.3. Bone diseases 9

2.4. Measuring bone density 9

2.4.1. Dual Energy X-ray Absorptiometry (DXA) 11

2.4.2. Quantitative Computed Tomography (QCT) 15

3 Geometrically-Equivalent Models of Bone Cross Sections **17**

3.1. Background 17

3.2. Materials and Methods 20

3.2.1. Subjects 20

3.2.2. Preprocessing 21

3.2.3. Boundary Detection 21
3.2.4. Separate Shell and Core 23
3.2.5. Shell GEM 24
3.2.6. Finite Strip Model (FSM) 26
3.2.7. Whole GEM 26
3.2.8. Quality Indices 28
3.3. Results 28
3.4. Discussion 34

4 Image Reconstruction from Limited Number of DXA Projections 37
4.1. Background 37
4.2. Methods 40
4.2.1. ART overview 40
4.2.2. DART Algorithm 42
4.2.3. SBART Algorithm 44
4.2.4. GC-SBART Algorithm 47
4.3. Simulations 50
4.3.1. Projections Simulation 50
4.3.2. Image Reconstruction 50
4.3.3. Quality Indices 52
4.4. Results 53
4.5. Discussion 63

5 Material Decomposition of Bone Cross Sections from Limited Number of DXA Projections 67
5.1. Background 67
5.2. Methods 72
5.2.1. Problem Formulation 72
5.2.2. Area Constraint 74
5.3. Simulations 77
5.3.1. Simulations of Projections 77
5.3.2. Simulations to derive the relationship between different tissues and basis materials 82
5.3.3. Optimization Method 87
5.3.4. Image Reconstruction 87

5.3.5. Quality Indices 87
5.4. Results 88
5.5. Discussion 102

6 Femoral Neck Studies using DXA and CT 105
6.1. Contribution of Local Buckling to Femoral Neck Failure 105
6.1.1. Background 105
6.1.2. Materials and Methods 107
6.1.3. Results 122
6.1.4. Discussion 128
6.2. Effect of hormone therapy and physical activity on the femur bone 129
6.2.1. Background 129
6.2.2. Materials and Methods 130
6.2.3. Results 132
6.2.4. Discussion 137
6.3. Relationship Between Reduced Mechanosensitivity and Fracture Incidence .. 140
6.3.1. Background 140
6.3.2. Materials and Methods 142
6.3.3. Results 143
6.3.4. Discussion 146

7 Conclusions and Future Work 149

Bibliography 154

Vita 169

List of Tables

3.1 Geometrical Parameters of original femoral neck image and whole GEM 33
4.1 Mean and standard deviation of coefficient of variation (%) over all projections for each tissue type. 58
5.1 Densities in gm/cm^3 of different materials used in simulations 79
6.1 Subject Data 108
6.2 Computed failure loads (N) required to produce pure material yield, pure local buckling and predicted failure considering both yield and local buckling for one-legged stance and a fall on the greater trochanter. 127
6.3 Participants characteristics for never HT users and current HT users divided into tertiles of physical activity 133
6.4 Ethnicity characteristics for never HT users and current HT users divided into tertiles of physical activity 134
6.5 Subject Categories 143
6.6 Participants characteristics divided according fracture category 144
6.7 Ethnicity characteristics for participants divided according fracture category 144

List of Figures

2.1 Low and high energy X-ray beams are transmitted through a block of bone and soft tissue 13
3.1 Model Generation Workflow 20
3.2 Original shell image versus shell GEM and shell FSM 30
3.3 Geometrical Parameters of original shell image, shell GEM and shell FSM. (a) Percentage error in area (b) Percentage error in I_{max} (C) Percentage error in I_{min}. .. 31
3.4 Original femoral neck image versus whole GEM 32
3.5 Principal Angle of (a) original shell image, shell GEM and shell FSM (b) original femoral neck image and whole GEM. 33
4.1 Determination of the weights w_{ij} of the projection matrix using the nearest neighbors method. 43
4.2 The successive binary algebraic reconstruction technique (SBART) Algorithm. ... 46
4.3 Separation of the cross-section into its basic materials. Original CT image (left) is segmented into 4 grey levels (middle) showing bone (white), fat (dark grey),lean (light grey) and air (black). Individual tissues are shown on right. 51
4.4 Reconstructed images using SBART algorithm from different number of projections in case of known skin boundary for (a) mid-femur, (b) distal femur, and (c) lower leg cross sections. 54
4.5 Reconstructed images using SBART algorithm from different number of projections in case of unknown skin boundary for (a) mid-femur, (b) distal femur, and (c) lower leg cross sections. 54
4.6 Pixel error (in percentage %) in reconstructed images using SBART algorithm from different number of projections with and without knowledge of the skin boundary. 56
4.7 Percentage error in the area of the reconstructed images using SBART algorithm in case of mid-femur (a,b), distal femur (c,d) and lower leg (e,f) with different number of projections with (a,c,e) and without (b,d,f) the skin boundary. 56
4.8 Maximum absolute percentage error in the second moment of area of the reconstructed images using SBART algorithm with different number of projections with and without knowledge of the skin boundary. 57
4.9 Comparison between reconstructions with unknown skin boundary using SBART and DART algorithms with 11 and 13 projections for (a) mid-femur (b) distal femur and (c) lower leg cross sections. 58
4.10 Pixel error (in percentage %) in mid-femur reconstructed images using SBART algorithm from different number of projections (a) with and (b) without knowledge of the skin boundary 60

4.11 Reconstructed images using GC-SBART from different number of projections with unknown skin boundary for (a) mid-femur, (b) distal femur, and (c) lower leg cross sections. 61
4.12 Pixel error (in percentage %) in reconstructed images from different number of projections with unknown skin boundary using SBART and GC-SBART reconstruction algorithms. 62
4.13 Maximum absolute percentage error in the second moment of area of the reconstructed images with different number of projections with unknown skin boundary using SBART and GC-SBART reconstruction algorithms. 62
4.14 3D Model of human cadaveric forearm constructed from series of 2D cross sections. 66
5.1 Two-material decomposition in a DXA projection for a mid-femur cross section. 69
5.2 Two-material decomposition in a representative DXA projection for a lower leg cross section. (a) segmented lower leg cross section. (b) individual projections 70
5.3 0° and 90° projections of a lower leg cross section. 71
5.4 Explanation of the area constraint in case the cross section contains (a) one bone, or (b) two bones. 76
5.5 Simulated X-ray spectra 77
5.6 H_{LE} and H_{HE} of 0° projection of a lower leg cross section 80
5.7 Decomposed aluminum and acrylic 0° projection of a lower leg cross section 80
5.8 Every point from BL table (blue) is matched with the nearest point from AL-AC table (red) with the threshold of 0.05. (only portion of the original data range is displayed). 83
5.9 Matching pairs of Aluminum-Acrylic and Bone-Lean 84
5.10 Results of the linear regression for bone and lean tissue 85
5.11 Results of the linear regression for fat and lean tissue 86
5.12 MPMD curves (red) are shown against the original (blue) and linear interpolation curves (black). Whole curves are shown in (a), a magnified version of the results is shown in (b). 89
5.13 Quality indices calculated from the MPMD (solid lines) and linear interpolation (dashed lines) projections in case of using CT simulations (red), monoenergetic (green) and spectrum (blue) DXA simulations of the mid-femur cross section. (a) Mean area error (fat and lean) over all projections. (b) Mean curve error (fat and lean) over all projections. (c) Mean curve error of soft tissue over all projections. 91
5.14 Quality indices calculated from the MPMD (solid lines) and linear interpolation (dashed lines) projections in case of using CT simulations (red), monoenergetic (green) and spectrum (blue) DXA simulations of the lower leg cross section. (a) Mean area error (fat and lean) over all projections. (b) Mean curve error (fat and lean) over all projections. (c) Mean curve error of soft tissue over all projections. 92

5.15 Reconstructed mid-femur images using SBART algorithm from (a) original, (b) MPMD, and (c) linear interpolation projections in case of using CT simulations. . 94
5.16 Reconstructed mid-femur images using SBART algorithm from (a) original, (b) MPMD, and (c) linear interpolation projections in case of using monoenergetic DXA simulations. 94
5.17 Reconstructed mid-femur images using SBART algorithm from (a) original, (b) MPMD, and (c) linear interpolation projections in case of using spectrum DXA simulations. 95
5.18 Errors in the reconstructed mid-femur images using SBART algorithm from the MPMD (solid lines) and linear interpolation (dashed lines) projections in case of using CT simulations (red), monoenergetic (green) and realistic spectra (blue) DXA simulations. (a) Pixel error. (b) Percentage error in area. (c) Maximum absolute percentage error in the second moment of area. 97
5.19 Reconstructed lower leg images using SBART algorithm from (a) original, (b) MPMD, and (c) linear interpolation projections in case of using CT simulations. . 98
5.20 Reconstructed lower leg images using SBART algorithm from (a) original, (b) MPMD, and (c) linear interpolation projections in case of using monoenergetic DXA simulations. 99
5.21 Reconstructed lower leg images using SBART algorithm from (a) original, (b) MPMD, and (c) linear interpolation projections in case of using realistic spectra DXA simulations. 99
5.22 Errors in the reconstructed lower leg images using SBART algorithm from the MPMD (solid lines) and linear interpolation (dashed lines) projections in case of using CT simulations (red), monoenergetic (green) and spectrum (blue) DXA simulations. (a) Pixel error. (b) Percentage error in area. (c) Maximum absolute percentage error in the second moment of area. 101
6.1 Study workflow 106
6.2 Forces acting on Femur in case of One-legged Stance 108
6.3 Free-Body diagram of the Femur (a) forces in the original directions (b) forces resolved in x-y directions 112
6.4 Femur Internal Forces 113
6.5 Femoral neck Free-Body Diagram 114
6.6 Forces acting on Femur in case of fall 116
6.7 Free-Body Diagram of the Femur 117
6.8 Femur Internal Forces 118
6.9 Femoral Neck Free-Body Diagram 118
6.10 FSM models shown in 1st column, and stress distributions for the two simulated loading conditions in 2nd and 3rd columns where compressive and tensile stresses are shown with red and blue lines, respectively. 123

6.11 Maximum stresses on inferior (medial) and superior (lateral) margins of the femoral neck cross-section in the plane of bending, under a) a one legged stance and b) a fall with impact on the greater trochanter. 124
6.12 FSM models shown in 1st column and buckled shapes for the two simulated loading conditions in 2nd and 3rd columns where buckled shapes (red elements) are superimposed over undistorted shapes..... 126
6.13 Slenderness ratio in a) a one legged stance and b) a fall with impact on the greater trochanter 127
6.14 Maximum medial neck stress by tertile of physical activity. All differences between tertiles and between never and current users $p<0.001$. 135
6.15 Maximum medial neck stress by tertile of physical activity after adjustment for lean mass fraction. Differences between tertiles are non-significant in Never-users but are significant in current users ($p<0.013$ middle and $p<0.001$ highest versus lowest tertile). 136
6.16 Maximum stresses on the infero-medial cortex of the femoral neck at its narrowest point in a one-legged stance, adjusted for HRT use, lean mass fraction and physical activity score. 145

Abbreviations

ART	Algebraic reconstruction techniques
BMD	Bone mineral density
BMI	Body mass index
CSA	Cross-sectional area
CT	Computed tomography
DART	Discrete algebraic reconstruction technique
DPA	Dual-photon absorptiometry
DQE	Detector quantum efficiency
DXA	Dual energy x-ray absorptiometry
FEA	Finite element analysis
FEM	Finite element method
FSM	Finite strip model
GC-SBART	Geometrically constrained successive binary algebraic reconstruction technique
GEM	Geometrically-Equivalent Model
HAS	Hip structural analysis
HT	Hormone therapy
LI	Linear interpolation
MET	Metabolic equivalent task
MPMD	Multi-projections material decomposition
NURB	Non-uniform rational B-spline
pDXA	peripheral DXA

pQCT	peripheral QCT
QCT	Quantitative computed tomography
RA	Radiographic absorptiometry
RMSE	Root mean square error
SART	Simultaneous algebraic reconstruction technique
SQP	Sequential quadratic programming
SBART	Successive binary algebraic reconstruction technique
SPA	Single-photon absorptiometry

Chapter 1

Introduction

1.1. Osteoporosis

Bone is the living tissue that makes up the skeleton of our bodies. It provides shape and support for the body as well as protection for some organs. It also serves as a storage site for minerals and provides the marrow for the development and storage of red blood cells. There are two types of bone tissue, compact tissue (cortical bone) and spongy tissue (trabecular bone). Cortical bone is the hard tissue that forms the outer layer of bones, while the trabecular bone is a sponge-like tissue found inside them. Because of its complex function, many diseases and disorders may affect the bone [1].

Osteoporosis is the most common bone disease. It is characterized by reduced mechanical strength which leads to an increase in bone fragility and susceptibility to fracture [2]. Diagnosis is most commonly done by observing reduced bone density at certain skeletal sites. Fractures tend to occur most commonly at the wrist, spine and hip [2] although other sites may also fracture. Osteoporosis affects an estimated 75 million people in Europe, USA and Japan and is responsible for 1.5 million fractures in the United States [3]. One in three women and one in five men over age 50 will have an osteoporosis-related fracture in their lifetime [4-6]. In the United States today, 10 million individuals already have osteoporosis and 18 million more have low bone mass, placing them at increased risk for this disease [7].

1.2. The role of engineering analysis in osteoporosis

Osteoporosis is most commonly diagnosed by measuring bone density using conventional bone density modalities such as dual-energy X-ray absorptiometry (DXA) and quantitative computed tomography (QCT). Despite the fact that it is convenient and relatively simple, density methods identify less than half of those who are at risk of osteoporotic fracture [8, 9]. The underlying reasons have been extensively studied and are complex, but fundamentally the problem is that the mechanical behavior of a complex human bone cannot be reliably reduced to a simple concept such as density. Density does not represent any mechanical property, or any specific configuration of mechanical properties that could be used in an engineering analysis. Ideally a diagnostic method needs to be developed that shares the clinical simplicity of a density test but that provides the rigor of an engineering analysis. This mechanical analysis could be based on CT data, but CT scanners are expensive, radiation doses are too high for routine screening, and the mapping of the CT data to the engineering model has yet to be reliably automated.

The objective of this research is to solve some of the critical technical problems toward implementing a practical bone engineering analysis in the clinical setting. The specific aims of this research are:

(1) To show the significance of engineering analysis in clinical research by performing different clinical studies using pre-acquired DXA and CT data.

(2) To develop accurate geometrically-equivalent models of tomographic cross sections for use in engineering analysis.

(3) To provide a new method of generating high quality images from as few projections as possible to limit the radiation dose to the patient.

Ultimately, an imaging scanner system will be commercially developed, based on principles elucidated in this dissertation. The contributions of this dissertation are outlined in the next section.

1.3. Dissertation Contributions

1.3.1. Image reconstruction from limited number of DXA projections

The first contribution of this dissertation is a novel method for reconstructing a high quality images from a small number of projections over a rotational angle of 90 degrees using data decomposed using DXA principles into the principle tissues, bone mineral, lean mass and fat mass. The methods are designed for ultimate implementation in a multi-projection DXA scanner system for use in scanning human limbs. The scanner will use the data to generate a 3D model of the limb for use in mechanical and structural analyses. To further improve the quality and geometrical and mechanical properties of the reconstructed cross sections, we added geometrical constraints to the reconstruction algorithm.

1.3.2. Material decomposition of bone cross sections from limited number of DXA projections

To supply the reconstruction algorithm with the individual tissue projections from the DXA scanner, material decomposition is employed. Since dual energies permit discrimination into only two materials while human limbs contain three, regions of fat and lean projections under the shadow of bone will be missing. These missing portions of the projections must be estimated so that complete projections are available for reconstruction. We propose a method for three-material decomposition from limited

number of DXA projections. In this method, we use the available projections along with logical constraints to form an optimization objective function. By minimizing this objective function, we estimate the best curves to fill in gaps in the projections while preserving the soft tissue composition and the area under the curves over all projections. This in turn preserves the tissue components in the cross sections which makes the structural and mechanical studies more accurate.

1.3.3. Geometrically-equivalent models of bone cross sections

To use the existing CT cross sections of femoral neck bones in a mechanical or structural studies, reasonably accurate structural models need to be generated. Because current CT data cannot resolve the fine structural details typical of osteoporotic bones, some accommodation must be incorporated into the engineering analysis. Instead of the more common density modulus approximation [10], we have incorporated an alternative approach that preserves the shell geometry in geometrically-equivalent bone models. These models which should be more accurate than those based on density modulus methods, preserve the cross sectional area, second moment of area and principal angle of the original cross-section, yet generate a more accurate cortical shell that should bears most of the applied loads encountered in use or in traumas. We then apply the finite strip method to the bone cortex in mechanical analysis that includes the investigation of local buckling failure.

1.3.4. Clinical studies using different modalities

Some analyses of previously acquired DXA and CT femoral neck bone data were performed to illustrate the importance of engineering and mechanical analyses in clinical

research. The first study employs a 2D beam analysis on DXA data to evaluate the effects of hormone therapy and physical activity on the femurs of postmenopausal women. The second study on the same data assessed the relationship between reduced mechanosensitivity and fracture incidence. Finally, a study based on 3D analysis of CT data on human cadaver femurs used geometrically-equivalent bone models to test whether the local buckling contributes to bone fractures under simulated physiologic and traumatic load conditions.

1.4. Dissertation Organization

The rest of this dissertation is organized as follows. Chapter 2 provides background on bone anatomy, physiology and on the disease of osteoporosis. Chapter 3 describes how to transform CT cross sections into geometrically-equivalent models using the proposed technique. In chapter 4, we present the new image reconstruction algorithm from a limited number of projections decomposed into individual tissue components. Chapter 5 describes the preparation of the required projections from DXA data for reconstruction as well as a method for estimating missing portions of these projections using the novel material decomposition algorithm. The clinical studies are presented next in chapter 6, with the first section devoted to hormone therapy and exercise, next is a study of mechanosensitivity and fracture, and the third considers contribution of local buckling to fractures of the femoral neck. Finally, Chapter 7 concludes the dissertation and provides an overview of how the research might ultimately be continued in a clinical instrument.

Intended to be blank.

Chapter 2

Background

2.1. Bone anatomy

Bone is a complex organ despite its simple appearance. It consists of several different tissues such as osseous tissue, cartilage, connective tissue, adipose tissues, and nervous tissue [1]. All these tissues are working together so bone can perform its intended functions. Bone is classified according to its shape into five categories: long bones, such as femur bone, short bone, such as wrist bone, flat and irregular bones as in sternum and vertebra respectively, and finally sesamoid bones which form where much physical stress and tension is expected such as in palms and patellae [1].

Osseous tissue consists of four types of cells that help bone grow and remodel. First are the osteogenic cells, which can divide to produce new cells that in turn develop into osteoblasts. Osteoblasts are the bone-building cells; they form the bone matrix. Osteocyte cells are mature bone cells that maintain bone tissue and its daily metabolism. The last type is the osteoclasts; they are huge cells that function in resorption and the breakdown of the bone matrix [1].

Osseous tissue has two major types: the compact bone tissue and the spongy bone tissue. Compact bone tissue (cortical bone) which forms the external layer of all bones is dense and strong. It provides the support, protection, and resistance to stresses developed by weight and physical activities. Spongy bone tissue on the other hand consists of

honeycomb-like network of bone called trabeculae [1, 11]. The spaces in trabeculae make the bone lighter and provide a volumes for storage of red bone marrow responsible for producing blood cells.

2.2. Bone remodeling and modeling

Bone remodeling is the continuous process of bone resorption and formation in which old osseous tissue is replaced by new tissue in order to maintain healthy bones. Osteoclasts are the bone-destroying cells while osteoblasts are the bone-producing cells. Osteoclasts destruct the old bone matrix and osteoblasts deposit minerals forming new bone matrix. Remodeling rates for compact tissue is ~4% per year while it reaches 20% for trabecular bone. Remodeling occurs at different rates in different skeletal sites [1]. The remodeling cycle can start after bone injury, to replace damaged bone. Remodeling is critical for bone health, since new osseous tissue is less brittle and much stronger than the old one.

Bone modeling differs from remodeling as it adjusts the mechanical strength of bone tissue to adapt to current loading conditions [1, 11]. The process is sensed by strain levels detected by osteocytes in tiny spaces within bone tissue. Modeling can increase bone strength by adding material to locations where strains exceed some threshold level. Modeling can also degrade bone as in disuse by removing bone tissue from regions where strains fall below some lower threshold. Modeling continually enables bones to adapted to physiological loads it encounters. As a result of the modeling process, bone may widen or change its axis depending on the load it encounters. For example, bones normally widen with aging in response to bone formation on periosteum and bone resorption on inner surfaces near the neutral axis [11]. Paradoxically this process reduces the

volumetric density of bone while not necessarily reducing mechanical strength since bending rigidity may be maintained in a larger diameter bone with less material than contained in a smaller diameter.

2.3. Bone diseases

The healthy bone requires a balance between bone formation and resorption. This balance can be altered by mechanical, genetic, hormonal, or nutritional factors [11]. Too much bone formation causes the bone to be thick and heavy, while too much resorption causes the bone to be weak and susceptible to fractures as in osteoporosis [1]. Other diseases such as Paget‘s Disease are characterized by excessively high bone turnover, where both operations of bone formation and resorption are abnormally activated. Although bone density may increase in this disease, bone strength is decreased and fractures can occur due to the irregular architecture of the bone matrix [11].

Since osteoporosis is very common bone disorder, much research has done to study its characteristics and causes. A large fraction of the research has concentrated on bone density measurements and the factors that influence bone density with less emphasis on the structural factors underlying the loss of strength in osteoporosis. This state of affairs can largely be ascribed to the widespread availability of density testing and the lack of good methods for evaluating bone structure.

2.4. Measuring bone density

Bone mineral density (BMD) testing started in the early 1940s where plain X-rays were used for measurement. However, the effect only by this method becomes apparent only

after 40% of the bone density is lost. Qualitative techniques such as the Singh index were used to identify trabecular pattern in bone images. X-rays were graded from IV down to I according to the disappearance of normal trabecular patterns. More advanced methods and technologies have been developed over the years to quantify bone density with methods such as radiographic absorptiometry, photon absorptiometry techniques and quantitative ultrasound bone densitometry [12]. In radiographic absorptiometry (RA), bone mineral density (BMD) can be measured from a high resolution X-ray images. An X-ray of the hand is taken with the presence of an aluminum wedge as a reference. The X-ray image is then digitized and analyzed to get the BMD by calibrating the bone density in the image with the reference wedge density. The bone density at other skeletal sites can then be predicted from this hand radiograph.

Techniques that depend on the photon attenuation physics started in 1963 with single-photon absorptiometry (SPA). In SPA, a monochromatic or single-energy photon beam is passing through bone and soft tissue. The amount of mineral can be quantifies by subtracting the beam intensity after passing through soft tissue alone from the original incident beam intensity; usually wrists were used as a site of measurement because they could be adequately penetrated with the low energy gamma ray sources in use at the time [12]. Dual-photon absorptiometry (DPA) on the other hand used ^{153}Gd a radioactive isotope that emits a photon beam with two distinct energy peaks. This gives the ability to distinguish soft tissue, and in turn allows for bone density measurements in the areas surrounded by larger soft tissue masses such as spine and proximal femur [12, 13]. Even so, this machine precision degrades with time due to the decay of the isotope.

Dual-energy X-ray absorptiometry (DXA) is similar to DPA but replaces the radioactive isotope with an X-ray tube. DXA measurements are superior over those of DPA because measurement precision does not decay and higher spatial resolution is possible with an x-ray source. Currently DXA is considered the gold standard for BMD testing. Quantitative Computed Tomography (QCT) on the other hand, is a photon absorptiometry technique that can be performed with most standard CT scanners by adding software and calibration methods. It is unique because it provides 3-dimensional volumetric measurements of bone from which volumetric density can be computed. It also has the ability of separating the area of interest from overlying tissue. The radiation dose for QCT however is relatively high compared to DXA and it is also relatively expensive. More details about DXA and QCT will follow in the next subsections.

Finally, smaller dedicated bone testing devices such as peripheral DXA (pDXA) and peripheral QCT (pQCT) have become widely available. These can be used for measuring BMD in peripheral sites such as the forearm. Because they are smaller and less expensive, they are convenient in bringing the test to populations who otherwise would not be tested. But accuracy in predicting the debilitating fractures of the hip and spine is worse than that of scanners that measure at the hip or spine. For this reason, peripheral machines are not considered adequate for monitoring patients undergoing osteoporosis treatment.

2.4.1. Dual Energy X-ray Absorptiometry (DXA)

DXA is widely used to measure bone mineral density and tissue composition. The underlying concept is that the attenuation of x-ray beams with two different energies can decompose an absorber into two materials that differ in the effective atomic number.

Bone mineral, the inorganic component of bone tissue, can be discriminated from soft tissue, and in ray paths that do not include bone, soft tissues can be decomposed into adipose and lean tissues. A good overview of the basic concept is provided in the fundamental paper by Lehmann *et al.* [14]. A brief description of the concept is outlined here.

Assuming the simple case of monochromatic X-ray beams with different energies (low and high energy) transmitted through a block of two materials (bone and soft tissue) as shown in Fig. 2.1, the attenuation equations of each beam results in the following equations [15]:

$$I_L = I_0^L e^{-\left[\left(\frac{\mu}{\rho}\right)_b^L \sigma_{b+} \left(\frac{\mu}{\rho}\right)_s^L \sigma_s\right]} \tag{2.1}$$

$$I_H = I_0^H e^{-\left[\left(\frac{\mu}{\rho}\right)_b^H \sigma_{b+} \left(\frac{\mu}{\rho}\right)_s^H \sigma_s\right]} \tag{2.2}$$

where H and L denote the high and low energy beams respectively, σ_b and σ_s are the areal density of bone and soft tissue in gm/cm^2, While $\left(\frac{\mu}{\rho}\right)$ represents the mass attenuation coefficient in cm^2/gm.

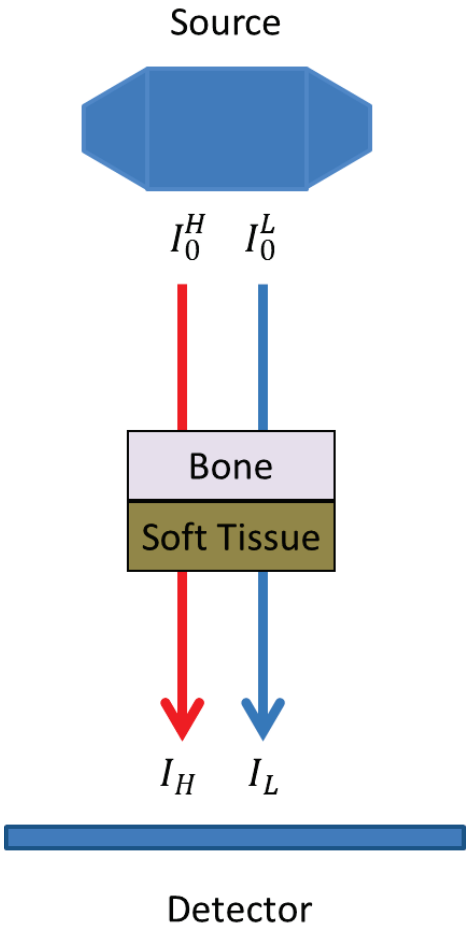

Fig. 2.1. Low and high energy X-ray beams are transmitted through a block of bone and soft tissue

Define the log of intensity transmission for low and high energy beams as m_L and m_H respectively, where

$$m_L = \ln\left(I/I_0\right)_L \tag{2.3}$$

and

$$m_H = \ln\left(I/I_0\right)_H \tag{2.4}$$

Solving equations (2.1) and (2.2) simultaneously for the bone areal density and defining:

$$\sigma_b = \frac{R_s m_H - m_L}{\left(\frac{\mu}{\rho}\right)_b^L - R_s\left(\frac{\mu}{\rho}\right)_b^H} \tag{2.5}$$

where

$$R_s = \frac{\left(\frac{\mu}{\rho}\right)_s^L}{\left(\frac{\mu}{\rho}\right)_s^H} \tag{2.6}$$

If the region contains only soft tissue ($\sigma_b = 0$), from equation (2.5) R_s can be calculated as:

$$R_s = \frac{-\ln\left(I_s/I_0\right)_L}{-\ln\left(I_s/I_0\right)_H} \tag{2.7}$$

where $I \rightarrow I_s$ because intensity is attenuated exclusively by soft tissue and R_s measures the percentage of fat in the soft tissue.

A major advantage of DXA is that, with efficient detectors, the radiation dose can be quite small so that sequential studies can be easily justified for disease screening even in vulnerable populations such as children. Expressed as a skin dose, radiation during a

proximal femur study, for example, is only 2-5 mrem [12]. Scan time is also extremely short with DXA, it takes less than five minutes to measure total body composition.

However, DXA also has its limitations. For example, since current DXA scanners work primarily with a single 2D projection image to measure bone density, the original volume cannot be estimated. In this case, we cannot differentiate between thick low-density bone and thin high-density bone [15]. To solve this problem, there is a growing body of literature extending DXA ideas into 3D x-ray computed tomography [16-19].

Also, because of the lack of standardization across DXA manufacturers, BMD cannot be directly compared. For example, the average difference in BMD between the two largest manufacturers (Hologic and GE Lunar) systems is approximately 8% [15].

2.4.2. Quantitative Computed Tomography (QCT)

QCT uses a standard CT machine to measure BMD. In QCT, the patient lies on a phantom containing reference densities, which appears in image cross-sections and is used for calibration. The calibration process transforms the Hounsfield Units (HU) of the CT image into the relative BMD values. The reference phantom also helps to compensate for variability in CT machines. QCT is the only currently available method that gives a true volumetric distribution of bone density [20] although there is little evidence that volumetric density discriminates osteoporotic patients better than areal (DXA) BMD.

QCT provides substantially more information than DXA. For example, it can separate cortical and trabecular bone. It is also very efficient in spine and hip clinical studies. Spine scans performed using QCT has been used in several osteoporosis studies

[21-23]. It has been found effective in separating osteoporotic patients from normal individuals. Nonetheless, the radiation exposure of QCT is much higher than DXA and the cost of the scan is also higher. This is one of many reasons why QCT is less widely used compared to DXA.

Chapter 3

Geometrically-Equivalent Models of Bone Cross Sections

Cross-sections through the femoral neck are often used in studies of hip fractures since this is a common site of fragility fracture. However, additional steps must be taken in the model to accommodate the relatively low resolution and partial volume fraction effect especially in the thin cortices and sparse trabeculae of osteoporotic subjects. As previously noted we have employed an alternative approach that should be more accurate than the more commonly used density-modulus approximation. Accordingly we have developed a reliable method for deriving a smooth, geometrically accurate model of the femoral neck cross-section using CT scan data (or the data from the proposed scanner).

3.1. Background

Bone fracture occurs when loads generate internal stresses that exceed the material strength of bone tissue. Studies of the factors governing fragility often employ models of the bone structure and simulations of failure conditions [24]. Bone tissue is highly complex and practical imaging method cannot resolve all the internal complexity, hence approaches for simplifying the structural model while retaining accurate behavior under load are an important part of the process. Most models are based on some form of the Finite element method (FEM) using dimensional information from 3D imaging methods (usually CT) to generate the model [25-28].

FEM is intrinsically a simplification method whereby the geometry of an object is represented by a 3-dimensional mesh of internally-uniform elements connected by nodes.

Mechanical behavior can be predicted by applying loading forces to the model in realistic directions and magnitude with the stresses propagating through the model from one element to the next. The accuracy of the model depends on the numbers and sizes of the elements used to construct the model. Increasing the numbers of elements while reducing their size results in more accurate behavior but this considerably increases the computational load needed to estimate failure. Typically model generation involves mapping of the 3D resolution element of the CT image (voxel) to model elements. The technical problem is that in clinical CT scans, voxel dimensions exceed the dimensions of the bone feature it represents. In other words the voxel is _thicker' than thin cortices or trabeculae in at least some part of the model. This problem is especially acute in osteoporotic bones. The most common approach is to use the fact that the load resistance of an element only partially filled with bone tissue varies roughly as the bone volume fraction. The mapping technique can take advantage of the ability of the CT scanner when calibrated, to measure the volume fraction of the voxel. The volume fraction is accommodated by modulating the elastic modulus of the element with the volume fraction based on experimental observations [10, 29-34]. Thus the model accommodates the inability to resolve substructure by modulating the element modulus [35].

Density-modulus curves are quite problematic, they vary significantly according to the anatomical site used in the experiment, data disperses widely and does not easily fit a functional relationship and no universal density-modulus relationship can be used [10, 36, 37]. A discussion of the density-modulus relationship method is beyond the scope of this thesis, but suffice it to say that it works poorly when cortices are thin. This is an important limitation because most loading conditions likely to cause failure concentrate

the load in the cortex. For these reasons we sought to completely avoid the density modulus relationship in this study.

A specialized version of Finite Element Analysis (FEA) called Finite Strip Method (FSM) was designed to evaluate failure in pure elastic buckling in thin-walled structures. The finite strip method was invented for structural analysis in the late 1960s. In this method a thin-walled member is discretized into longitudinal strips. This is advantage over other methods such as finite element method, which applies the discretization in both the longitudinal and transverse direction [38, 39]. This feature enables the modeling of a structure that may have complex geometry in its cross section, but vary relatively slowly along the length. This method has been proposed to handle failure of the femoral neck under conditions involving a fall to the side impacting on the hip.

Our objectives are to produce a Geometrically-Equivalent Model (GEM) for femoral neck bone cross-section from a CT scans and to create a finite strip model of the shell using the generated shell models. These models can then be used in further fracture studies such as buckling analysis in Chapter 6.

Fig. 3.1 shows the workflow of the method used to generate the GEM from CT image data. Beginning with the original CT image of the femoral neck bone at its narrowest point, a boundary detection method is used to separate the shell from the image of the core. The resulting shell and core images can then be used to generate individual geometrically-equivalent models for the core and shell and for the cross-section by combining both models. The shell model is used to generate finite strip model of the shell. This shell FSM can be used later in buckling analysis of the femoral neck bone.

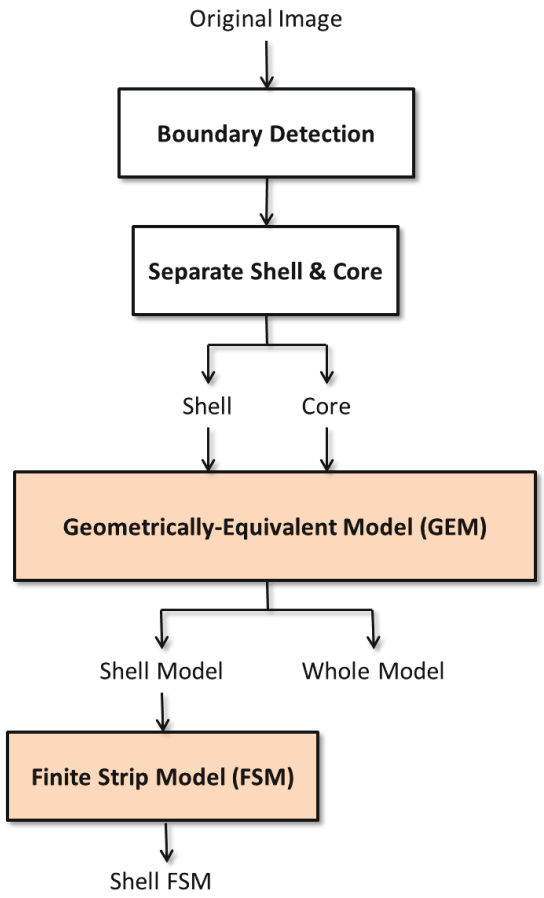

Fig. 3.1. Model Generation Workflow

3.2. Materials and Methods

3.2.1. Subjects

Six cadaver femurs from German subjects including 3 males aged 52, 66 and 93, and 3 females aged 65, 81 and 85 were scanned in a water bath using a 16-slice Siemens CT scanner with a slice spacing of 0.5 mm. Specialized software was used to extract the cross-section at the minimum neck diameter and FSM models of the cortex were derived and evaluated in the plane of the neck-shaft angle. Scan data was kindly supplied by J.K. Brown, Mindways Software Inc., Austin, TX.

3.2.2. Preprocessing

First, we need to resize the image to decrease the pixel size to makes the resulting model more accurate in terms of geometric measurements. Then, the CT image in Hounsfield units is converted into a binary image where the soft tissue has the value of zero and bone has value of one. This is done by assigning average values for both bone and soft tissue, truncating and scaling the image. The resulting image will express the mineralization of bone tissue.

3.2.3. Boundary Detection

Bone cross-sections contain two types of bone tissue that must be separated: cortical bone (shell) and trabecular bone (core). This requires detection of two boundaries, the outer boundary which contains the whole cross-section and the inner boundary which encircles the core only.

To detect the outer boundary, we eliminate all of the details in the image by assigning the value of one to all pixels that contains bone or soft tissue, leaving the other pixels as zero. This approach is based on the Canny method [40] to detect the edges in that image.

Detection of the inner boundary is more difficult, especially in low resolution images where partial volume fraction obscure trabeculae and thin cortices. To overcome this problem, we estimate the thickness of the cortex – at its thickest part – and use this value as a first estimate to the location of the inner boundary. So, we first need to determine the location of the thickest part of the cortex then measure its thickness in pixels.

A good estimate of the location of the thickest part of the cortex can be found using the area moment of inertia (or second moment of inertia) and the principal angle of the bone cross-section.

Generally, the second moment of area I is used to determine the resistance of the cross-section to bending about the axis in the plane of the cross-section and is calculated as [41, 42]:

$$I_x = \int \mathrm{y}^2 \, \mathrm{dA} \tag{3.1}$$

$$I_y = \int \mathrm{x}^2 \, \mathrm{dA} \tag{3.2}$$

$$I_{xy} = \int \mathrm{xy} \, \mathrm{dA} \tag{3.3}$$

and

$$I_\theta = \frac{I_x + I_y}{2} + \frac{I_x - I_y}{2} \cos 2\theta - I_{xy} \sin 2\theta \tag{3.4}$$

where I_x and I_y are the second moments of area with respect to the x and y axis respectively, I_{xy} is the product of inertia, required in the study of bending of nonsymmetrical beams, and I_θ is the same as I_x for an inclined axis at an angle θ measured counterclockwise from original x-axis to inclined x'-axis.

The angle at which I_θ has extreme value (could be maximum or minimum) is called the principal angle, α, and it is calculated using the following equation:

$$\tan 2\alpha = \frac{2I_{xy}}{I_x - I_y} \tag{3.5}$$

There is two roots for 2α, which are 90° apart, which means that there are two orthogonal axes have the extreme values for the second moment of area, one is the maximum and the other is the minimum. I_{max} and I_{min} can be calculated as:

$$I_{max,min} = \frac{I_x + I_y}{2} \pm \sqrt{\left(\frac{I_x - I_y}{2}\right)^2 + I_{xy}^2} \tag{3.6}$$

Intuitively, the maximum value for second moment of area , I_{max}, must be located at the strongest axis of the bone cross-section, which can be determined using the principal angle. So, to calculate the cortex thickness at its thickness part:

1. Calculate I_x, I_y, I_{xy} and the principal angle.
2. Rotate the image by its principal angle.
3. Take the first derivative of the profile line along *X* and *Y* axis.
4. Count the number of pixels between first and second zero crossing, this is the estimate of the cortical thickness.

At this point we have the outer and inner boundaries of the cross-section under study, however these curves are not smooth. For the final model to look as real as possible, smooth boundaries are required. NURBs (Non-uniform rational B-spline) can be used to perform this task. NURB is a mathematical model commonly used in computer graphics for generating and representing curves and surfaces [43]. NURBs are fitted to the pre-determined inner and outer boundaries. Both NURB curves are adjusted to have the same number of points with each adjacent pair of points are separated by 5 degrees as measured from the center of area of the original image.

3.2.4. Separate Shell and Core

From the last step, we have two NURB curves for the inner and outer boundaries and the original cross-section image. In order to separate shell and core, the INPOLYGON function in MATLAB R2006b is used to determine the points inside the inner boundary

which are assigned to the core, while points between inner and outer boundaries are assigned to the shell.

3.2.5. Shell GEM

The original shell image has different gray scale values, because of the partial volume fraction effect, and this does not reflect the reality. The real cortical bone must have approximately the same value, assumed to be 1 if it is fully mineralized. This property has to be adopted in a good geometrically-equivalent shell model. The algorithm used to generate an accurate realistic shell GEM is described in the following steps:

1. Generate a mask to go over the original shell image and create the shell model. This mask is created using the inner and outer boundary NURB curves. Beginning with the first point on each curve, construct a mask with length of 10 pixels and width equal to the maximum thickness of the shell.
2. Calculate the center of mass $(\bar{x}, \bar{y})$ of the original shell area included inside the mask where [41, 42]:

$$Q_x = A\bar{y} = \int_{Area} y \, dA \tag{3.7}$$

and

$$Q_y = A\bar{x} = \int_{Area} x \, dA \tag{3.8}$$

where x and y are the coordinates of an element of area dA, A is the total area inside the mask region, and Q_x and Q_y are the first moments of area with respect

to the *x* and *y* axes, respectively. The first moment of area is a measure of the distribution of the area in relationship to an axis.

3. Calculate the cross-sectional area (CSA) of the original shell area included inside the mask where:

$$CSA_1 = p \sum_{i=1}^{N_T} g_i \tag{3.9}$$

Where p is the area of one pixel, N_T is total number of pixels, and g_i is the gray scale (from 0 to 1) at pixel *i*.

The cross-sectional area of the shell model with the same length is:

$$CSA_2 = p.l.t \tag{3.10}$$

Where *l* is the mask length (10 pixels) and *t* is the effective thickness of the shell (needs to be determined).

4. Let $CSA_1 = CSA_2$ and calculate *t*. Then:

$$t = \frac{\sum_{i=1}^{N_T} g_i}{l} \tag{3.11}$$

5. Using the location of the center of mass and thickness, calculate two new points on the outer and inner shell edges. These new points will construct the new boundaries of the shell.
6. Move the mask up to the next points, and repeat the steps 2-4 until all the new points in the two boundaries are determined.
7. Fit NURB curves to the new points in the inner and outer sides to generate the new –modeled– inner and outer boundaries.
8. Fill the pixels in between these two curves with ones. This completes the shell modeling algorithm.

3.2.6. Finite Strip Model (FSM)

As in the finite element model, finite strip model (FSM) consists of small elements connected by nodes and each element has its material properties. To construct FSM from the shell model, we need to determine the elements, the nodes that connect them with their position and degree of freedom, and the material properties of the elements (which reflects the material properties of bone in this case). In our calculations, we used the following parameters:

1. The material properties for bone are [44, 45]:

   $E_x = E_y = 17{,}000\ Mpa$ $\quad V_x = V_y = 0.30$ $\quad G_{xy} = 11{,}346\ Mpa$

   Where E is the modulus of elasticity (or Young's modulus), V is Poisson's ratio and G is the shear modulus of elasticity

2. Nodes are chosen to be halfway between inner and outer boundary curves; the number of nodes is equal to the number of points in these curves.
3. Each element is comprised of two nodes, the number of elements is equal to one less the number of nodes, and the thickness of an element is the number of shell pixels lying on the perpendicular vector to the vector linking the two nodes.

3.2.7. Whole GEM

To create a geometrically-equivalent model for the whole bone cross section, after modeling the shell, the core must be modeled. The problem in the core is that it is non-uniform. It is dense in some areas and less dense in others. The model needs to be as uniform as possible for the FSM process.

To generate the core model, we model the core image column by column to get the column model and then model it row by row to get the row model, averaging these two models will yield the average final core model. The algorithm is described into details in the following steps:

1. Begin with a column in the core image; sum all the pixel values in this column.
2. Get the corresponding column in the shell model image, and calculate the number of zero value pixels in this column inside the inner boundary. This will be the length of new column model in the core model image.
3. Divide the sum value calculated in step 1 by the number of pixels from step 2; this gives the average value of the core column to be added in the column model such that this model will preserve the same CSA.
4. Repeat these steps for each column in the original core image. Finally we will have a column model.
5. Repeat the first four steps on each row to get a row model.
6. Average the row and column model to have final core model.
7. Put the core and shell models on the same image, we will have the whole GEM for the original bone cross-section.

It is useful to mention that modeling the core distribution in many other directions such as 30^0, 45^0 and averaging all of these models did not significantly improve the geometrical results. Due to excessive computation time it was decided to use only 2 directions.

3.2.8. Quality Indices

Several geometrical measurements are calculated from the GEM and FSM models and compared with those of the original images to judge the quality of the models. We consider geometrical parameters because we intended to use these models in the engineering analysis, in which those parameters play an important role. These geometrical measurements include the cross-sectional area (CSA), moments of inertia in X and Y direction (I_x and I_y), principal angle and principal moments of inertia (I_{max} and I_{min}).

The cross-sectional area has been calculated previously in equation (3.9). Area of the original images $A_{Original}$ will be compared to the area of the model A_{Model} to compute the percentage area error as:

$$\varepsilon_A = \frac{A_{Model} - A_{Original}}{A_{Original}} \times 100 \tag{3.12}$$

The percentage error in I_{max} and I_{min} is also calculated in a similar way.

3.3. Results

Fig. 3.2 shows the original shell images in the first column, generated shell model in the second column and the equivalent FSM in the third column for each of the six subjects tested. It is obvious that the shell GEM images preserve the original shell shape while correcting for the partial volume fraction effects by effectively making the cortex uniformly mineralized.

Fig. 3.3 shows the geometrical parameters of the original shell image and the two models. Percentage errors in area, maximum and minimum second moment of area between the original shell image and the shell GEM and shell FSM for the six cases are shown in (a), (b) and (c) respectively. In all cases the percentage error ranges from 0% to 3.12%. Principal angles are shown in Fig. 3.5(a) where the maximum difference in angles takes place in case 3 and equals to 1.5° which is a small difference. These values means that shell models are pretty accurate and preserving the geometrical features of the original shell images.

Fig. 3.4 shows the original femoral neck images versus the generated GEM for the six subjects. The models have a uniform core that follows the original core; it is brighter where the original core is more dense. Table 3.1 shows the corresponding geometrical measurements. The percentage area error is still very low (maximum is 0.7% in case 1). The whole GEM in cases 4 and 6 have percentage area error of zero, which means that the cross sectional area is completely preserved. The percentage error in I_{max} has a maximum of 5% in case 2 and minimum of 1.28% in case 4. I_{min} has a maximum error of 6.22% in case 3.

As shown in Fig. 3.5 (b), cases 2 and 5 have a good principal angle match between the original and GEM images with difference less than 1°. However, differences are higher in the rest of cases with maximum of 6.8° in case 4. Overall the errors are still low and in the acceptable range with maximum of 6.22%.

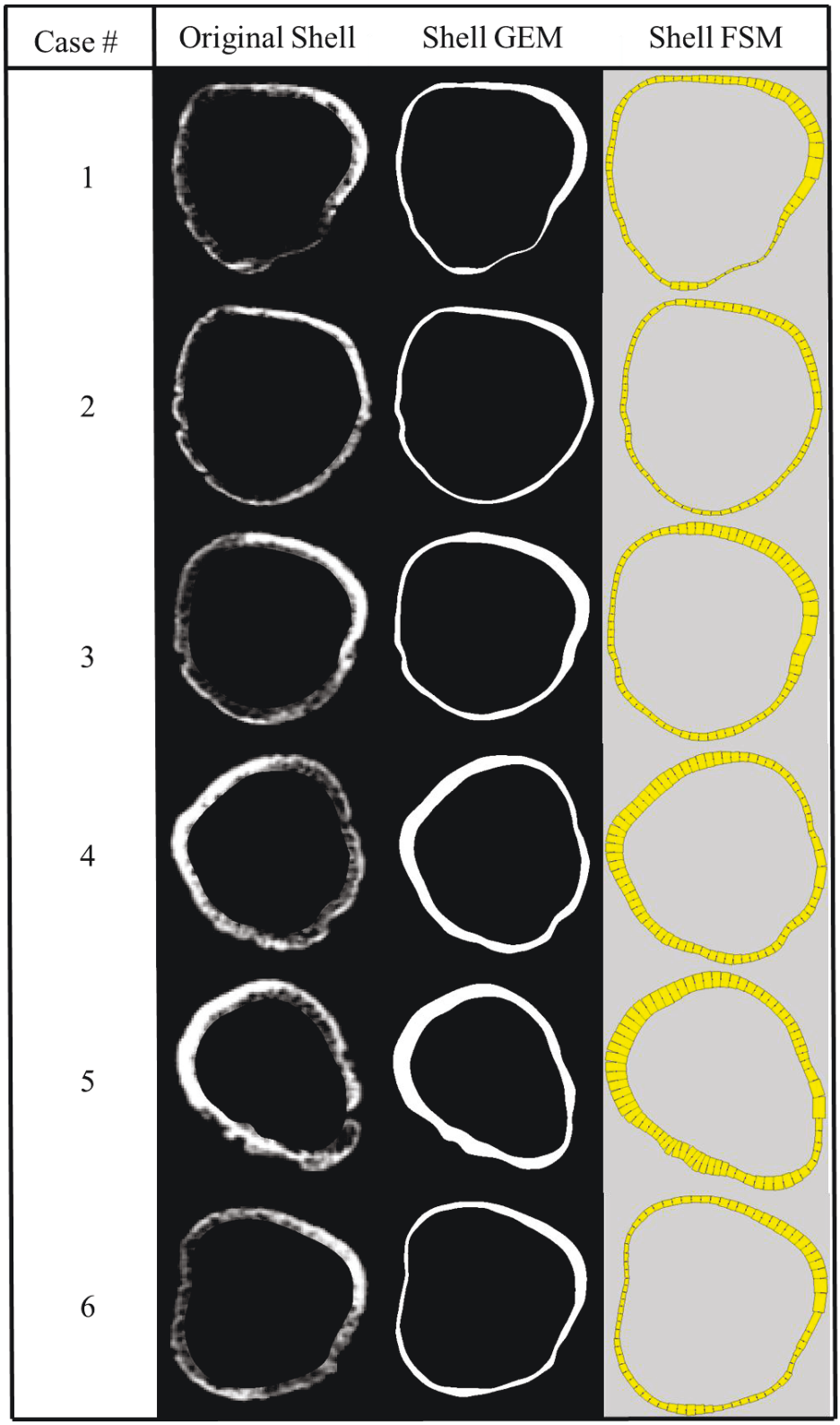

Fig. 3.2. Original shell image versus shell GEM and shell FSM

(a)

(b)

(c)

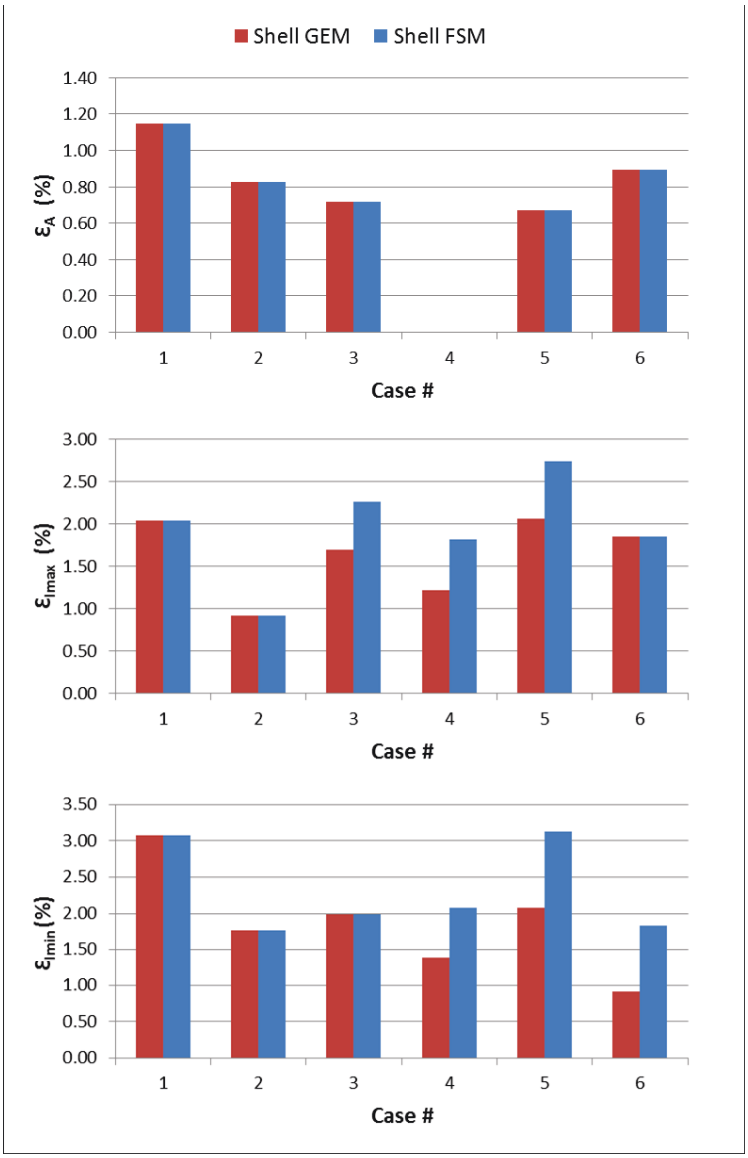

Fig. 3.3. Geometrical Parameters of original shell image, shell GEM and shell FSM. (a) Percentage error in area (b) Percentage error in I_{max} (C) Percentage error in I_{min}.

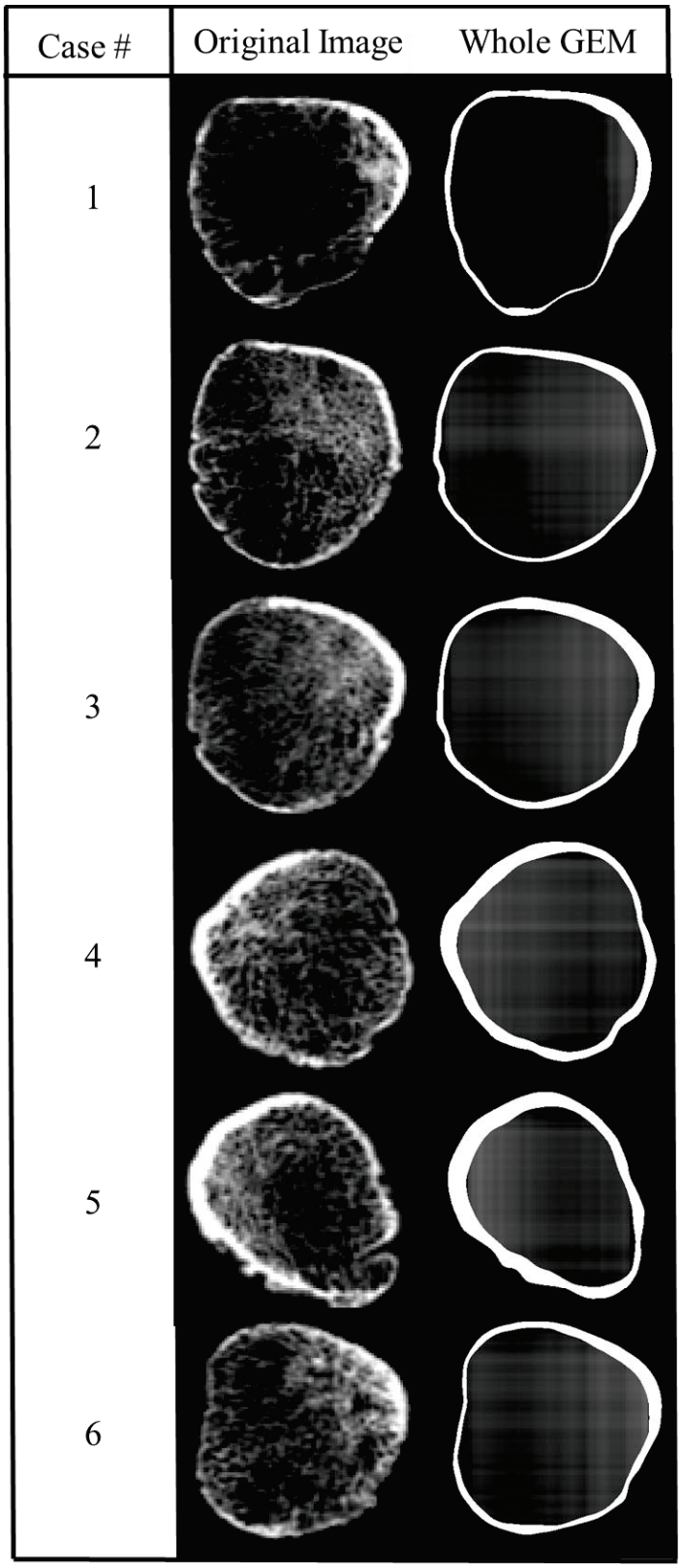

Fig. 3.4. Original femoral neck image versus whole GEM

Table 3.1 Geometrical Parameters of original femoral neck image and whole GEM

Case #	CSA Error (%)	I_{max} Error (%)	I_{min} Error (%)
1	0.70	4.51	0.00
2	0.31	5.00	2.37
3	0.33	1.92	6.22
4	0.00	1.28	2.93
5	0.40	1.55	1.64
6	0.00	3.11	6.04

(a)

(b)

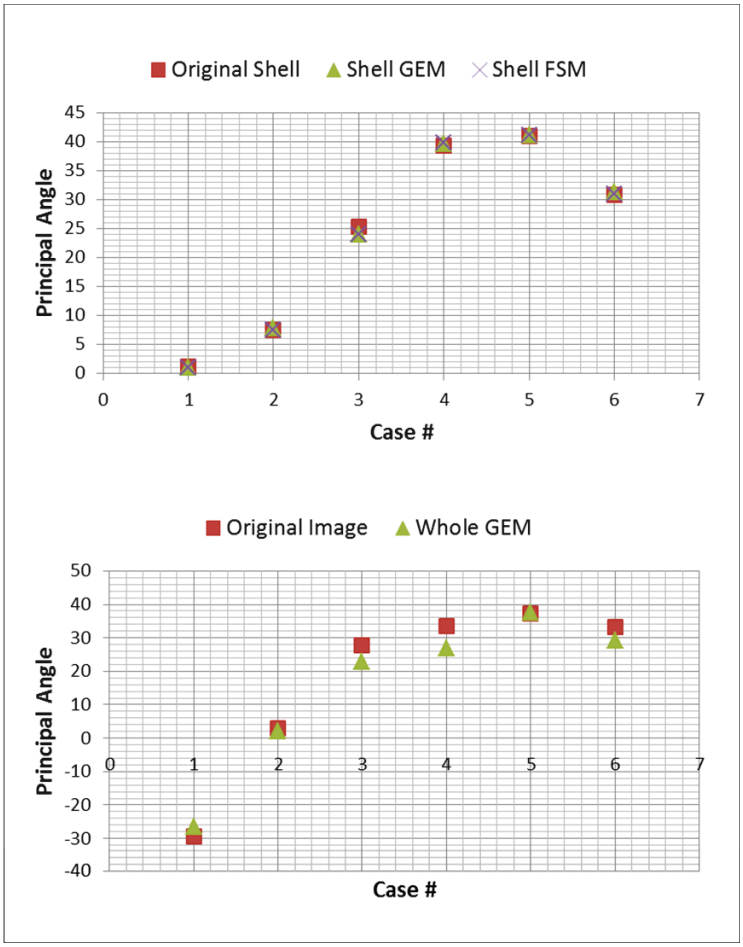

Fig. 3.5 Principal Angle of (a) original shell image, shell GEM and shell FSM (b) original femoral neck image and whole GEM.

3.4. Discussion

We introduced a new algorithm to generate geometrically-equivalent models (GEM) for femoral neck bone cross sections. This will allow the use of these cross sections in further engineering studies and corrects for the low resolution and partial volume fraction effects in the CT image without resorting to the density modulus relationship. GEM models for the shell and for the whole cross-sections were produced using this algorithm. The models were then used in the Finite Strip method. The results indicate that these models are geometrically accurate in preserving the geometrical specifications of the cross sections, and hence can be used safely for engineering analysis. A buckling analysis using these models is described in Chapter 6.

From the results, it is noted that second moment of area has errors in case of whole GEM images that reaches a maximum of 6%. This should be acceptable although its effects must be considered when using the model in fracture or structure analyses. Generally, errors in the second moment of area correspond to errors in the distribution of the points in the mode. This can happen even if the area is preserved. The bone can be perceived as stronger or weaker than normal which can affect the engineering and stress analyses. Since the shell has low errors, the problem originates from the core; modification is needed to the core model to further reduce the moment of inertia error.

As mentioned before, most prior work done on structural behavior used the density-modulus relationship. Here we are avoiding the uncertainties of that method by assigning the modulus of elasticity to a constant value over the bone cross section effectively using the gray level value account for partial volume error, the main source of

its variability in bone. Use of the finite strip method also makes the bone modeling easier, and should improve efficiency of the structure analysis process.

We have provided a FSM for only the shell in this work, another reliable model for core is also needed to be able to incorporate it into the buckling analysis and study its effect in providing strength to bones. Future work will include core modeling, probably using Voronoi tessellation [46]. Voronoi tessellation methods divide the space into regions where each region contains a seed that is specified in the beginning of the operation and where all the points that are closer to this seed than to any other seed. This may be the most suitable way to model the core due to its complex structure especially since image resolution is inadequate.

In conclusion, the proposed GEM and FSM algorithms can be used to generate reliable, geometrically accurate, smooth models of bone cross-sections that can be used in any engineering analysis required. In the future a more accurate model of the core model will be added to the shell FSM to better accommodate the effects of trabecular bone.

Intended to be blank.

Chapter 4

Image Reconstruction from Limited Number of DXA Projections

Relatively high radiation CT techniques are being widely used in diagnostic imaging raising the concerns about cancer risk especially for routine screening of asymptomatic populations. An important strategy for dose reduction is to reduce the number of projections, although doing so with high image quality is technically difficult. We introduce a new algorithm to reconstruct discrete (limited gray scale) images decomposed into individual tissue types from a small number of projections acquired over a limited view angle. The algorithm was tested using projection simulations from segmented CT scans of different cross sections including mid femur, distal femur and lower leg.

4.1. Background

When the number of x-ray projections is constrained by technical or dose limitations, it is nearly impossible to reconstruct high quality continuous images. However, if the imaged object is known to be composed of a small number of different but relatively uniform materials, discrete tomography algorithms can successfully reconstruct images from a limited number of projections [47]. Certain regions of the human body, especially the extremities, can fulfill this requirement since they can be decomposed into adipose, lean tissues, and bone mineral. For applications wherein quantification of tissue composition and its spatial distribution are important, reasonably good accuracy can be obtained with sufficiently small voxels by assuming that they may contain only pure bone, adipose or

lean tissue. This approach assumes negligible variations in tissue attenuation within those discrete categories. Examples of applications where these criteria would hold include measurements of muscle size and shape, fat distribution, and in particular our major focus on bone structural geometry for engineering analysis. Discrete tomography algorithms have been previously demonstrated in several applications including, prostate implants [48], tomographic mammography [49], and neutron imaging [50].

Algebraic reconstruction techniques (ART) [51] have also been employed in reconstruction from limited projection data. For example, simultaneous algebraic reconstruction technique (SART) with a sparsity constraint has been used although a relatively large number of projections, 25-55, are needed [52]. SART has also been used for cone beam reconstruction for breast tomosynthesis from 21 angles in 3° increments over a ±30° angular range [53]. Classical ART along with metric labeling classification has been used for tomographic reconstruction and for segmentation of CT volumes when only a few projection views are available [54]. Sets of 10, 15, and 20 equally spaced projections from the complete rotational set were used.

Discrete algebraic reconstruction technique (DART) is a heuristic discrete tomography algorithm based on an iterative algebraic technique [55]. This algorithm profits from the capabilities of iterative algebraic methods widely used in continuous tomography and incorporates the power of discrete tomography to reconstruct accurate discrete cross sections from relatively few projections. Previous work suggests that five projections can provide satisfactory reconstructions in a simple binary case with no internal voids, whereas ~10 projections are needed for more complex binary images and as many as 18 projections were required for the Shepp-Logan head phantom [55].

In this chapter, we present a modification to the DART method termed: the successive binary algebraic reconstruction technique (SBART) algorithm. SBART uses dual energy x-ray absorptiometry (DXA) projection data that can be decomposed into individual material projections. Using the projections of a single component material and the DART algorithm, binary images of that discrete component can be reconstructed. This binary image can then be used, along with other material projections, as *a priori* constraints to successively reconstruct binary images of individual components until all grey levels are reconstructed into the final discrete image. With this strategy, high quality discrete images can be produced using a remarkably small number of projections.

We also address the advantages of knowing the spatial location of the skin boundary to enhance the SBART algorithm. We are testing an infrared (IR) ranging method, but other methods have also been used to locate the skin boundary. For example, one method used an optical fiber (glass fiber sensor) to sense the location of the body surface for radiation therapy. The advantages of this type of sensor is that, it is visible in a CT scan and is bio-compatible [56]. Another method used infrared to locate and record the motion of the skin surface for respiration tracking in radiosurgery [57]. Another method employed infrared laser displacement sensors (LDS) to detect a respiratory waveform in a similar application[58].

We also hypothesize that if we add a geometrical constraint to SBART, we can further enhance the reconstruction results in case of unknown skin boundary. Here, we are using the second moment of area as a geometrical constraint.

The purpose is to demonstrate the feasibility of the SBART and the Geometrically-Constrained SBART (GC-SBART) algorithms using simulations of DXA

decomposed projections generated from CT scans of lower limbs from de-identified patient scans.

4.2. Methods

4.2.1. ART overview

Let f be a n x n gray scale image with total number of pixels $N=n^2$, and p is the set of parallel rays passing through f. The rays p consist of D detectors in different projection directions N_θ, so total number of rays in all projections is $M = N_\theta D$ [59]. The relationship between f and p may be expressed as [51]:

$$\sum_{j=1}^{N} w_{ij} f_j = p_i, \quad i = 1,2, \dots, M \tag{4.1}$$

where the weighting factors w_{ij} represent the contribution of the jth pixel in the image to the ith ray of the projection. Equation (1) can be expressed as a system of linear equations,

$$Wf = p \tag{4.2}$$

where the M x N matrix W is the projection matrix, the N x 1 vector f represents the pixel values of the image, and the M x 1 vector p represents the set of projection rays.

ART is used to reconstruct the image f from projections p. The basic steps in ART are [51, 59]:

1. Assume an original image $f^{(0)}$, this can be a zero image.
2. Calculate forward projections based on the nth estimation of f

$$p^{(n)} = Wf^{(n)} \tag{4.3}$$

3. Correct the estimation

$$f^{(n+1)} = f^{(n)} - \frac{\left(w_i f^{(n)} - p_i\right)}{w_i w_i^T} w_i^T \tag{4.4}$$

Where the projection index *i* is distributed randomly.

4. Repeat steps 2 and 3 until the change in consecutive images values falls below a preset threshold.

The projection matrix *W* depends on image size, number of projections and detectors (rays) used. Therefore, an accurate reconstruction requires considerable computational resources. To minimize the burden in computing *W*, various approximations of the projection matrix can be used. Here, we use the nearest neighbors method [59]. As shown in Fig 4.1, the center of each pixel in the image *f* has a quadratic neighborhood of the size b^2, where *b* is the pixel spacing. The distance between the beam and the center of the pixel $\mathfrak{z}'$ can be determined by:

$$\mathfrak{z}' = \mathfrak{z}_d - (x_k \cos(\gamma_r) + y_l \sin(\gamma_r)) \tag{4.5}$$

where $\mathfrak{z}_d$ is the shortest distance from the origin to the beam, γ_r is the projection angle, and (x_k, y_l) is the center of the pixel. Then weights w_{ij} are assigned a value according to the rule:

$$\begin{aligned} if \quad & \left|\mathfrak{z}' \cos(\gamma_r)\right| < \frac{b}{2} \quad or \quad \left|\mathfrak{z}' \sin(\gamma_r)\right| < \frac{b}{2} \\ then \quad & w_{ij} = b \\ \text{else} \quad & w_{ij} = 0 \end{aligned} \tag{4.6}$$

4.2.2. DART Algorithm

The DART algorithm is described in detail in the references [55, 60]. The outline of the algorithm is as follows:

1. Compute a preliminary reconstruction $f^{(0)}$ using a small number of ART iterations.
2. Segment the image into its main gray levels.

$$s^{(n)} = r\left(f^{(n-1)}\right) \tag{4.7}$$

where $f^{(n-1)}$ is the estimated image after *n-1* iterations, $s^{(n)}$ is the segmented image, and *r* is the threshold function defined as

$$r(v) = \begin{cases} \rho_1, & v < \tau_1 \\ \rho_2, & \tau_1 \le v < \tau_2 \\ \dots\dots & \\ \rho_l, & \tau_{l-1} \le v \end{cases} \tag{4.8}$$

where $\{\rho_1, \rho_2, \dots\dots, \rho_l\}$ is the set of gray levels in the reconstructed image and τ_i is calculated as

$$\tau_i = \frac{\rho_i + \rho_{i+1}}{2} \; for \; i = 1,2, \dots\dots, l-1 \tag{4.9}$$

where *l* is the number of gray levels.

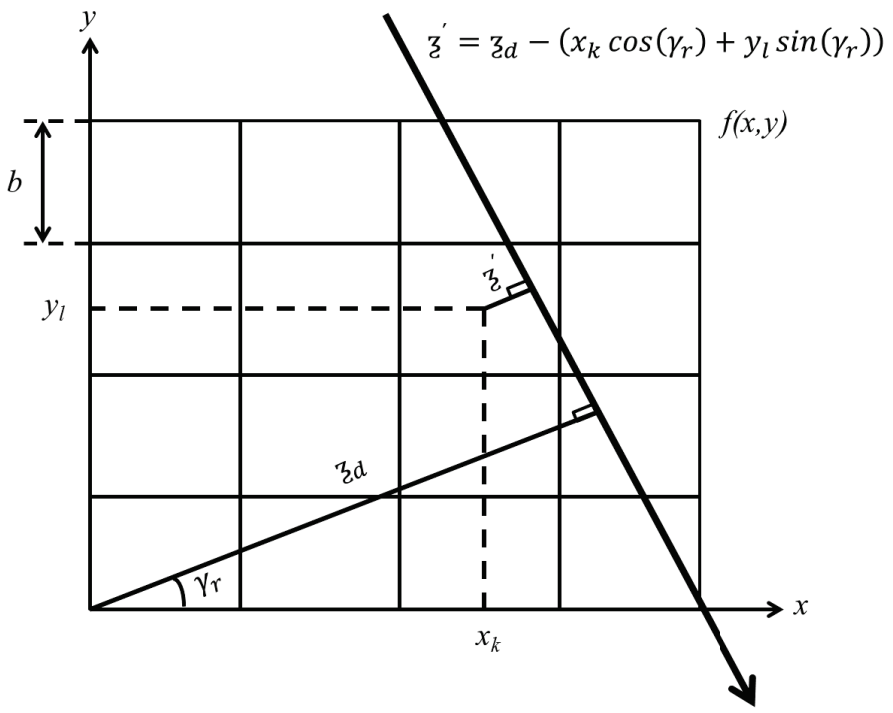

Fig. 4.1. Determination of the weights w_{ij} of the projection matrix using the nearest neighbors method.

3. Divide the resultant image $s^{(n)}$ into boundary $B^{(n)}$ and non-boundary $I^{(n)}$ sets of pixels, where a pixel is considered non-boundary if it and all 8-connected neighboring pixels have the same gray level.
4. Compute the image $g^{(n)}$ from $f^{(n-1)}$ and $s^{(n)}$ such that

$$g_i^{(n)} = \begin{cases} s_i^{(n)} & if\ i \in I^{(n)} \\ f_i^{(n-1)} & if\ i \in B^{(n)} \end{cases} \tag{4.10}$$

5. Using $g^{(n)}$ as a starting image, perform one ART iteration, leaving non-boundary pixels unchanged.
6. Apply a local smoothing operator to the boundary pixels $B^{(n)}$,

$$f_i^{(n)} = 0.7 f_i^{(n)} + 0.3b \tag{4.11}$$

where b is the average gray level in the 8-neighborhood of pixel i.

7. Repeat steps 2 to 6 until a stop criterion is met.

4.2.3. SBART Algorithm

The essence of the proposed SBART algorithm is to use the individual projections of each discrete tissue type extracted from dual energy scans to reconstruct the tissue as a binary set of voxels, before proceeding to the next tissue. During each reconstruction step, the previous reconstruction results are used as *a priori* constraints on the following step. In the final step, the voxels resulting from the individual tissue reconstructions are combined in the cross section. Using this approach, the problem is simplified by reducing uncertainties in each step of the reconstruction. The SBART algorithm is outlined in Fig. 4.2 for the case of the three tissues: fat, lean, and bone.

The SBART algorithm performs the following steps:

1. The bone image is reconstructed first using DART with soft–tissue-subtracted bone projections acquired from DXA data. The prior information is a mask constructed from the intersection of bone outer boundaries from all bone projections constraining the reconstruction to mask boundary. If projections are noisy, noise suppression takes place outside the boundary by thresholding the projection to 10% of the maximum projection value.

If the skin boundary is known, steps 2a-3a are performed:

2a. Fat voxels are reconstructed using DART and DXA fat projections. Bone voxels reconstructed in step 1 as well as the skin boundary are used to constrain the reconstruction, i.e., fat voxels are reconstructed only within the skin boundary avoiding bone voxels. In case of noisy projections, thresholding is done as with bone projections.

3a. Given the reconstructed bone and fat voxels, the remaining voxels within the skin boundary are assigned to lean without requiring further reconstruction.

If the skin boundary is unknown, use alternative steps 2b-3b:

2b. Fat voxels are reconstructed using DART from DXA fat projections. A crude mask is created using the intersection of skin outer boundaries from all projections constraining the reconstruction to within the mask, excluding previously reconstructed bone voxels. If noisy, thresholding is done as with bone projections.

3b. Lean voxels are finally reconstructed using DART algorithm and DXA lean projections. As in step 2b, bone and fat voxels reconstructed in the previous steps as well as the mask are used to restrict the reconstruction. If lean projections are noisy, thresholding takes place but with a threshold value of only 5% of the maximum projection value. This is because lean projections have small values in some areas especially around the skin boundary; thresholding at a higher level distorts projections with greater reconstruction errors.

Finally,

4. The bone, fat and lean binary voxels are each assigned discrete grey scale values to form the final image consisting of four gray levels including air.

5. To correct for isolated voxels of one tissue or air voxels within the cross section, a neighborhood connectivity test of each voxel is performed. Out of its eight neighbors, a voxel with more than 4 neighboring nonzero voxels, is assigned the value of the voxel with the most repeated gray level in its eight-neighborhood. If not, the voxel is assigned to zero (air). This step is repeated until no change occurs in the final image. In our experience, two repetitions were sufficient to exclude isolated voxels. This step, unneeded if the skin boundary is known, becomes more important with noisy data. Noise increases the number of isolated and air voxels air within the cross section.

The iterations in step 1, 2 or 3 are terminated if the total projection error E defined in equation (4.12) decreases by less than 1% over the previous five iterations.

$$E = \|Wf - p\|_2 \tag{4.12}$$

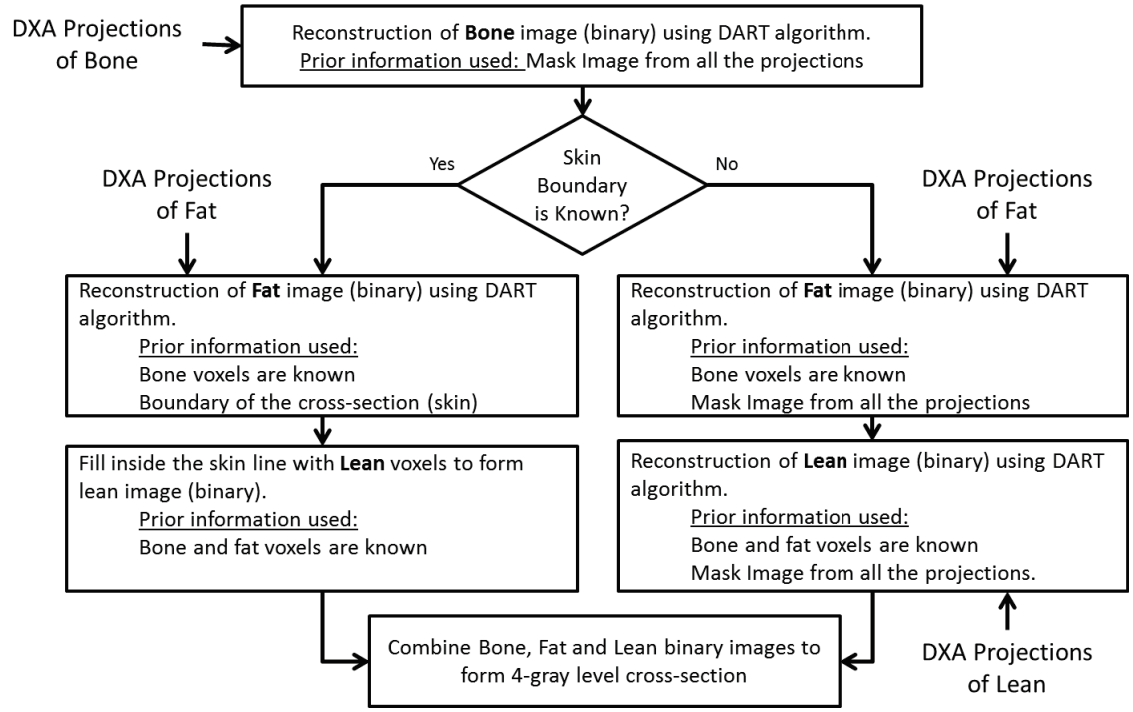

Fig. 4.2. The successive binary algebraic reconstruction technique (SBART) Algorithm.

4.2.4. GC-SBART Algorithm

In geometrically-constrained SBART (GC-SBART), the second moment of area is used to further enhance the reconstruction especially in case of unknown skin boundary. The second moment of area is defined before in equations (3.1) to (3.4). These equations are repeated here for convenience:

$$I_x = \int \mathrm{y}^2 \, \mathrm{dA} \tag{3.1}$$

$$I_y = \int \mathrm{x}^2 \, \mathrm{dA} \tag{3.2}$$

$$I_{xy} = \int \mathrm{xy} \, \mathrm{dA} \tag{3.3}$$

$$I_\theta = \frac{I_x + I_y}{2} + \frac{I_x - I_y}{2} \cos 2\theta - I_{xy} \sin 2\theta \tag{3.4}$$

To use the second moment of area with SBART, a new geometrically-constrained (GC) iteration step is added inside the reconstruction loop of fat and lean images. We are not using this constraint with bone reconstruction since it good results are obtained with very small geometrical errors with DART alone.

As in ART equations (4.3) and (4.4), we can use the following GC equations:

$$I^{(n)} = V f^{(n)} \tag{4.13}$$

$$f^{(n+1)} = f^{(n)} - \frac{\left(v_i f^{(n)} - I_i\right)}{v_i v_i^T} v_i^T \tag{4.14}$$

where I and V are defined as

$$I = \begin{bmatrix} I_0 \\ \vdots \\ I_{179} \end{bmatrix} \tag{4.15}$$

and

$$V = \begin{bmatrix} R_0(x^2) \\ \vdots \\ R_{179}(x^2) \end{bmatrix} \tag{4.16}$$

Each row of V is $R_\theta(x^2)$ where R_θ is a rotating operator and θ is from 0° to 179°, and each row of I is the second moment of area calculated at angles 0° through 179°.

To calculate I_θ at each angle, second moment of area I_y, I_{45}, and I_x at angles 0°, 45°, and 90° respectively are calculated from the corresponding projections. These projections are included in every set of projections used from three to 13 projections. Using $I_\theta = I_{45}$ and $\theta = 45°$ in equation (3.4) and solve for I_{xy} :

$$I_{xy} = \frac{I_x + I_y}{2} - I_{45} \tag{4.17}$$

Knowing I_x, I_y, and I_{xy}, we can calculate I_θ at each angle from 0° to 179° using equation (3.4).

The GC-SBART algorithm performs the following DART-GC iterations to reconstruct fat and lean binary images:

1. Compute a preliminary reconstruction $f^{(0)}$ using a small number of ART iterations.
2. Segment the image into its two gray levels (binary image).

$$s^{(n)} = r\left(f^{(n-1)}\right) \tag{4.18}$$

where $f^{(n-1)}$ is the estimated image after *n-1* iterations, $s^{(n)}$ is the segmented image, and *r* is the threshold function defined as

$$r(v) = \begin{cases} 0, & v \leq 0.5 \\ 1, & v > 0.5 \end{cases} \tag{4.19}$$

3. Divide the resultant image $s^{(n)}$ into boundary $B^{(n)}$ and non-boundary $I^{(n)}$ sets of pixels, where a pixel is considered non-boundary if it and all 8-connected neighboring pixels have the same gray level.

4. Compute the image $g^{(n)}$ from $f^{(n-1)}$ and $s^{(n)}$ such that

$$g_i^{(n)} = \begin{cases} s_i^{(n)} & if\ i \in I^{(n)} \\ f_i^{(n-1)} & if\ i \in B^{(n)} \end{cases} \tag{4.20}$$

5. Using $g^{(n)}$ as a start image, perform one ART iteration as in equation (4.21), leaving non-boundary pixels unchanged.

$$f^{(n+1)} = f^{(n)} - \lambda_1 \frac{\left(w_i f^{(n)} - p_i\right)}{w_i w_i^T} w_i^T \tag{4.21}$$

where λ_1 is a parameter to specify step length.

6. Apply a local smoothing operator to the boundary pixels $B^{(n)}$,

$$f_i^{(n)} = 0.7 f_i^{(n)} + 0.3b \tag{4.22}$$

where b is the average gray level in the 8-neighborhood of pixel i.

7. Repeat steps 2 to 5 with the exception of using GC equation (4.23) instead of equation (4.21),

$$f^{(n+1)} = f^{(n)} - \lambda_2 \frac{\left(v_i f^{(n)} - I_i\right)}{v_i v_i^T} v_i^T \tag{4.23}$$

where λ_2 is a parameter to specify step length.

8. Repeat steps 2 to 7 until a stop criterion is met.

While performing these iterations, the same prior information are used as in SBART. The parameters λ_1 and λ_2 can be changed to maximize the effect of the geometrical constraint. In this work, we used $\lambda_1 = \lambda_2 = 0.5$.

4.3. Simulations

4.3.1. Projections Simulation

In the proposed application, DXA data would be used for this method, but the algorithm separating lean and fat tissues from projection rays containing bone is a separate development effort (described in Chapter 5). To avoid these uncertainties, human leg CT images were used in our simulations since simple thresholding can be used to separate the tissues into the three components (plus air). Images were reconstructed on a 256x256 matrix with a pixel spacing b = 0.488 mm.

Different numbers of equally-spaced projections were created between 0° and 90° consistent with the design of the multiple projection DXA system. In the simulations each leg cross-section was separated into its three main (uniform) components using simple thresholding (Fig. 4.3), and projections were generated for individual tissues.

Assuming that the skin boundary is detected by an independent method, the boundary of the leg cross-section is known. Our simulations consider both cases of known and unknown skin boundary as described in the previous section.

4.3.2. Image Reconstruction

Cross sections at three locations were used in simulations at mid-femur, distal femur and lower leg. In case of known skin boundary, sets of 3, 5, 7, 9, and 11 equally-spaced projections between 0° to 90° were used. When the skin boundary was unknown, sets of 5, 7, 9, 11, and 13 equally-spaced projections between 0° to 90° were used.

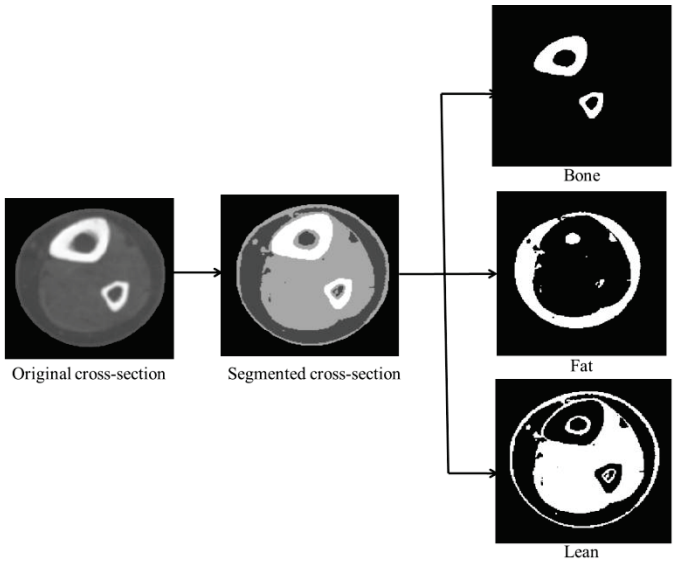

Fig. 4.3. Separation of the cross-section into its basic materials. Original CT image (left) is segmented into 4 grey levels (middle) showing bone (white), fat (dark grey),lean (light grey) and air (black). Individual tissues are shown on right.

To test the effect of noise on the robustness of the reconstruction algorithm, noisy projections were simulated. Since the number of photons emitting from the x-ray source is random and follows a Poisson distribution [61, 62], line integrals (projections) were converted into x-ray intensity using incident fluences of 10^3 and 10^4 photons in cases of low and high energy, respectively, and Poisson noise was added. Assuming 100% detector quantum efficiency (DQE), the detected intensity was then transferred back to line integrals, creating noisy projections [63]. Reconstruction using the SBART algorithm took place next using those projections. Coefficients of variation (CV), defined as the ratio between the standard deviation of the noise and the signal mean, were calculated for every projection to express noise magnitude.

4.3.3. Quality Indices

Pixel error and geometrical measurements such as cross-sectional area (A), center of mass (CM), and second moment of area (I) over the entire image were used as indices to evaluate reconstructed image quality. These geometrical parameters were used to ensure the reconstructed cross-section is sufficiently accurate for engineering analyses; the anticipated main application of the reconstructed discrete image.

Pixel error was defined as the percentage ratio between the number of mismatched pixels between the original and the reconstructed images, and the total number of tissue-filled (nonzero) pixels in the original image.

The area of each tissue type is calculated as:

$$A_t = b^2 n_t \tag{4.24}$$

and the total area is

$$A = \sum_{t=1}^{T} A_t \tag{4.25}$$

where b is the pixel spacing, n_t is the total number of voxels of segmented tissue t in the image and T is the number of segmented tissues. The percentage error in A_t is then calculated:

$$\varepsilon_{A,t} = \frac{A_{t,rec} - A_{t,org}}{A_{t,org}} \times 100 \tag{4.26}$$

where $A_{t,org}$ and $A_{t,rec}$ are the areas of tissue t in the original and reconstructed images, respectively.

The center of mass is located at coordinates $(\bar{x}, \bar{y})$ as shown previously in equations (3.7) and (3.8). The Euclidean distance between center of mass of the original image and that of the reconstructed image is then calculated:

$$\varepsilon_{CM} = \sqrt{(\bar{x}_{org} - \bar{x}_{rec})^2 + (\bar{y}_{org} - \bar{y}_{rec})^2} \tag{4.27}$$

Finally the maximum absolute percentage error in the second moment of area I is then calculated as:

$$\varepsilon_I = max_\theta \left| \frac{I_\theta^{rec} - I_\theta^{org}}{I_\theta^{org}} \right| \times 100 \tag{4.28}$$

where I_θ is calculated at each angle from 0° to 180° from the original and reconstructed images.

4.4. Results

Fig. 4.4 shows the original segmented image of each cross section in the first column and the reconstructed images using different number of projections in subsequent columns in case of known skin boundary. In the first row, in comparison to the original segmented image, the reconstructed mid-femur images using 11 projections is not superior to the image reconstructed from 9 projections. The same is true for the lower leg image in the third row. In the second row, it is apparent that the more complex distal femur image continually improves with increasing numbers of projections.

Fig. 4.5 shows reconstruction results for the case when the skin boundary is unknown. It is apparent that more projections are needed to achieve good quality images, vs. known skin boundary. At the mid-femur, the quality of the reconstructed image using 13 projections is comparable to the reconstruction using 11 projections (Fig. 4.4) except at the skin margin. The same is true for the lower leg image moreover it has high quality at edges. The distal femur image requires more projections to reach an acceptable quality.

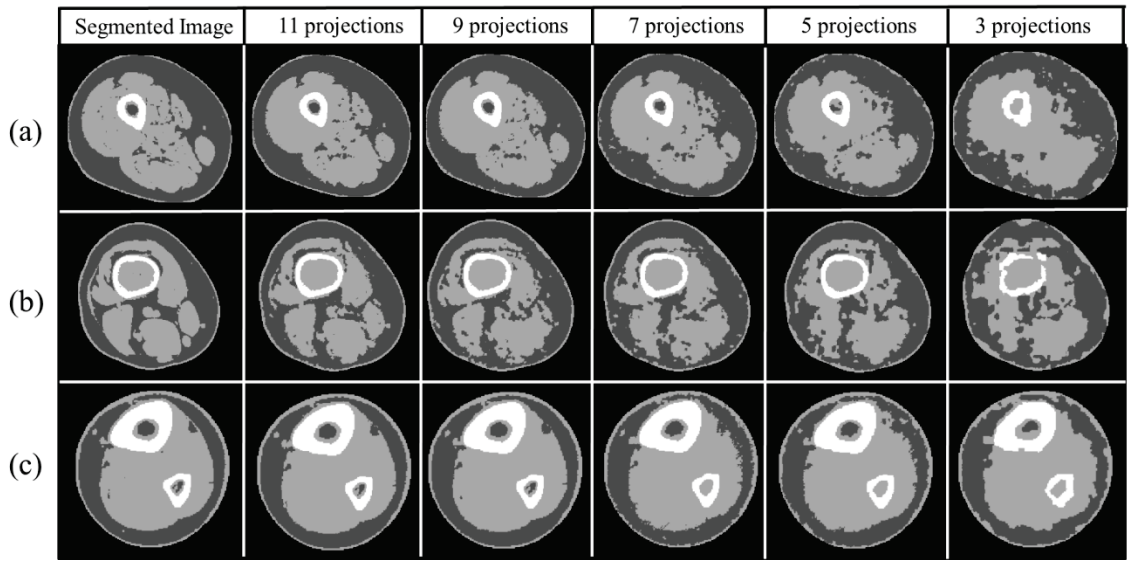

Fig. 4.4. Reconstructed images using SBART algorithm from different number of projections in case of known skin boundary for (a) mid-femur, (b) distal femur, and (c) lower leg cross sections.

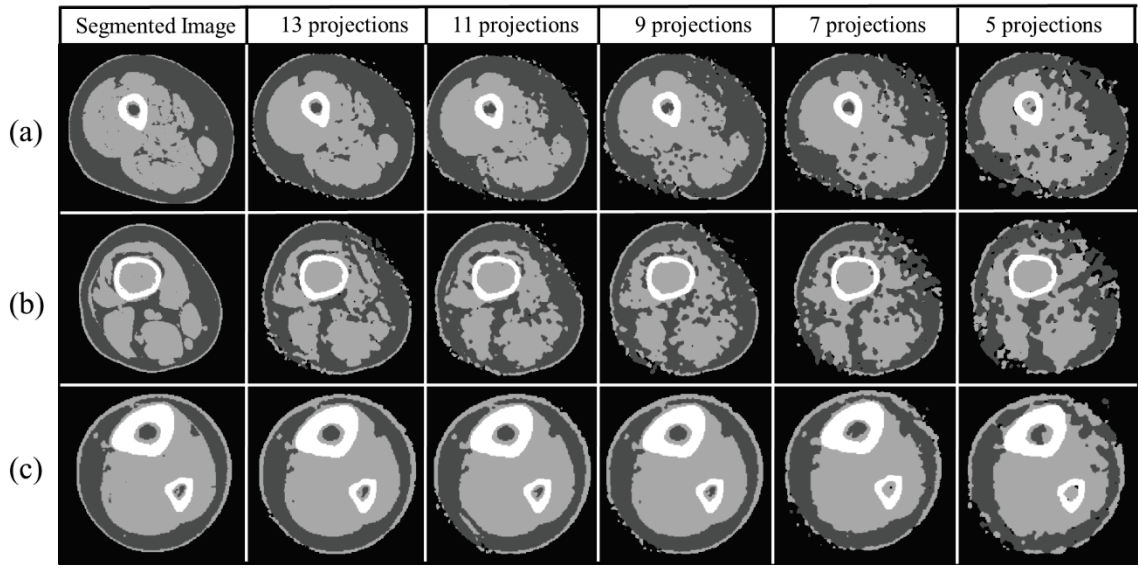

Fig. 4.5. Reconstructed images using SBART algorithm from different number of projections in case of unknown skin boundary for (a) mid-femur, (b) distal femur, and (c) lower leg cross sections.

Fig. 4.6 plots the pixel error of the reconstructed images from different number of projections with and without skin boundary. The pixel error of images reconstructed with known skin boundary is shown in solid lines, with unknown skin boundary in dotted lines. For mid femur images, with known skin boundary the error is 13.1% with three projections; reducing to 2.4% with 11, vs. unknown skin boundary where the error ranges from 20.3% at 5 projections to 5.5% with 13. Similarly, for the distal femur image, error ranges from 20.7 % to 5.5% and 31. 0% to 13.3% for known and unknown skin boundaries, respectively. Finally, in the lower leg image which gives the best results, pixel error is in the range of 8.9% to 0.6% and 14.5% to 3.3% in cases of known and unknown skin boundaries, respectively. Generally, pixel error is greater with unknown skin boundary, and improves with number of projections.

Percentage error in area (ε_A) in all three cross sections is shown in Fig. 4.7. It is apparent that error is much higher if the skin boundary is unknown. Interestingly, the error in area in the whole cross section is negligible (<0.1%) regardless of the number of projections used in case of known skin boundary. The average error in the center of mass (ε_{CM}) is 0.08±0.12 mm and 0.27±0.10 mm in the two cases and reaches a maximum value of only 0.48 mm .

Fig. 4.8 shows the maximum absolute percentage error in second moment of area (ε_I) for the reconstructed images using different numbers of projections under both conditions. As before, there is considerable improvement if the skin boundary is known. The range of error with the skin boundary is only 0.07%-0.8% vs. 1.8-7.4% without. In these simulations the number of iterations averaged 72, ranging from 46 to 115.

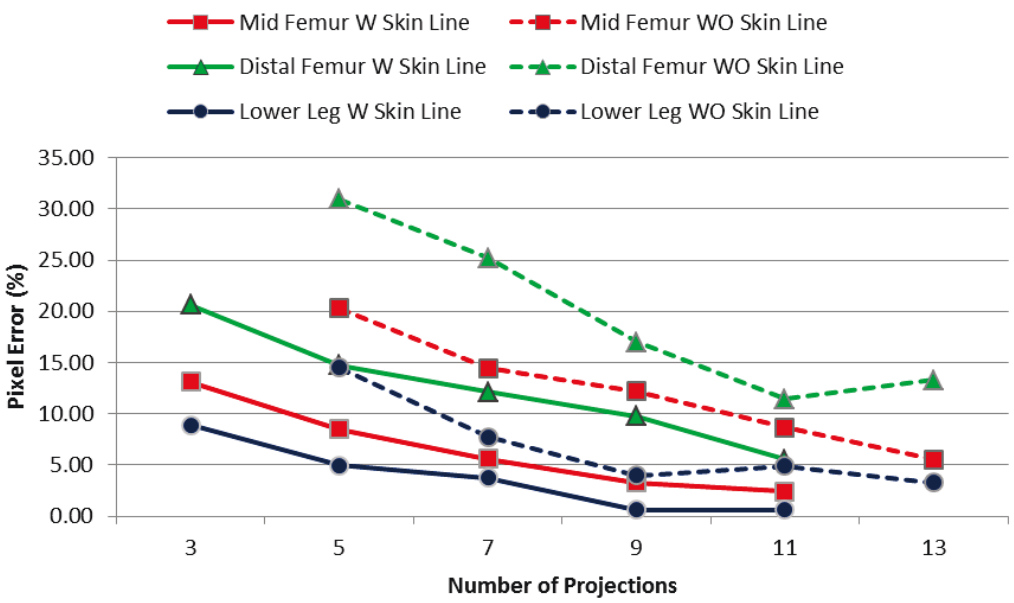

Fig. 4.6. Pixel error (in percentage %) in reconstructed images using SBART algorithm from different number of projections with and without knowledge of the skin boundary.

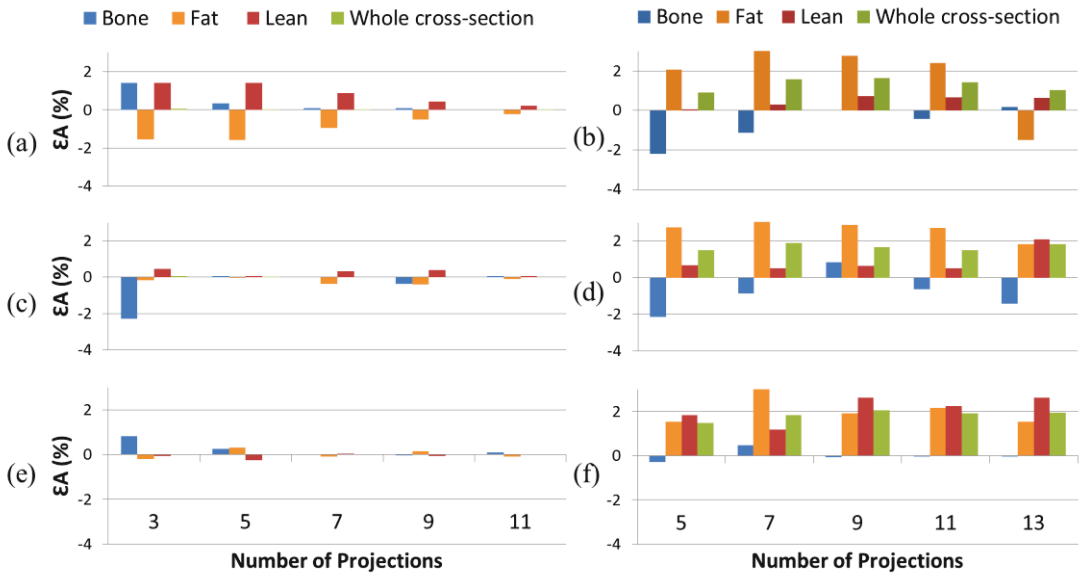

Fig. 4.7. Percentage error in the area of the reconstructed images using SBART algorithm in case of mid-femur (a,b), distal femur (c,d) and lower leg (e,f) with different number of projections with (a,c,e) and without (b,d,f) the skin boundary.

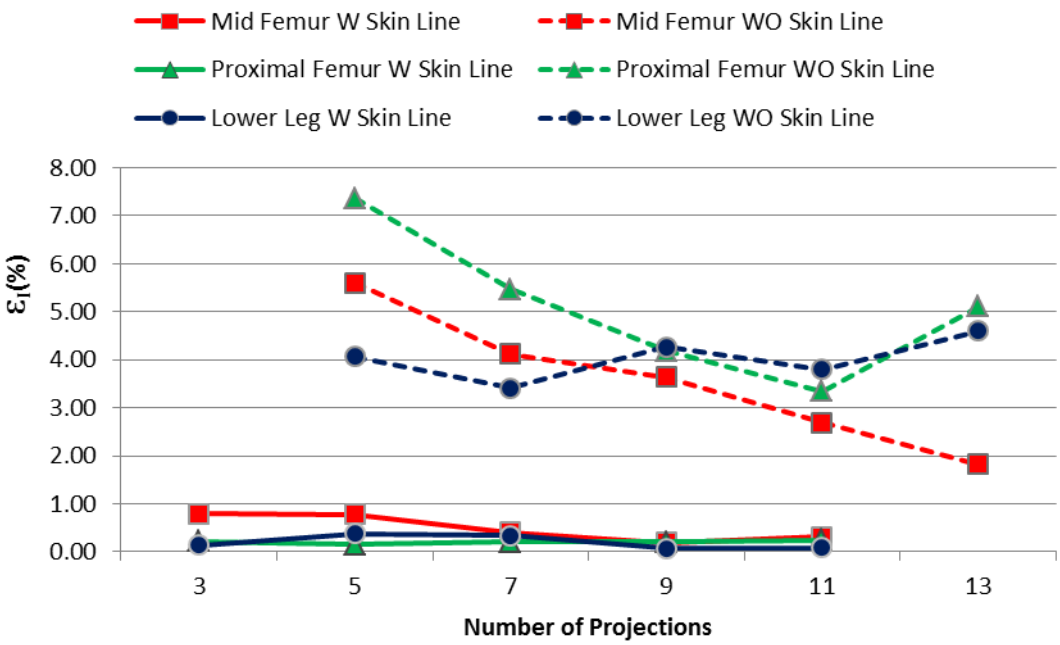

Fig. 4.8. Maximum absolute percentage error in the second moment of area of the reconstructed images using SBART algorithm with different number of projections with and without knowledge of the skin boundary.

Fig. 4.9 compares reconstructed images labeled with pixel error using SBART and DART algorithms in case of unknown skin boundary. Image quality is clearly better with the SBART method compared to DART.

Table 4.1 shows the mean and standard deviation of coefficient of variation (%) over the all 13 projections for bone, fat, and lean tissues to express the amount of noise added.

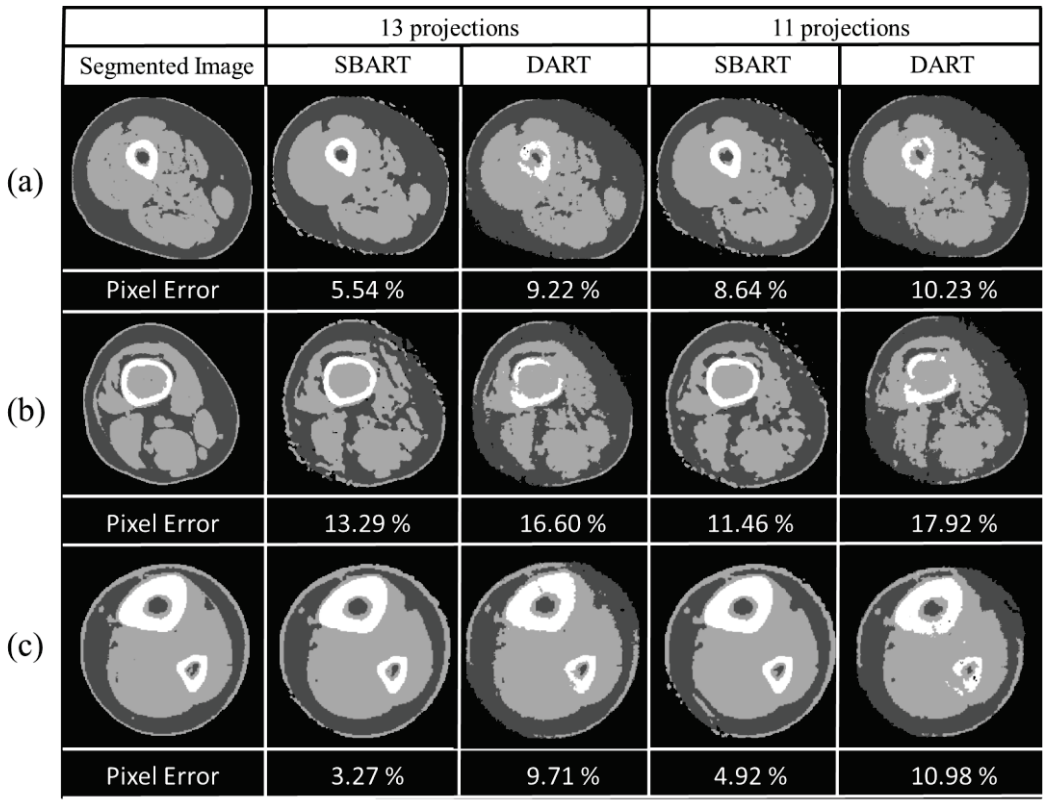

Fig. 4.9. Comparison between reconstructions with unknown skin boundary using SBART and DART algorithms with 11 and 13 projections for (a) mid-femur (b) distal femur and (c) lower leg cross sections.

Table 4.1. Mean and standard deviation of coefficient of variation (%) over all projections for each tissue type.

Tissue Type	CV (%)
Bone	3.5±0.4
Fat	6.8±0.8
Lean	5.1±0.6

The effect of noise on reconstruction was tested on the mid-femur cross-section. Pixel error in reconstructed images from different number of projections with and without knowledge of the skin boundary is shown in Fig. 4.10. The pixel error of images reconstructed with known skin boundary is shown (a), with unknown skin boundary in (b). Reconstruction done using noise-free projections is shown in solid lines, with noisy projections with dotted lines. The error of reconstrution from noisy data is higher than without but it also improves with more projections. The error is about 14% with three projections and drops to 7% with 11 projections with known skin boundary vs. 21.8% with five projections improving only to 13% with 13 projections without known skin boundary.

Percentage error in area (ε_A) in reconstruction from noisy projections remains low (<1.3%) and the error in the center of mass (ε_{CM}) is below 0.48 mm in both cases. The maximum absolute percentage error in second moment of area (ε_I) for the reconstructed images using different numbers of projections averages 4% in case of known skin boundary and 5.5% if it is unknown.

Reconstructed images using GC-SBART algorithm with unknown skin boundary are shown in Fig. 4.11. Comparing with Fig. 4.5, it is apparent that the images are with better quality than those reconstructed using SBART algorithm especially around skin boundary.

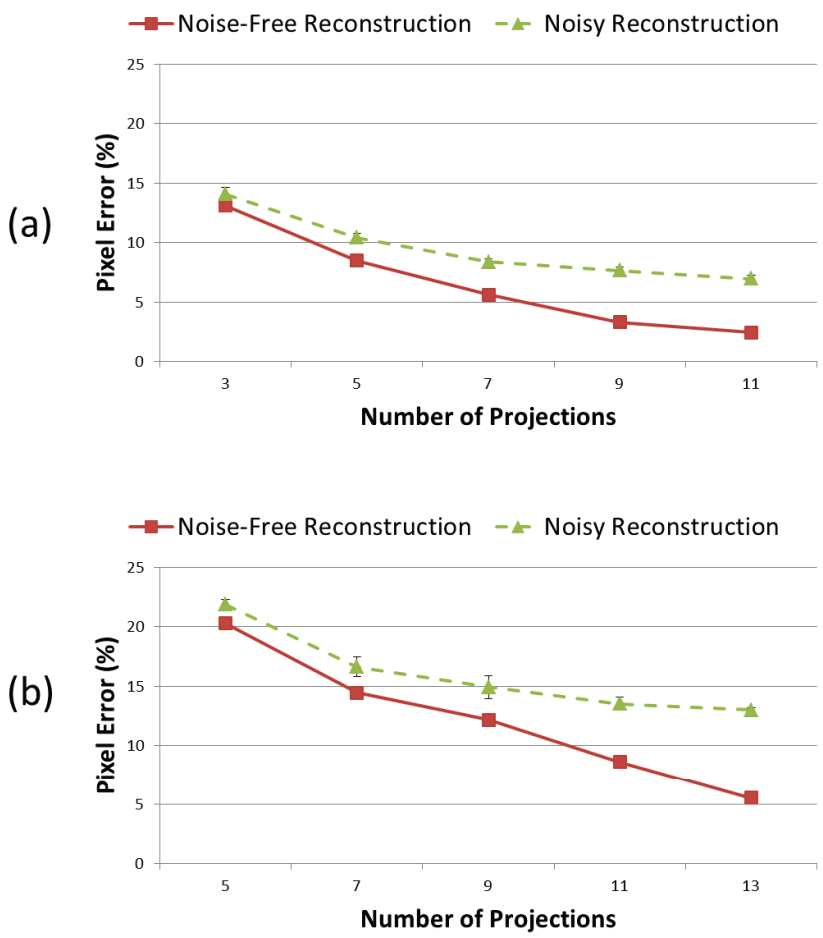

Fig. 4.10. Pixel error (in percentage %) in mid-femur reconstructed images using SBART algorithm from different number of projections (a) with and (b) without knowledge of the skin boundary.

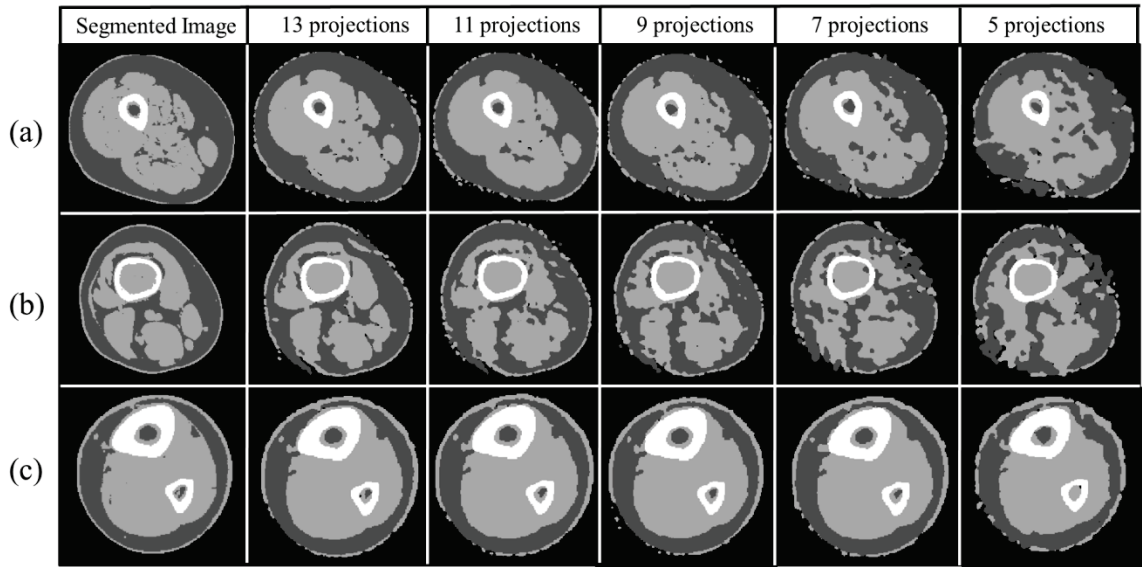

Fig. 4.11. Reconstructed images using GC-SBART from different number of projections with unknown skin boundary for (a) mid-femur, (b) distal femur, and (c) lower leg cross sections.

Fig. 4.12 presents the pixel error of the reconstructed images from different number of projections without the knowledge of the skin boundary using SBART (solid lines) and GC-SBART (dotted lines) reconstruction algorithms. The pixel error is reduced with an average of 23%, 4%, and 8% for mid-femur, distal femur, and lower leg cross-sections respectively. Percentage error in area (ε_A) is also reduced as shown in Fig. 4.13 with an average of 27%, 2%, and 23% for the same cross-sections in order.

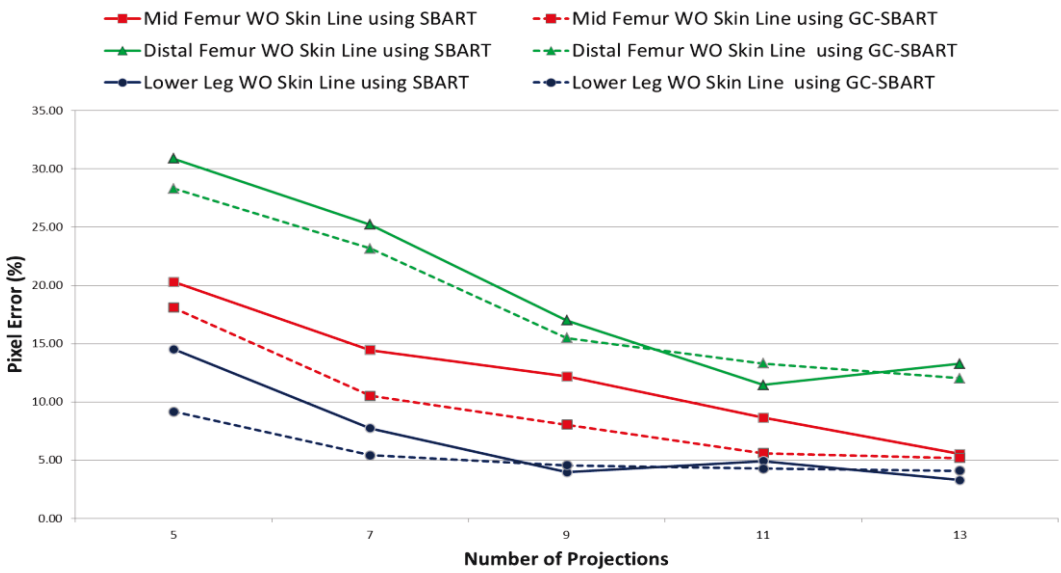

Fig. 4.12. Pixel error (in percentage %) in reconstructed images from different number of projections with unknown skin boundary using SBART and GC-SBART reconstruction algorithms.

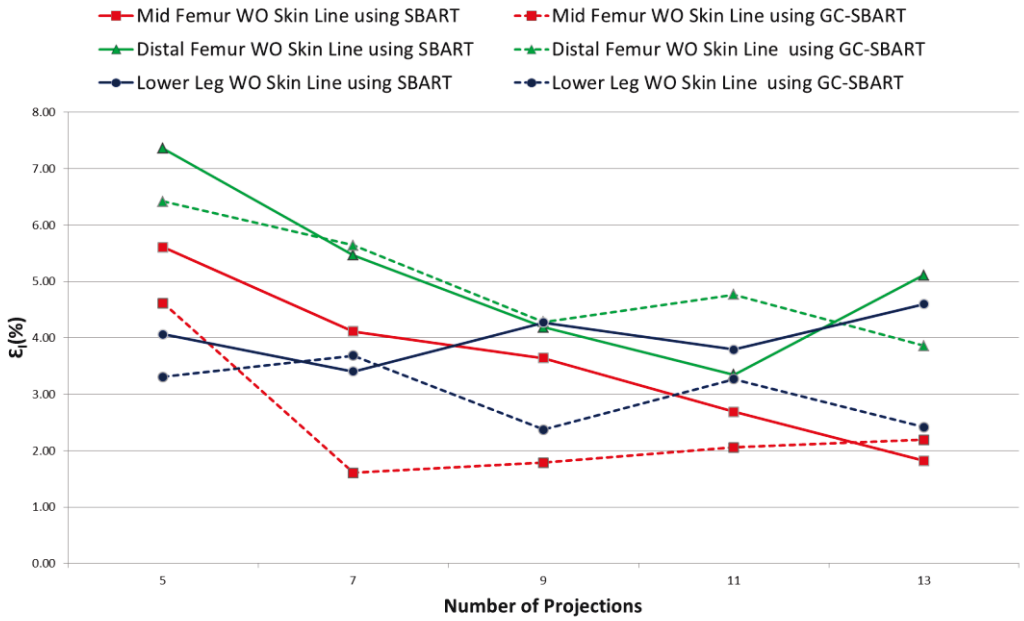

Fig. 4.13. Maximum absolute percentage error in the second moment of area of the reconstructed images with different number of projections with unknown skin boundary using SBART and GC-SBART reconstruction algorithms.

4.5. Discussion

Currently there is considerable concern about the cancer risk from the widespread use of high radiation CT techniques in clinical medicine. Radiation concern is heightened in imaging of sensitive populations like children and in screening procedures where radiation risk is not necessarily balanced by the presence of known disease. A good example of the latter is in screening of osteoporosis, a totally symptomless disease causing bone fragility. To a first order, the dose is a function of the number of projections thus can be reduced in 3D imaging by reconstructing images with fewer projections. Considering that typical reconstructions require 240-360 projections or more, a reduction to as few as 5 projections at two energies could reduce dose by an order of magnitude.

In the method described here, we take advantage of the fact that fewer projections are needed if the image volume consists of a limited number of discrete materials with differing attenuation properties. The SBART algorithm reconstructs individual discrete tissues in sequence under conditions where the projection data can be decomposed into discrete component tissues. Our ultimate goal is to implement this algorithm with dual energy x-ray absorptiometry (DXA) data which has the capacity to differentiate projection data into two components. An iterative algorithm for completely separating dual energy projection data into three components over the entire projection is described in Chapter 5. Here we have avoided DXA uncertainties in demonstrating the SBART reconstruction principle by thresholding CT scans into three tissue components. Overall, our results demonstrate that the SBART algorithm provides excellent reconstruction quality with a small number of projections restricted in angle.

SBART also yields superior results over the DART method when the same number of projections is reconstructed. This is because individual tissues are completely reconstructed using *a priori* constraints before proceeding to the next tissue. The effect is apparent in Fig. 4.9, especially for bone tissue which is critically important in osteoporosis diagnosis. The SBART algorithm can be generalized to more than three materials provided that there exists a method for reliable decomposition of projection data into the individual discrete materials.

The principle application of this work is in deriving structural geometry of bone cross-sections for use in a 3D engineering models. Critical geometric properties of cross-sections are the bone cross-sectional area and second moment of area, governing load stresses in axial compression and bending, respectively. Errors in those parameters ranged between 2% and 8% when the skin boundary is unknown, but were reduced to <1% with a known skin boundary reconstructed with as few as 5 projections. We are currently investigating several independent methods for mapping the skin boundary.

Because the lean tissue boundary is very thin, it is relatively susceptible to reconstruction errors from the nearby large fat region (Fig. 4.5 and Fig. 4.9). The inclusion of prior knowledge of the skin boundary and/or other reconstruction constraints further improves the accuracy of this boundary. Adding a geometrical constraint such as the second moment of area as in GC-SBART algorithm enhances the solution in such case (as shown in Fig. 4.11).

The reconstruction using GC-SBART algorithm, if the skin boundary is unknown, gives better image quality especially around the boundaries. It also reduces the pixel and second moment of area errors by a significant amount in case of mid-femur and lower leg

cross-sections. The distal femur cross-section however, is only slightly improved. This may be due the complexity of the cross-section which makes the reconstruction more difficult and requires more projections to yield an image comparable to other cross-sections used here.

Because GC-SBART consists of the combined DART-GC iterations compared to DART iterations only in SBART, the time required for reconstruction is considerably longer. This is the cost of achieving a good reconstruction results without knowing the skin boundary. We conclude that a method that incorporates an independent measurement of the skin boundary with the SBART algorithm is preferred over the GC-SBART algorithm. Nevertheless for cases when it is not possible to measure the skin boundary, the GC-SBART approach is a viable method for achieving good reconstructions.

We have not yet determined exactly how many projections will be required in reconstruction in all cases; this appears to be dependent on complexity of the cross-section, the accuracy required, and the application. For cross-sectional geometry calculations in bone it appears that 5-7 projections will usually be sufficient when the skin boundary is known, although more may be needed for better accuracy in regions containing a lot of trabecular detail.

One of the drawbacks of the clinical CT images used in our simulations is that resolution was inadequate to resolve trabecular bone. Trabeculae should appear at least as scattered voxels within the inner cortical boundary of cross-sections near joints. Future studies with a higher resolution data set sufficient to resolve trabeculae are in the planning stages.

Reconstruction of discrete images can be useful in diagnosis of diseases involving quantitative tissue discrimination, such as osteoprosis (or bone thinning) as mentioned before, and muscle dystrophy [64, 65] which is genetic disorder gradually weakens the muscles and that may be characterized by measurements of muscle size or volume. The SBART and GC-SBART methods will permit reconsructions of entire limb volumes using a series of discrete projections along the limb thus providing a 3D image of the limb from which we can generate a valid 3D model. One example of a 3D forearm reconstructed from a series of 2D cross secions is shown in Fig 4.14. Mechanical and structural analyses can then be applied to the 3D model, so that load stresses can be computed in physiologic and traumatic loading conditions. This type of research will be valuable in the study of osteoporosis, and other musculoskeltal diseases.

In conclusion, the SBART and GC-SBART algorithms can be used to reconstruct high quality discrete images from a remarkably limited number of projections decomposed into individual tissue types in case of known and unknown skin boundary.

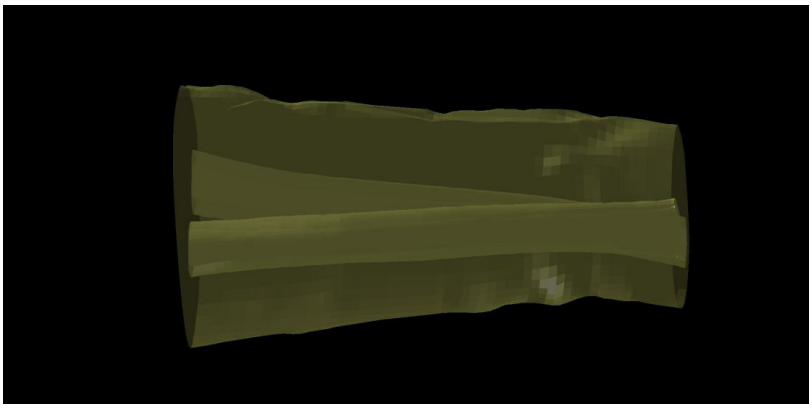

Fig. 4.14. 3D Model of human cadaveric forearm constructed from series of 2D cross sections.

Chapter 5

Material Decomposition of Bone Cross Sections from Limited Number of DXA Projections

To reduce the dose burden to the patient compared to conventional CT image, we previously proposed the successive binary algebraic reconstruction technique (SBART) algorithm to reconstruct discrete cross sections from a small number of dual energy x-ray absorptiometry (DXA) projections decomposed into individual tissue components (bone, fat, and lean) as shown in chapter 4. This algorithm could generate high quality cross sections from as few as five projections. However, to be able to use this algorithm, all projections of the three component tissues must be complete. Due to limitations of the DXA physics, individual ray paths may be decomposed into only two components so projections using material decomposition are incomplete in regions where there are three discrete materials. In this chapter, we introduce an algorithm to generate three complete discrete projections to accommodate this situation. The algorithm was tested using projection simulations from segmented CT scans of different cross sections as well as simulations with simulated dual energy x-ray spectra.

5.1. Background

Since the DXA scanner produces X-rays at two different energy levels, only two materials can be decomposed in any given region. For rays passing through bone, the output can be decomposed into bone and soft tissue (an unknown mixture of lean tissue

and fat), and for rays passing through a bone-free area, fat and lean tissue can be decomposed. Therefore there are some missing portions in the fat and lean projections in the shadow of the bone, as shown in Fig. 5.1. This prevents complete tomographic reconstructions of those materials.

The challenge due to bone shadowing of the soft tissue is greater when there is a greater amount of bone, relative to soft tissue in the cross-section In our examples we can illustrate this in cross-sections of the lower leg with two bones. As shown in Fig. 5.2, large regions are missing from fat and lean projection curves compared to the known parts of them and this should increase the chance of error in estimating those missing curves. Also, depending on the projection angle there may be one missing region where bones overlap and two where they do not (Fig. 5.3). This complicates problem formulation in estimating the missing curves.

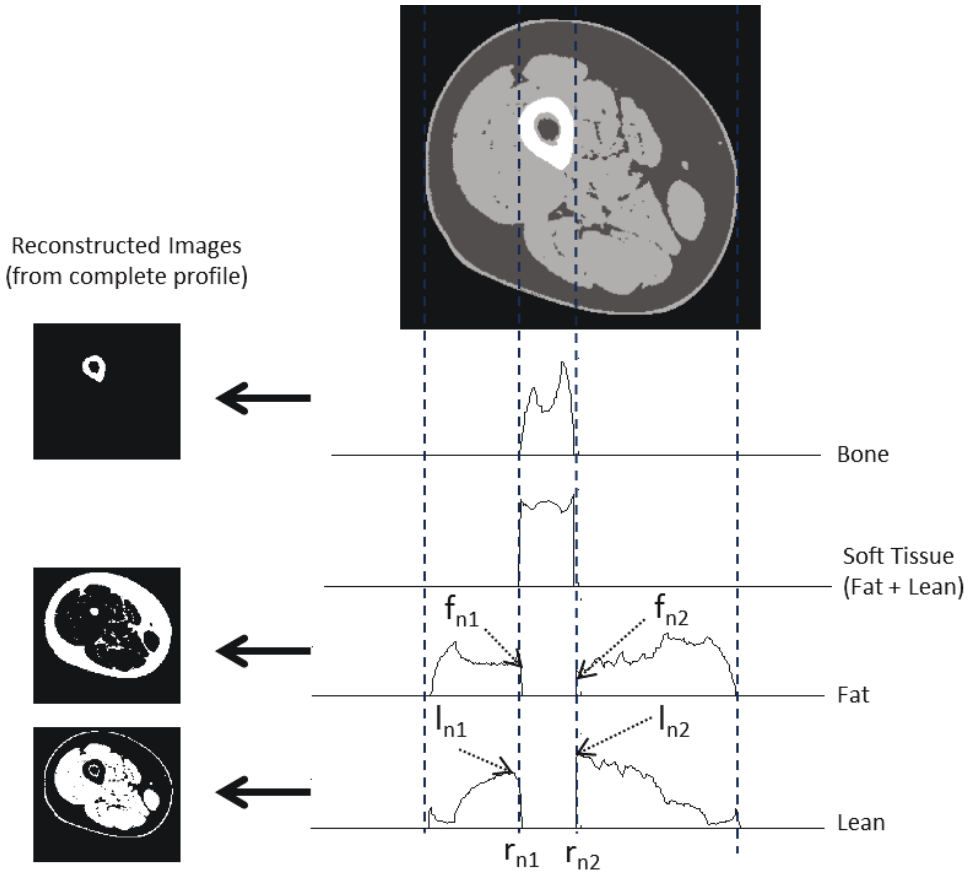

Fig. 5.1. Two-material decomposition in a DXA projection for a mid-femur cross section.

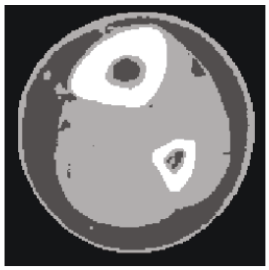

(a)

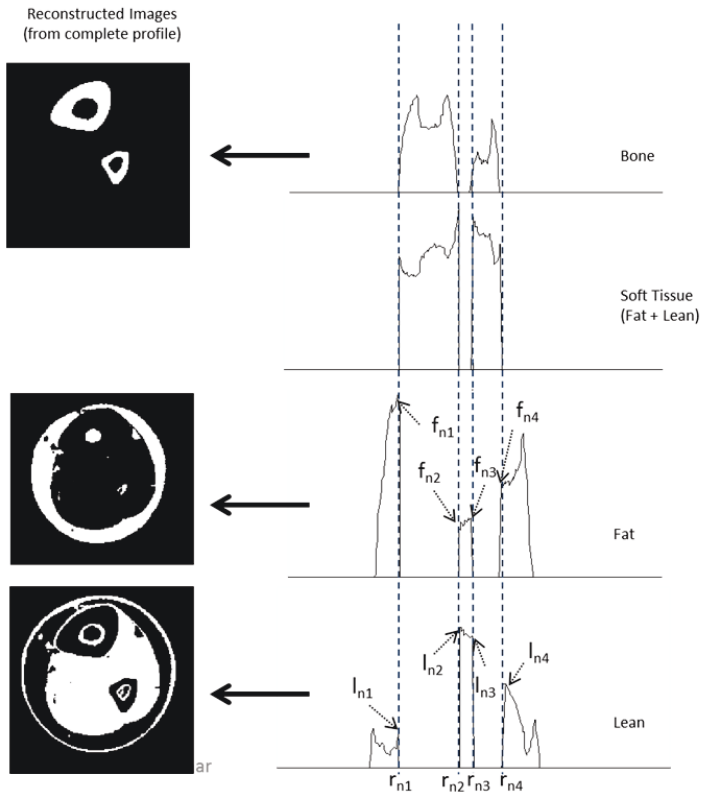

(b)

Fig. 5.2. Two-material decomposition in a representative DXA projection for a lower leg cross section. (a) segmented lower leg cross section. (b) individual projections

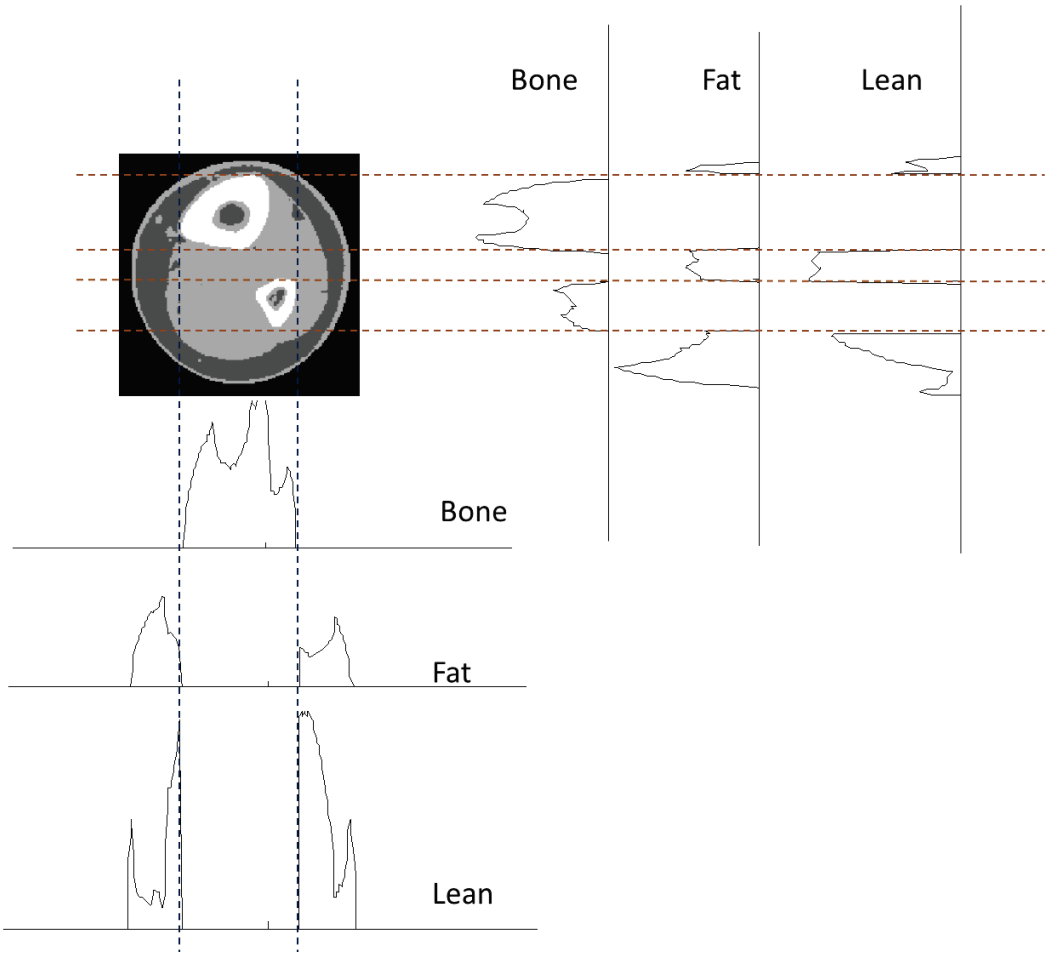

Fig. 5.3. 0° and 90° projections of a lower leg cross section.

In previous literature, different methods had been used to estimate the missing fat and lean regions under the bone. One method is to assume uniform distribution [15, 66], where the ratio of the fat to lean on both edges of the bone is calculated, averaged, and used in the area under the bone. This method is inaccurate because the soft tissue composition cannot be assumed to be the same everywhere. A somewhat more appropriate method is to use a weighted linear distribution method [66] or linear interpolation (LI). In this method, it is assumed that the fat percent in soft tissue changes

linearly from that measured at one bone edge to that measured at the other edge. This method has been considered sufficiently accurate for total body composition calculations but is inadequate for tomographic reconstruction. More accurate methods for approximations and estimation of these curves are usually proprietary.

In this chapter, we propose a new method for estimating the missing portions of the projections, the multi-projections material decomposition (MPMD) method. This method simultaneously uses data from all of the available projections to estimate the missing regions in each single projection. We hypothesize that this approach makes the estimation more accurate and hence improve limited angle tomographic reconstructions. The algorithm is demonstrated below using cross-sections through the mid-thigh and lower leg of an adult subject.

5.2. Methods

5.2.1. Problem Formulation

We formulated the problem as an optimization with two logical constraints. The first constraint is summation, where the fat and lean curves in the missing region of each projection must sum to equal the measured soft tissue curve (see Fig. 5.1). The second constraint is the area, where we assume that the areas under fat and lean curves are equal over all projections. Curves were modeled as sums of sinusoids with *n* harmonics and with coefficients arranged in *x*. The optimization problem can be expressed as:

$$min_x \sum_{i=1}^{P} \left\| f^i(r) + l^i(r) - s^i(r) \right\|^2 \; + \; \|Ax - b\|^2$$

$$where\ r_{n1} \leq r \leq r_{n2}$$

$$and\ i = 1,2, \ldots \ldots, P$$

$$where\ P\ is\ the\ number\ of\ projections \tag{5.1}$$

Where *f*, *l* and *s* are the fat, lean and soft tissue curves, respectively. r_{n1} and r_{n2} are the indices of the start and end points of the required curve (shown in Fig. 5.1). The area constraint is arranged in matrix *A* and vector *b*. This will be described in the next section. And,

$$\begin{aligned} f(r) = c + \ & a_1 \cos\left(\frac{2\pi r}{r_{n2} - r_{n1}}\right) + b_1 \sin\left(\frac{2\pi r}{r_{n2} - r_{n1}}\right) \\ & + a_2 \cos\left(\frac{4\pi r}{r_{n2} - r_{n1}}\right) + b_2 \sin\left(\frac{4\pi r}{r_{n2} - r_{n1}}\right) \\ & + \cdots\cdots\cdots \\ & + a_n \cos\left(\frac{2n\pi r}{r_{n2} - r_{n1}}\right) + b_n \sin\left(\frac{2n\pi r}{r_{n2} - r_{n1}}\right) \end{aligned} \tag{5.2}$$

$$\begin{aligned} l(r) = d + \ & e_1 \cos\left(\frac{2\pi r}{r_{n2} - r_{n1}}\right) + g_1 \sin\left(\frac{2\pi r}{r_{n2} - r_{n1}}\right) \\ & + e_2 \cos\left(\frac{4\pi r}{r_{n2} - r_{n1}}\right) + g_2 \sin\left(\frac{4\pi r}{r_{n2} - r_{n1}}\right) \\ & + \cdots\cdots\cdots \\ & + e_n \cos\left(\frac{2n\pi r}{r_{n2} - r_{n1}}\right) + g_n \sin\left(\frac{2n\pi r}{r_{n2} - r_{n1}}\right) \end{aligned} \tag{5.3}$$

The vector x contains the coefficients of $f(r)$ and $l(r)$ curves that need to be determined in the following order:

$$x = [c;\ a_1;\ b_1;\ a_2;\ b_2; \ldots\ldots\ldots; d;\ e_1; g_1; e_2; g_2; \ldots\ldots\ldots] \tag{5.4}$$

Since preliminary testing indicated that three harmonics are adequate three were used in all subsequent work.

To ensure continuity, the start and end points of curves in missing regions must be contiguous with boundary points in the available part of the curve for both fat and lean. To satisfy that constraint, we set the proper elements of the initial guess of the variable x (x_0), such that the start points of the missing curves will be equal to f^i_{n1}, and l^i_{n1} , where f^i_{n1}, and l^i_{n1} are the start points of fat and lean curves in projection i. This can be done by setting:

$$c^i = f^i{}_{n1} \quad and \quad d^i = l^i{}_{n1} \tag{5.5}$$

5.2.2. Area Constraint

The formula for the area constraint is different between cross sections with one bone and those with two bones. In case of one bone, only one curve region will be missing per tissue per projection. From Fig. 5.4(a), the area under the curve in a given projection can be expressed as:

$$f_{area} = A_1 + A_2 + \int_{r_{n1}}^{r_{n2}} f(r)dr \tag{5.6}$$

Let

$$A_T = A_1 + A_2 \tag{5.7}$$

Then,

$$f_{area} = A_T + \int_{r_{n1}}^{r_{n2}} f(r)dr \tag{5.8}$$

To satisfy the area constraint, the area under the curve of each material is assumed to be equal in all. Then,

$$f^1{}_{Area} = f^2{}_{Area} = \cdots = f^P{}_{Area} \tag{5.9}$$

Comparing two projections,

$$f^1{}_{Area} = f^2{}_{Area} \tag{5.10}$$

$$A_T{}^1 + \int_{r_{n1}}^{r_{n2}} f^1(r)dr = A_T{}^2 + \int_{r_{n1}}^{r_{n2}} f^2(r)dr \tag{5.11}$$

$$\int_{r_{n1}}^{r_{n2}} f^1(r)dr - \int_{r_{n1}}^{r_{n2}} f^2(r)dr = A_T{}^2 - A_T{}^1 \tag{5.12}$$

This process is repeated for the remaining projections; the left hand sides of Equation (5.12) and similar equations are arranged in matrix A while the right hand sides (which are numbers) are arranged in vector b. This is done for both fat and lean projections sets.

In case of cross sections with two bones, from Fig. 5.4(b), the area under the curve in a given projection can be expressed as:

$$f_{area} = A_1 + A_2 + A_3 + \int_{r_{n1}}^{r_{n2}} f(r)dr + \int_{r_{n3}}^{r_{n4}} f(r)dr \tag{5.13}$$

Let

$$A_T = A_1 + A_2 + A_3 \tag{5.14}$$

Then,

$$f_{area} = A_T + \int_{r_{n1}}^{r_{n2}} f(r)dr + + \int_{r_{n3}}^{r_{n4}} f(r)dr \tag{5.15}$$

To satisfy the area constraint:

$$f^1{}_{Area} = f^2{}_{Area} = \cdots = f^P{}_{Area} \tag{5.16}$$

Comparing two projections,

$$f^1{}_{Area} = f^2{}_{Area} \tag{5.17}$$

$$A_T{}^1 + \int_{r_{n1}}^{r_{n2}} f^1(r)dr + \int_{r_{n3}}^{r_{n4}} f^1(r)dr =$$

$$A_T{}^2 + \int_{r_{n1}}^{r_{n2}} f^2(r)dr + \int_{r_{n3}}^{r_{n4}} f^2(r)dr \tag{5.18}$$

$$\left[\int_{r_{n1}}^{r_{n2}} f^1(r)dr + \int_{r_{n3}}^{r_{n4}} f^1(r)dr\right] - \left[\int_{r_{n1}}^{r_{n2}} f^2(r)dr + \int_{r_{n3}}^{r_{n4}} f^2(r)dr\right]$$

$$= A_T{}^2 - A_T{}^1 \tag{5.19}$$

Similar to the case of cross sections with one bone, this process is repeated for remaining projections, with the left hand side of Equation (5.19) and arranged in matrix A and the right hand sides in vector b. Knowing that not all projections have the same number of unknown curve regions, equation (5.19) can have two, three, or four integration terms according to the projections being compared.

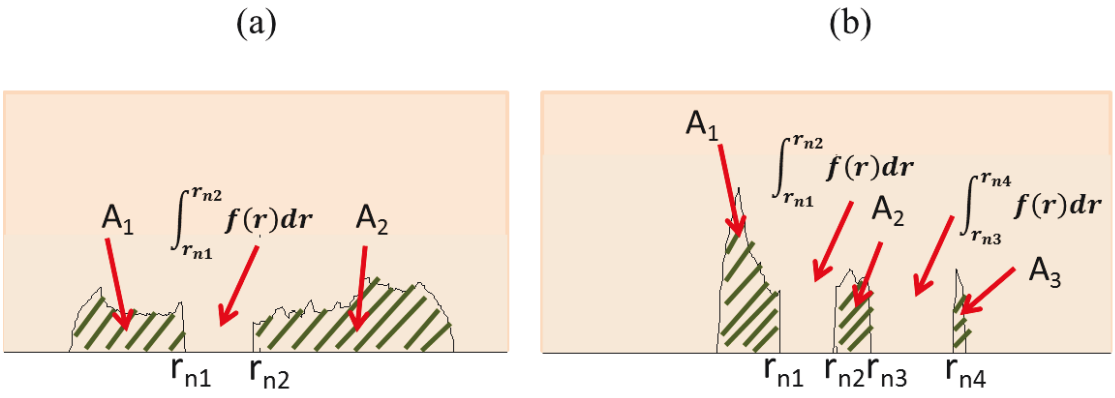

Fig. 5.4. Explanation of the area constraint in case the cross section contains (a) one bone, or (b) two bones.

5.3. Simulations

5.3.1. Simulations of Projections

Selected CT cross-sections were segmented into Bone, Fat, and Lean tissues using thresholding. The projections were then directly generated at selected angles for individual tissues as described previously in section 4.3.1. Fat and lean projections have missing regions under bone to be estimated using the proposed MPMD method.

In the second part of the simulations, dual energy x-ray methods were used in two forms to separately assess effects with and without beam hardening. First is the monoenergetic case where two x-ray beams at 41 kVp and 99 kVp were used. In the second, more realistic form using two tungsten target x-ray spectra was used. The low energy spectrum was generated at 70 kVp filtered with 0.8 mm Beryllium, 4 mm Aluminum, and 0.5 mm Copper; and the high energy at 140 kVp filtered with 4 mm Aluminum, and 3.1 mm Copper [67]. These spectra are shown in Fig. 5.5, where low and high energy spectra are shown in red and blue respectively.

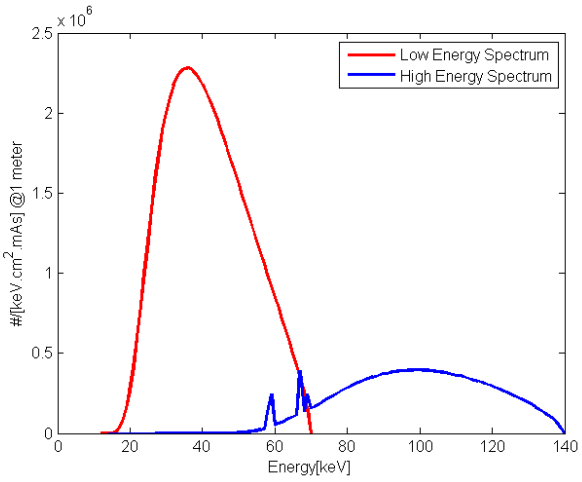

Fig. 5.5. Simulated X-ray spectra

These spectra were calibrated using basis material decomposition methods where a combination of bone-like and soft tissue-like basis materials usually aluminum and acrylic are used in the calibration process [68]. The low and high energy spectra are transmitted through blocks of aluminum and acrylic with different thicknesses (0, 1, 2, 4, 8, 16, 32 mm of Aluminum and 0, 10, 50, 100, 150, 200, 250 mm of Acrylic). The negative of log of intensity transmission for low and high energy beams $-\ln(I/I_0)$ is then calculated with each combination for both low and high energies and polynomials of the form shown in equations (5.20) and (5.21) are fitted to solve for the unknowns a_1 through a_6 and b_1 through b_6.

$$t_{AL} = a_1 {H_{LE}}^2 + a_2 {H_{HE}}^2 + a_3 H_{LE} H_{HE} + a_4 H_{LE} + a_5 H_{HE} + a_6 \tag{5.20}$$

$$t_{AC} = b_1 {H_{LE}}^2 + b_2 {H_{HE}}^2 + b_3 H_{LE} H_{HE} + b_4 H_{LE} + b_5 H_{HE} + b_6 \tag{5.21}$$

where t_{AL} and t_{AC} are the aluminum and acrylic thicknesses corresponding to

$$H_{LE} = -\ln\left(I/I_0\right)_{LE} \tag{5.22}$$

and

$$H_{HE} = -\ln\left(I/I_0\right)_{HE} \tag{5.23}$$

where I is the output intensity and I_0 is the intensity of the incident beam in cases of low energy (LE) and high energy (HE).

These low and high x-rays can then pass through the segmented cross sections with bone, fat and lean tissues. The following equation was used to calculate the output intensity [61]:

$$I(x) = \sum_E S_0(E') E' e^{-\sum_0^x \mu(x';E')\Delta x'} \tag{5.24}$$

where

$S_0(E')$ is the incident x-ray spectrum at energy E'

$\mu(x';E')$ is the linear attenuation coefficient of a material x' at specific energy E'

$\Delta x'$ is the material thickness

The densities of the materials and tissues assumed in the calculations are listed in Table 5.1 [69]. In case of soft tissue, the density of lean tissue is assumed.

An example of the simulated projection output for a 0° projection is shown in Fig. 5.6. Next step is to map H_{LE} and H_{HE} to equivalent thicknesses of aluminum and acrylic using equations (5.20) and (5.21). An example of the mapped aluminum and acrylic projections is shown in Fig. 5.7.

Aluminum and acrylic projections are then be used to calculate bone, fat and lean projections. It is obvious that the region including bone can be separated with a simple edge detection method. In this case, we can decompose the area under the bone to bone and soft tissue and the bone-free area to fat and lean. However, equations used in the literature [70, 71] have energy range limitations and differ from one paper to another, so we decided to derive our equations (5.25) to (5.32). Derivations of these equations are shown in the next section.

Table 5.1. Densities in gm/cm^3 of different materials used in simulations

Material /Tissue	**Density (g/cm^3)**
Aluminum	2.7
Acrylic	1.19
Bone	1.92
Fat	0.95
Lean	1.05

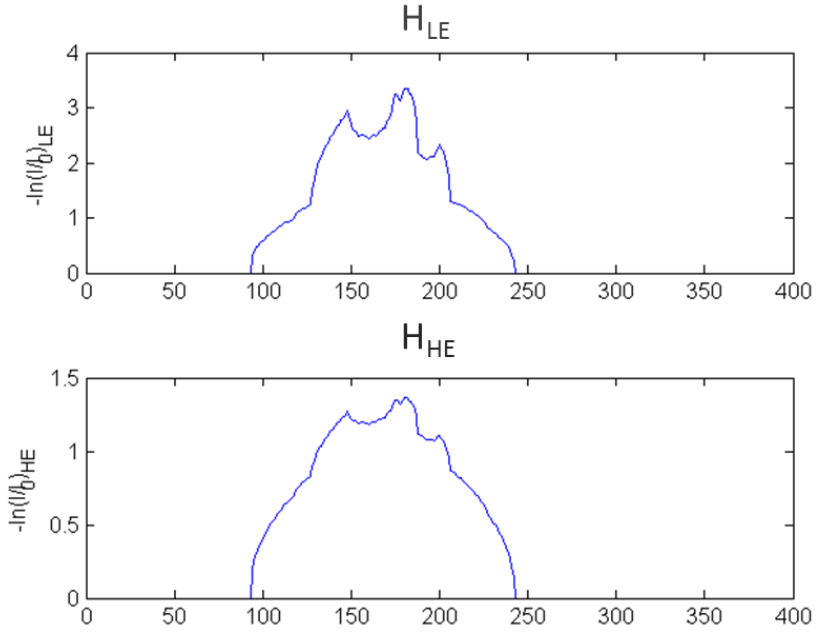

Fig. 5.6. H_{LE} and H_{HE} of 0° projection of a lower leg cross section

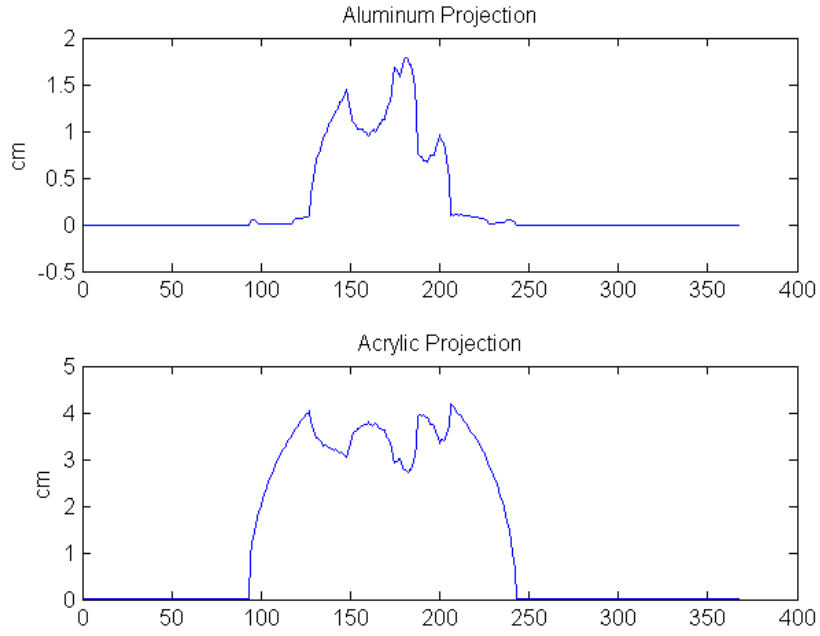

Fig. 5.7. Decomposed aluminum and acrylic 0° projection of a lower leg cross section

In monoenergetic case, the area under bone is decomposed into bone and soft tissue using the following equations:

$$t_B = 1.1325\, t_{AL} - 0.0436\, t_{AC} \tag{5.25}$$

$$t_{ST} = 0.3114\, t_{AL} + 1.1858\, t_{AC} \tag{5.26}$$

where t_B, t_{ST}, $t_{AL}$and t_{AC} are the bone, soft tissue, aluminum and acrylic thicknesses at each point of the projection curve, respectively. While the bone-free area is decomposed into fat and lean tissue using the following equations:

$$t_F = -29.1148\, t_{AL} + 1.1458\, t_{AC} \tag{5.27}$$

$$t_L = 28.8339\, t_{AL} + 0.0666\, t_{AC} \tag{5.28}$$

where t_F and t_L are the fat and lean tissue thicknesses at each point of the projection curve, respectively.

In case of realistic spectra, the following equations are used instead:

$$t_B = 1.1296\, t_{AL} - 0.044\, t_{AC} \tag{5.29}$$

$$t_{ST} = 0.3213\, t_{AL} + 1.1871\, t_{AC} \tag{5.30}$$

$$t_F = -26.8729\, t_{AL} + 1.0831 t_{AC} \tag{5.31}$$

$$t_L = 27.0144\, t_{AL} + 0.1199\, t_{AC} \tag{5.32}$$

Generation of the bone projection is complete after this step while fat and lean projections are not; due to the unknown mixtures under the bone that are estimated using the proposed MPMD algorithm.

5.3.2. Simulations to derive the relationship between different tissues and basis materials

In this section, we present the simulations used to derive the relationship between each tissue type i.e. bone, fat and lean and basis materials used in DXA calibration such as Aluminum and Acrylic.

5.3.2.1. Bone-Lean Decomposition

The low and high DXA energy spectra are transmitted through blocks of aluminum and acrylic with different thicknesses (0, 1, 2, 4, 8, 16, 32 mm of Aluminum and 0, 10, 20, 40, 80, 160, 320 mm of Acrylic). All combinations are used and the low and high output intensity I_L and I_H are calculated, then $H_{LE} = -\ln\left(I/I_0\right)_{LE}$ and $H_{HE} = -\ln\left(I/I_0\right)_{HE}$ are calculated. Aluminum and Acrylic combinations along with the corresponding H_{LE} and H_{HE} are arranged to form Aluminum-Acrylic (AL-AC) data table.

The same procedure is repeated with different thicknesses of bone and lean tissue. For bone the range from 0 to 10 cm with 0.1 cm increment is used, while for lean tissue, the range is 0 to 45 cm with 0.5 cm increment. All combinations are used and H_{LE} and H_{HE} are calculated. Similarly, we form the Bone-Lean (BL) data table.

Minimum distance classifier then used to assign H_{LE} and H_{HE} from BL table to the nearest H_{LE} and H_{HE} from AL-AC table to form a match points as shown in Fig. 5.8. Threshold of 0.05 is used such as: if the minimum distance is more than 0.05, we cannot use these pair points as match. The following equation is used to measure the distance and optimize for the nearest point.

$$(H_{LE}, H_{HE})_{AL-AC} =$$

$$\arg min_{(H_{LE},H_{HE})^{i}{}_{AL-AC}} \left\| (H_{LE}, H_{HE})_{BM} - (H_{LE}, H_{HE})^{i}{}_{AL-AC} \right\| \tag{5.33}$$

Matching pairs of Aluminum-Acrylic and Bone-Lean are shown in Fig 5.9. These pairs are then checked for unreasonable values. For example, if bone has thickness more than 0 while aluminum has thickness of 0 and vice versa. The same also applies for the lean tissue and acrylic relationship.

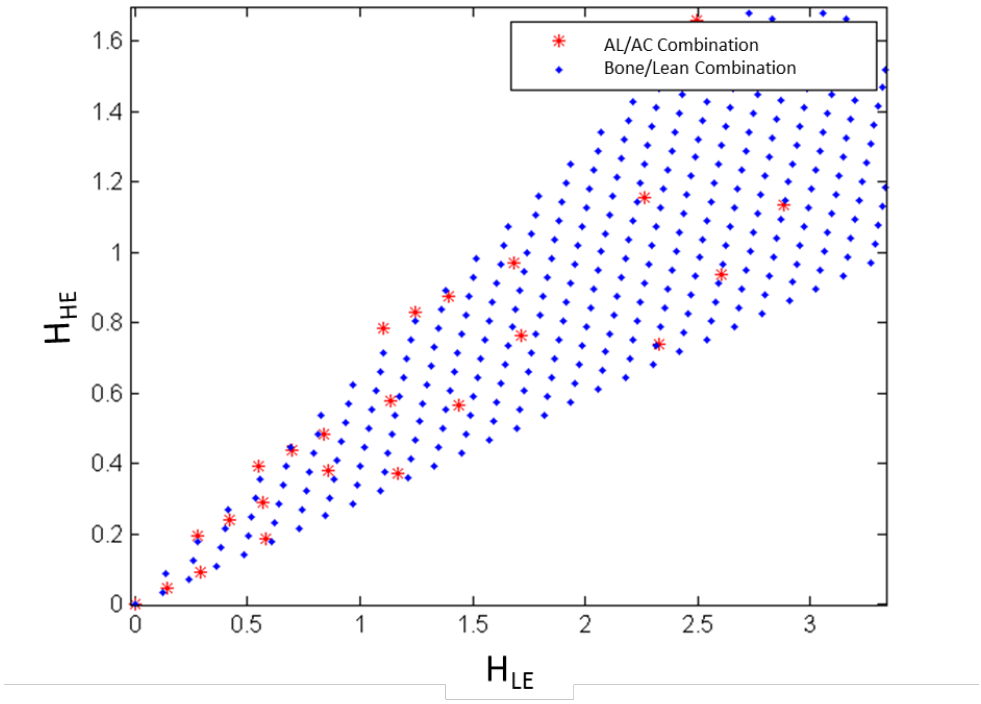

Fig. 5.8. Every point from BL table (blue) is matched with the nearest point from AL-AC table (red) with the threshold of 0.05. (only portion of the original data range is displayed).

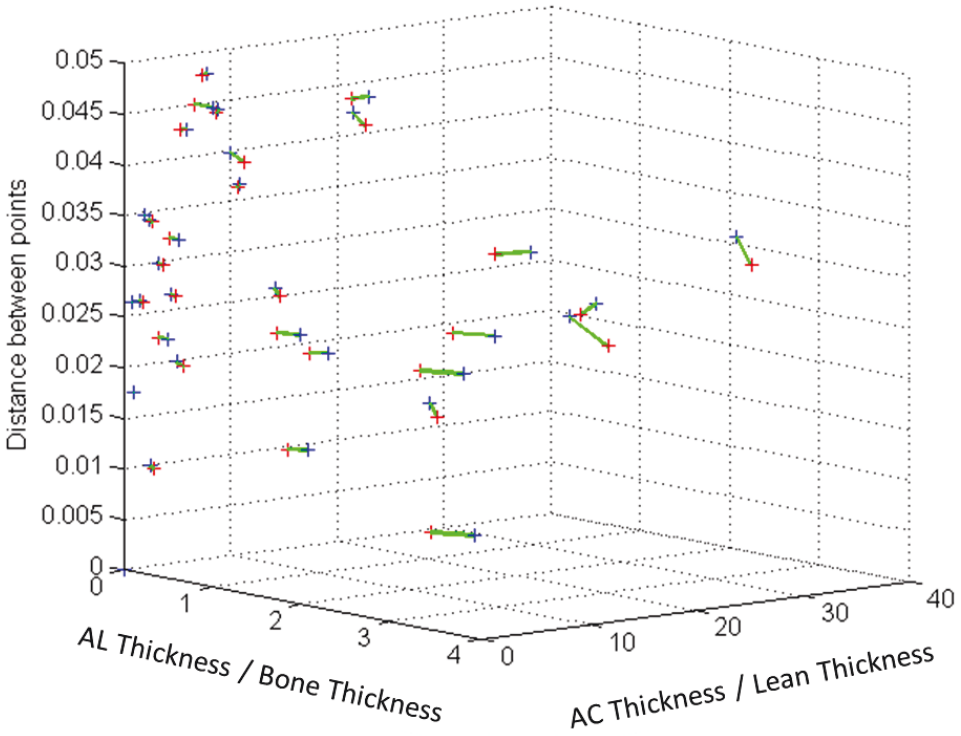

Fig. 5.9. Matching pairs of Aluminum-Acrylic and Bone-Lean

The linear regression is then used to model the relationship between bone as a dependent variable and aluminum and acrylic as independent variables. The same applies for lean tissue. Results are shown in Fig. 5.10 and interpreted in the following equations:

$$t_B = 1.1325\, t_{AL} - 0.0436\, t_{AC} \tag{5.34}$$

$$t_{ST} = 0.3114\, t_{AL} + 1.1858\, t_{AC} \tag{5.35}$$

where t_B, t_{ST}, $t_{AL}$and t_{AC} are the bone, soft tissue, aluminum and acrylic thicknesses at each point of the projection curve, respectively. Here lean tissue is used instead of soft tissue since they do not differ significantly in the material properties.

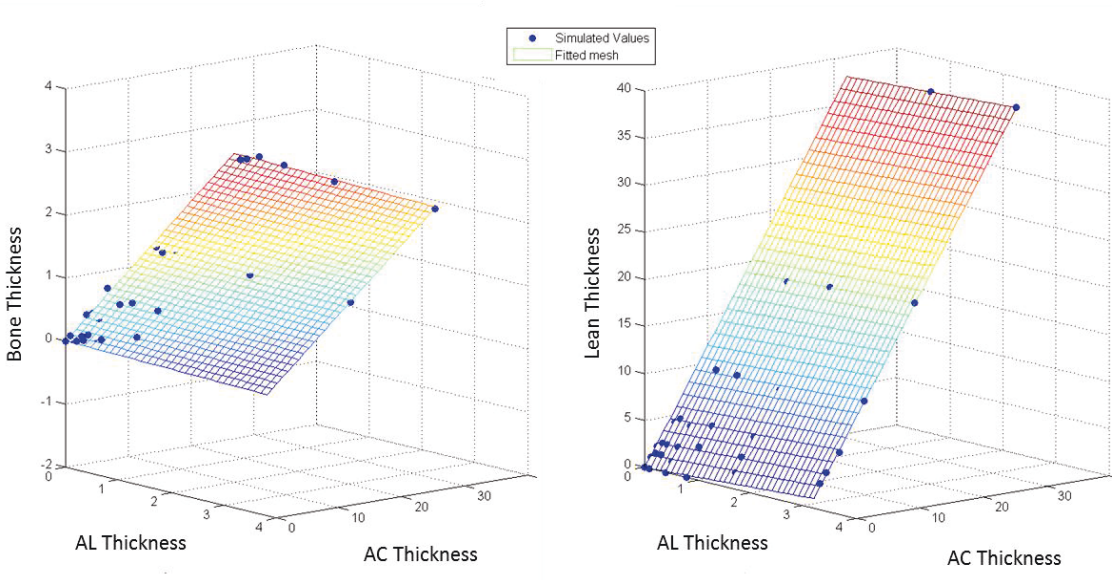

Fig. 5.10. Results of the linear regression for bone and lean tissue

Equations (5.34) and (5.35) are derived using monochromatic DXA beams. In case of spectrum, the following equations should be used instead:

$$t_B = 1.1296\, t_{AL} - 0.044\, t_{AC} \tag{5.36}$$

$$t_{ST} = 0.3213\, t_{AL} + 1.1871\, t_{AC} \tag{5.37}$$

5.3.2.2. Fat-Lean Decomposition

To derive the relationship between fat and lean tissue and basis materials, different thicknesses of fat and lean tissue are used. For both of them, the range is 0 to 45 cm with 0.5 cm increment is used. All combinations are employed and H_{LE} and H_{HE} are calculated. We then form the Fat-Lean (FL) data table that contains different thicknesses of fat and lean tissue and the corresponding H_{LE} and H_{HE} values.

Similarly and using the AL-AC table generated in the last section, the minimum distance between each point from FL table and AL-AC table is computed in order to find a matching pairs. Then the linear regression is applied. The results are shown in Fig. 5.11 and equations (5.38) and (5.39) in case of monochromatic DXA and in equations (5.40) and (5.41) in case of spectrum.

$$t_F = -29.1148\, t_{AL} + 1.1458\, t_{AC} \tag{5.38}$$

$$t_L = 28.8339\, t_{AL} + 0.0666\, t_{AC} \tag{5.39}$$

and

$$t_F = -26.8729\, t_{AL} + 1.0831 t_{AC} \tag{5.40}$$

$$t_L = 27.0144\, t_{AL} + 0.1199\, t_{AC} \tag{5.41}$$

where t_F and t_L are the fat and lean tissue thicknesses at each point of the projection curve, respectively.

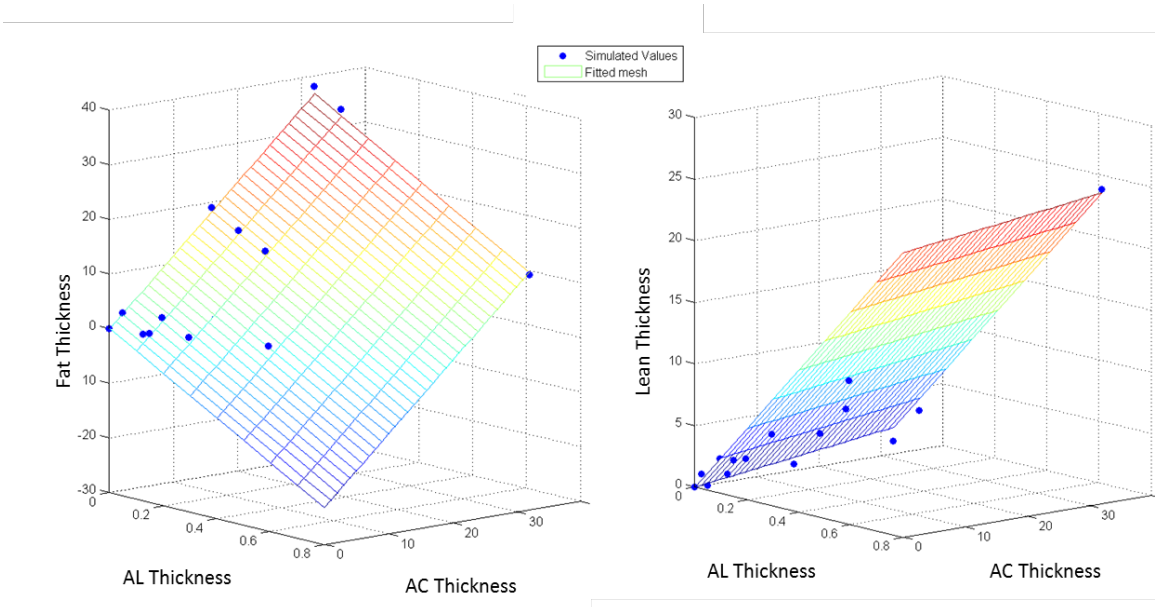

Fig. 5.11 Results of the linear regression for fat and lean tissue

5.3.3. Optimization Method

The Sequential Quadratic Programming (SQP) method was used for optimization. SQP method is considered the most efficient method to solve nonlinear optimization problems with constraints [72]. SQP method uses Newton‘s method to solve the KKT (Karush–Kuhn–Tucker) conditions of a given problem [73]. This transforms the original problem into a sequence of sub-problems. Each sub-problem is by turn minimizes a quadratic approximation of the LaGrangian function over a linear approximations of the constraints.

5.3.4. Image Reconstruction

Different numbers of equally-spaced projections (5, 7, 9, 11 and 13) between 0° to 90° were created. Reconstruction employed the successive binary algebraic reconstruction technique (SBART) algorithm (see chapter 4 for details).

5.3.5. Quality Indices

Two quality indices were used to judge the three-material decomposition results, area error and curve error. Area error can be calculated as:

$$\varepsilon_A = abs\left(\frac{\widehat{A_f} - A_f}{A_f}\right) \times 100 \tag{5.44}$$

where A_f and $\widehat{A_f}$ are the areas of under original and estimated curves. While the curve error can be calculated as:

$$\varepsilon_C = \sqrt{\frac{\sum_{i=1}^{n}\left(\frac{\widehat{f_i} - f_i}{f_i}\right)^2}{n}} \tag{5.45}$$

where ε_C is the RMSE of average error at each point of the curve, n is the number of points in the curve, f and $\hat{f}$ are the original and the estimated curves.

Finally, pixel error and other geometrical measurements such as area, center of mass, and second moment of area over the entire image are used to judge reconstruction results as described in Chapter 4.

5.4. Results

Fig. 5.12 shows the three-material decomposition results on one projection. The estimated projection using MPMD method (red) is shown against the known projection (blue) and one calculated using the linear interpolation (black). The missing region is magnified for clarity in (b). While not perfect, the MPMD projection is closer to the original projection than the linear interpolation, moreover the soft tissue curve is fully preserved in this case.

Fig. 5.13 shows the quality indices calculated from the MPMD (solid lines) and linear interpolation (dashed lines) projections of the mid-femur cross section. Area error is shown in (a), curve error of the fat and lean in (b), and soft tissue curve error in (c). In each graph, three cases are presented: CT simulations case where the original projections are used and the under-bone missing curves are estimated, monoenergetic and spectrum DXA simulations cases where the projections are simulated using dual-energy X-rays, then material decomposition and calibration process were used.

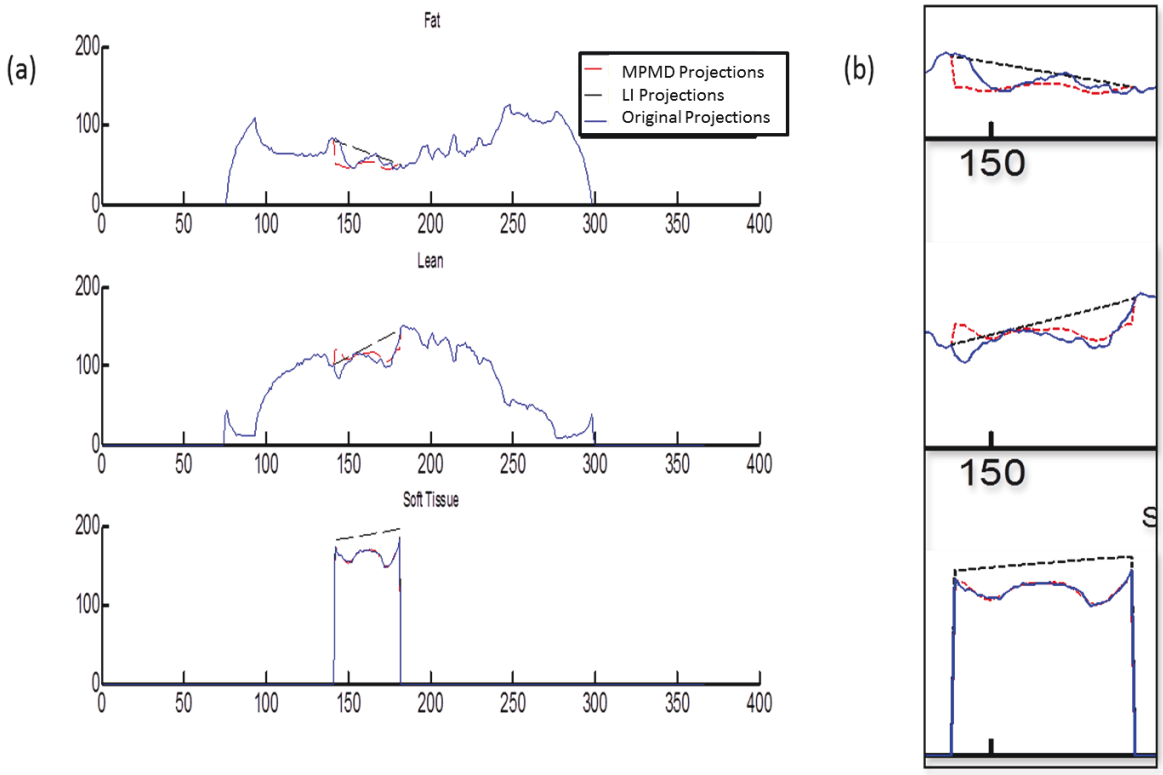

Fig. 5.12. MPMD curves (red) are shown against the original (blue) and linear interpolation curves (black). Whole curves are shown in (a), a magnified version of the results is shown in (b).

Generally, the figure shows the enhancement of the MPMD projections over those calculated using linear interpolation. There is a significant difference in area error and curve error between both types of projections regardless of the method used for simulations ($p<0.0001$ and $p<0.05$ respectively). Using CT simulations, the area error (Fig. 5.13 (a)) of the MPMD projections ranges from 1.2% to 1.6 % vs. 2.7% to 2.8% in case of projections calculated using linear interpolation. The error increases to the range of 2.2% to 2.7% in MPMD projections vs. 3% to 3.3% in linear interpolation of monoenergetic DXA. Error increases again to 3% - 3.6% vs. 3.4% - 3.9% if realistic

DXA spectra are used. Interestingly the area error changes little with 7 or more projections. The curve error shown in Fig. 5.13 (b) is also less with MPMD projections vs. linear interpolation ranging from 2.6% - 3.5% vs. 3.7% - 4.3% respectively. Soft tissue curve error (Fig. 5.13 (c)) is also low, maximum of 3%, in case of using MPMD compared to linear projection case. These results are encouraging.

The quality indices calculated for MPMD and linear interpolation projections of the lower leg cross section are shown in Fig. 5.14. The area error of the MPMD projections is less than projections with linear interpolation for CT simulations or monoenergetic DXA simulations are used, 2.5% - 7.4% vs. 11.6% - 12.9%. However if realistic DXA spectra are used, the errors are somewhat greater and comparable to that of linear interpolation 20.5% - 21.2% vs. 18.6% - 20.3% respectively. On the other hand, the curve error of the projections using linear interpolation is actually less than that of MPMD projections in all cases as shown in Fig. 5.14 (b). The differences in area error are significant ($p<0.01$) in all cases while differences in curve error are not significant with 5% significance level. Soft tissue curve error, shown in (c), is still a lot better in case of MPMD projections with maximum error of 3.6% vs. minimum of 7.1% in case of linear interpolation.

(a)

(b)

(c)

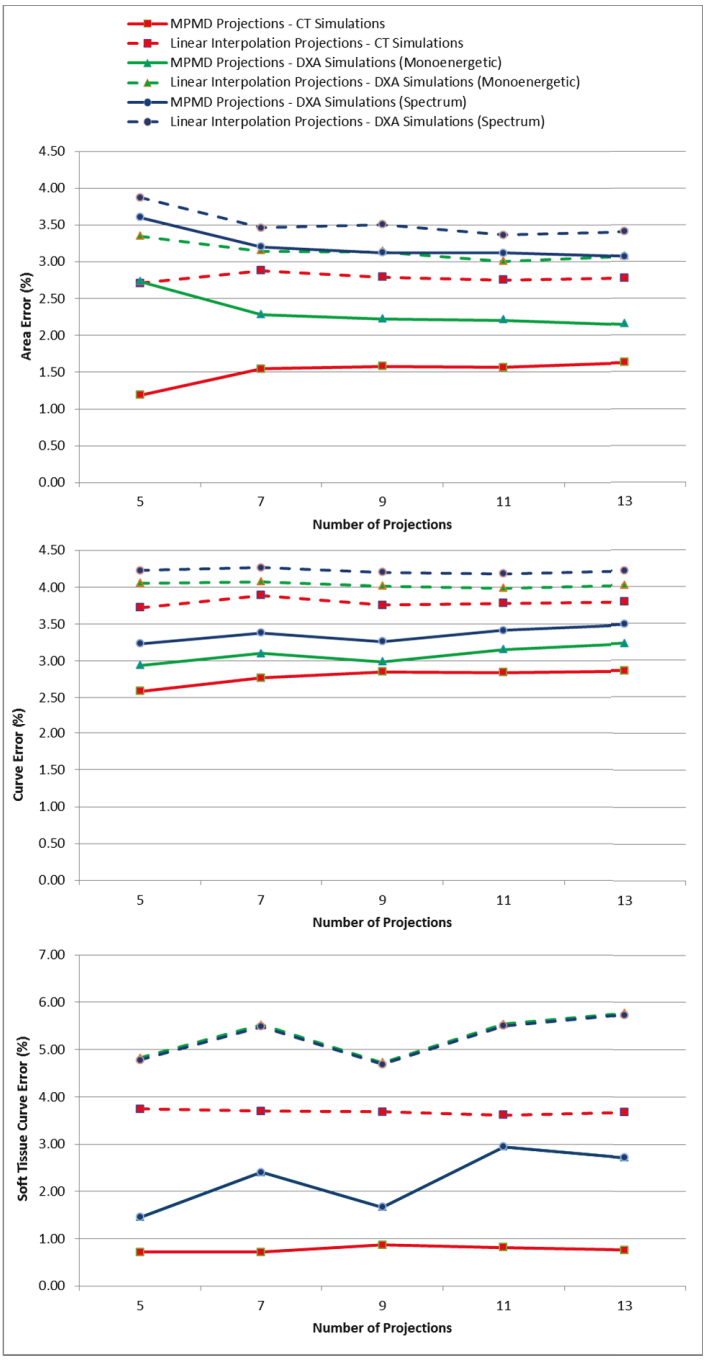

Fig. 5.13. Quality indices calculated from the MPMD (solid lines) and linear interpolation (dashed lines) projections in case of using CT simulations (red), monoenergetic (green) and spectrum (blue) DXA simulations of the mid-femur cross section. (a) Mean area error (fat and lean) over all projections. (b) Mean curve error (fat and lean) over all projections. (c) Mean curve error of soft tissue over all projections.

(a)

(b)

(c)

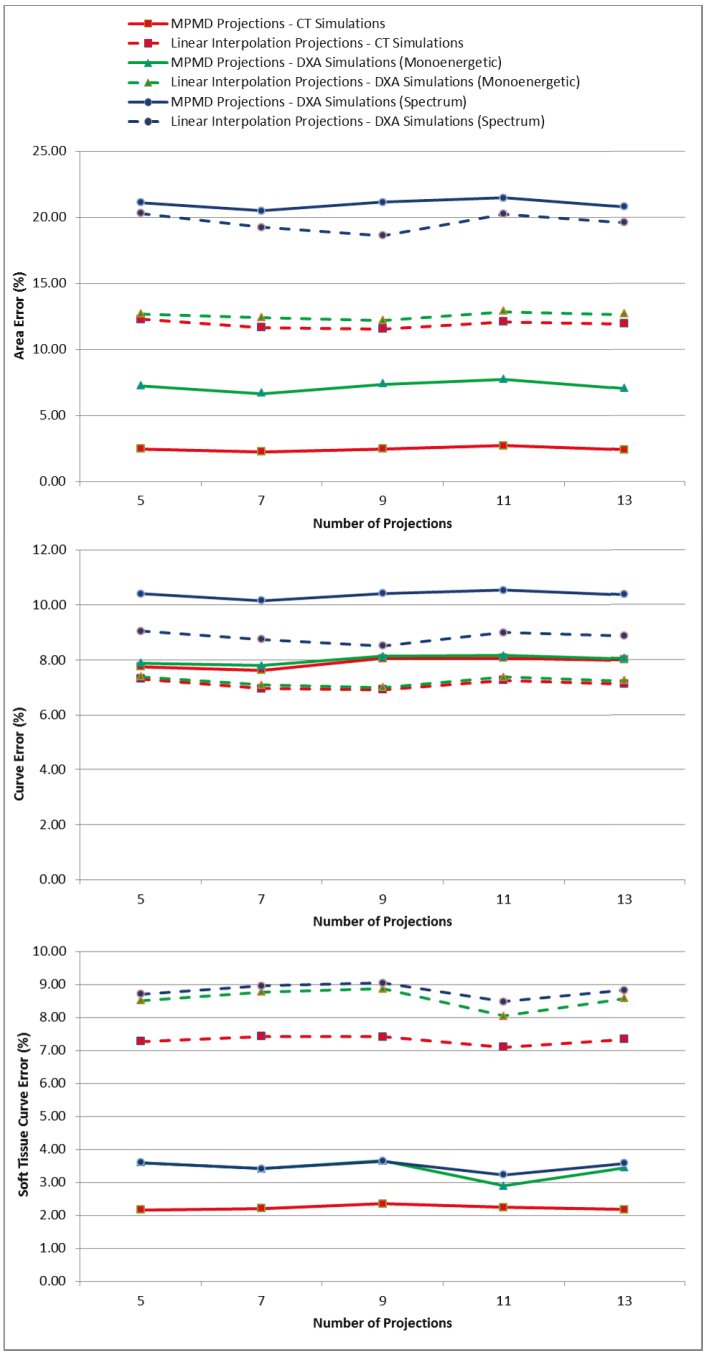

Fig. 5.14. Quality indices calculated from the MPMD (solid lines) and linear interpolation (dashed lines) projections in case of using CT simulations (red), monoenergetic (green) and spectrum (blue) DXA simulations of the lower leg cross section. (a) Mean area error (fat and lean) over all projections. (b) Mean curve error (fat and lean) over all projections. (c) Mean curve error of soft tissue over all projections.

The reconstruction of mid-femur cross sections using the MPMD projections and the projections calculated from linear interpolation are compared in Fig. 5.15, 5.16 and 5.17 to those reconstructed from the original projections. Note that this process only improves the accuracy of the fat and lean tissue projections; the bone is already accurately separated by the material decomposition. Generally, the quality of the images improves with more projections used. However, the quality of the images reconstructed from projections that used CT simulations is better than those used monoenergetic DXA simulations, which is in turn better than projections used realistic DXA spectra. It is also clear that the quality of the images reconstructed from MPMD projections is superior to linear interpolation (LI) projections. Note that the lean tissue images using LI projections did not converge using the DART algorithm after the initial five ART iterations while the MPMD projection data did converge.

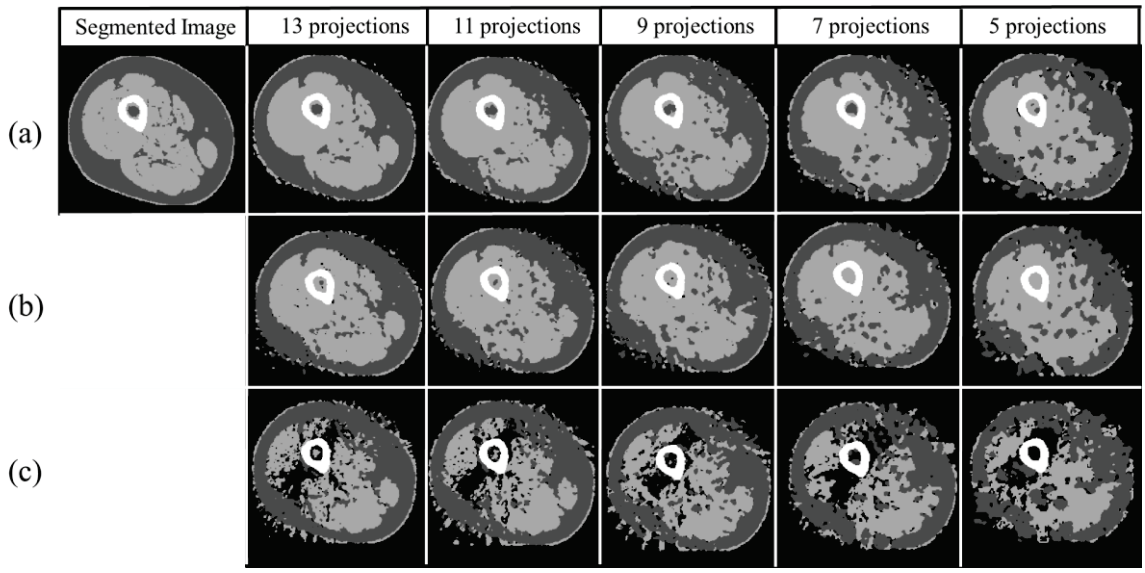

Fig. 5.15. Reconstructed mid-femur images using SBART algorithm from (a) original, (b) MPMD, and (c) linear interpolation projections in case of using CT simulations.

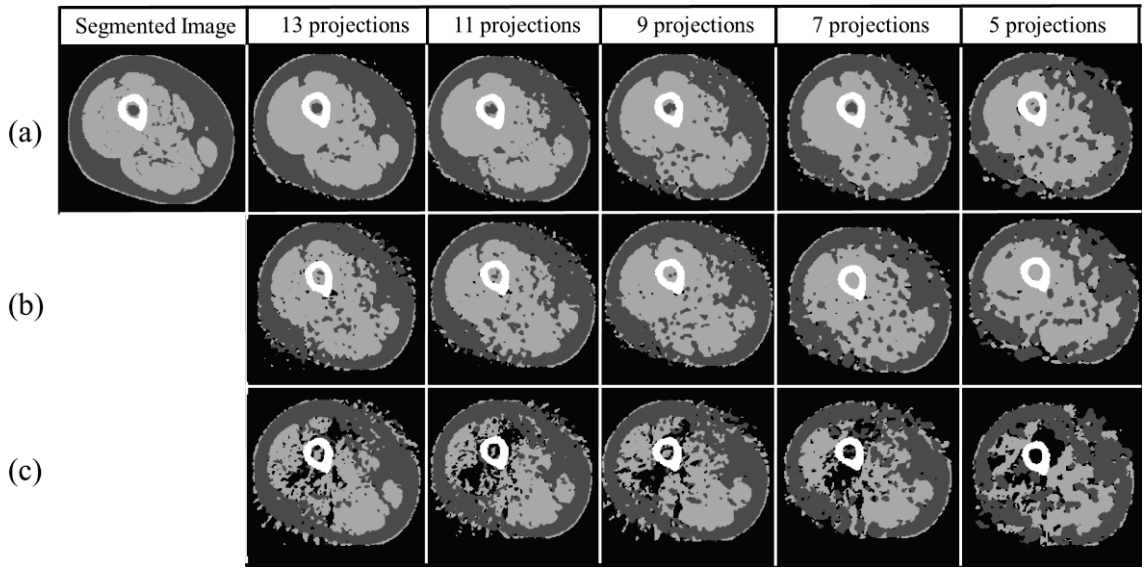

Fig. 5.16. Reconstructed mid-femur images using SBART algorithm from (a) original, (b) MPMD, and (c) linear interpolation projections in case of using monoenergetic DXA simulations.

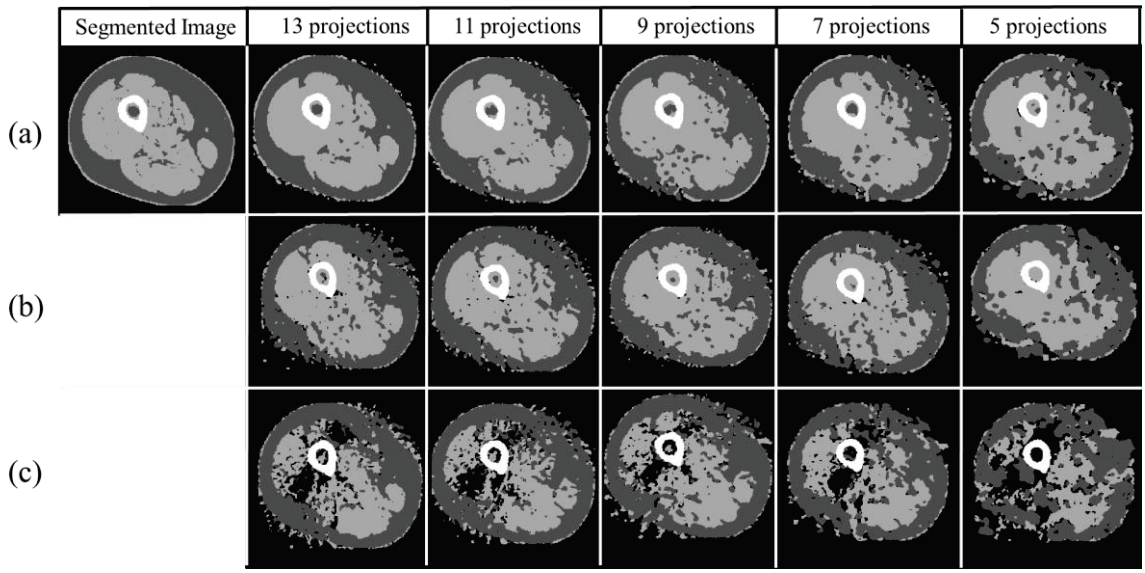

Fig. 5.17. Reconstructed mid-femur images using SBART algorithm from (a) original, (b) MPMD, and (c) linear interpolation projections in case of using spectrum DXA simulations.

Pixel, area and second moment of area errors for reconstructed mid-femur images shown in Fig. 5.18 (a)-(c) respectively are consistent with the obviously better image quality results. Pixel error of images reconstructed from MPMD projections in case of CT simulations starts at 21.5% if only 5 projections are used and decreases to 11.2% if 13 projections are used. While the images reconstructed form LI projections in the same case have pixel error ranges from 37.4% in case of 5 projections to 24.3 % in case of 13. Using monoenergetic DXA simulations, the pixel error of the images reconstructed from MPMD projections range is 24.2% (5 projections) to 15.2% (13 projections) vs. 38.8% to 23.1 % in case of LI projections. Similarly, in case of DXA spectrum, pixel error ranges from 23.9% to 17% in case of MPMD projections vs. 48.3% to 26.1% in case of LI projections. These values to be compared with the pixel error of the images reconstructed

form the original projections as a reference, which begins with 20.3% using 5 projections and decreases to only 5.5% if 13 projections are used.

Percentage error in area (ε_A) is less than 1.6% if MPMD projections are used regardless of the method used in the simulations of the projections, whether it is CT or DXA, while it is higher than 5.4% in case of LI projections with the highest value at 15.4% if only 5 projections are used and were simulated using DXA spectrum. The average error in the center of mass (ε_{CM}) is 0.22±0.12 mm and 4.93±1.18 mm in the two cases, with maximum of 0.44 mm in case of MPMD projections and 8.19 mm in case of LI.

Finally, the maximum absolute percentage error in second moment of area (ε_I) for the reconstructed images (Fig. 5.18 (c)) shows enhancement of the MPMD case over the LI case. The range of the error is 3.3% to 6.2% in case of MPMD projections vs. 7.7% to 21.9% in case of LI projections.

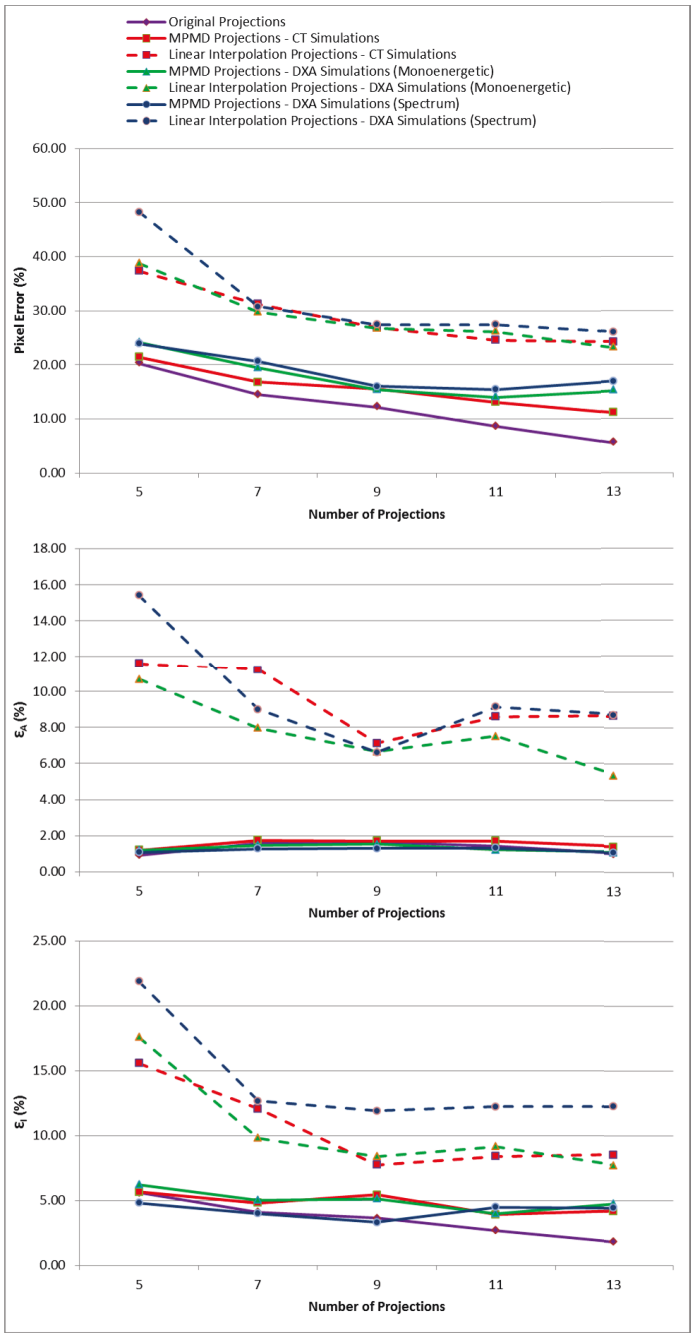

Fig. 5.18. Errors in the reconstructed mid-femur images using SBART algorithm from the MPMD (solid lines) and linear interpolation (dashed lines) projections in case of using CT simulations (red), monoenergetic (green) and realistic spectra (blue) DXA simulations. (a) Pixel error. (b) Percentage error in area. (c) Maximum absolute percentage error in the second moment of area.

Figures 5.19 to 5.21 show the reconstructed lower leg images. In this case, all lean images either using MPMD or LI projections did not converge after the initial ART iterations. This explains the low quality images and lack of obvious differences between images. Pixel error and other geometrical measurements are very important in this case to be able to judge the images numerically.

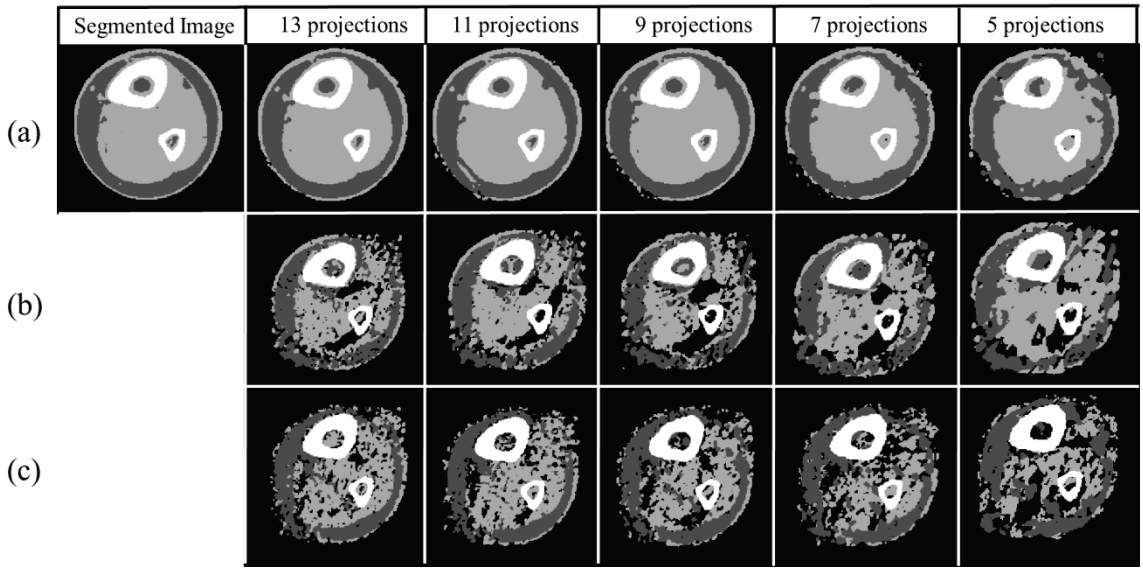

Fig. 5.19. Reconstructed lower leg images using SBART algorithm from (a) original, (b) MPMD, and (c) linear interpolation projections in case of using CT simulations.

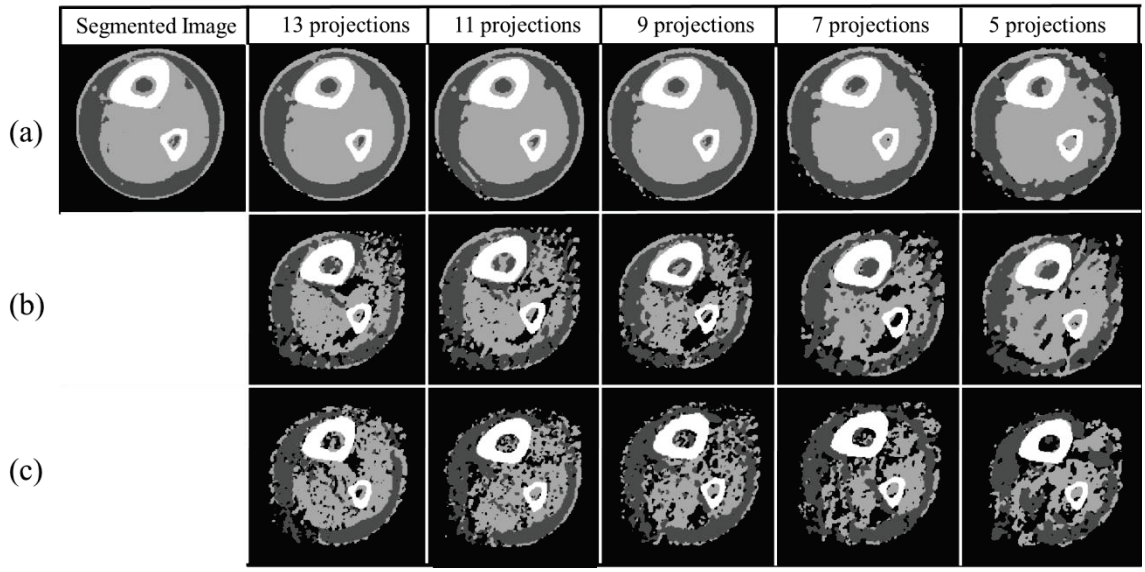

Fig. 5.20. Reconstructed lower leg images using SBART algorithm from (a) original, (b) MPMD, and (c) linear interpolation projections in case of using monoenergetic DXA simulations.

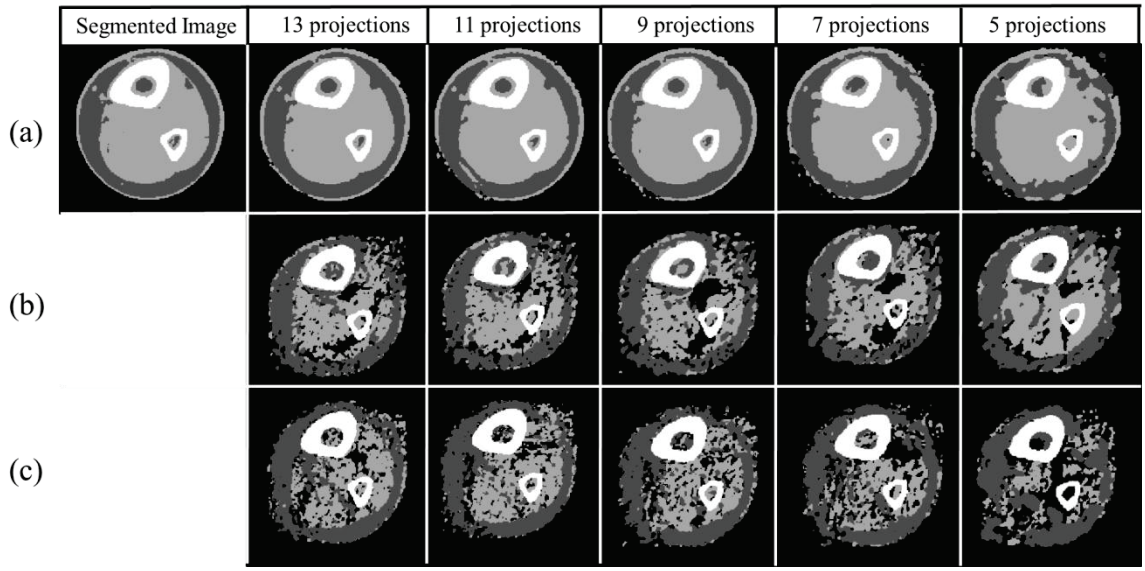

Fig. 5.21. Reconstructed lower leg images using SBART algorithm from (a) original, (b) MPMD, and (c) linear interpolation projections in case of using realistic spectra DXA simulations.

The quality indices of the reconstructed lower leg images are shown in Fig. 5.22 with pixel error in (a), percentage error in area in (b) and maximum absolute error in second moment of area in (c). Pixel error has the same pattern in all three cases of simulations, images reconstructed from MPMD projections are better if five or seven projections are used, images reconstructed using LI projections are slightly better if 9 projections are used, with almost no difference with 11 and 13 projections. All errors are quite large 30.3% - 54.4% compared to 3.3% - 14.5% if original projections are used in reconstruction.

Images reconstructed from MPMD projections have less error in area as shown in Fig. 5.22 (b). The range of errors is 2% to 14.9% in case of MPMD vs. 9.8% to 18.2% in case of LI. The average error in center of mass is 2.1±0.92 mm and 2.34±0.81 mm in the two cases respectively and reaches a maximum value of 3.9 mm in case of MPMD and 3.4 mm in LI case.

Considering the second moment of area, generally images reconstructed from MPMD projections are still better than those reconstructed from LI projections. The error ranges from 6.2% to 10% vs. 17.5% to 22.6% if CT simulations are used, 5.8% to 7.4% vs. 11% to 24.6% if monoenergetic DXA are used, and 10.2% to 12.9% vs. 20.6% to 25.4% if DXA spectrum is used.

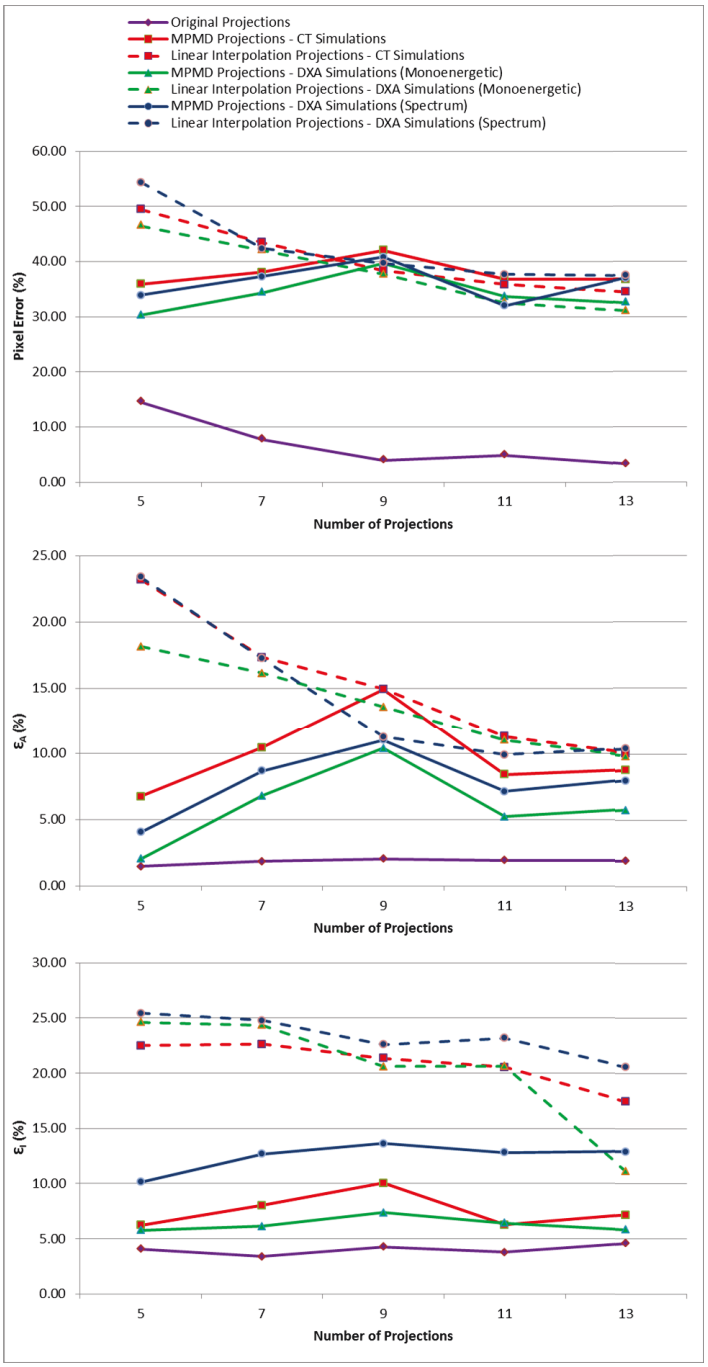

Fig. 5.22. Errors in the reconstructed lower leg images using SBART algorithm from the MPMD (solid lines) and linear interpolation (dashed lines) projections in case of using CT simulations (red), monoenergetic (green) and spectrum (blue) DXA simulations. (a) Pixel error. (b) Percentage error in area. (c) Maximum absolute percentage error in the second moment of area.

5.5. Discussion

Using the SBART algorithm, we are able to perform tomographic reconstruction from a small number of projections, which can provide a considerable reduction in patient dose in cases where it is adequate to image using only a small number of gray levels. To do so, the individual projections of component tissue types are needed. However, these projections are not complete due to the physics of the DXA and the limitation that only two materials can be decomposed at a time. Our proposed algorithm, multi-projection material decomposition (MPMD), uses all the available projections to perform three-material decomposition and generates the complete set of individual projections needed for the reconstruction. MPMD algorithm yielded far better results than the linear interpolation method in terms of material decomposition and reconstruction image quality.

The power of this algorithm is that it preserves area and the soft tissue composition. The area under the curve in all projections is constrained to be constant; this preserves the total area of that tissue in the reconstructed cross section. Also, since the algorithm has small soft tissue curve error (<3.6%), the summation constraint is satisfied to a great extent.

Nevertheless, it is apparent that DXA simulations especially with realistic spectra, decrease the quality of the reconstructed image. Employing the geometrically-constrained SBART (GC-SBART) algorithm should further enhance the results to some extent, especially the geometrical features of the images such as the center of mass and the second moment of area.

It is also evident that the lower leg projections and reconstructed images have far lower quality than at the mid-femur. This is probably due to the large missing regions in the projections that needs to be estimated. In these cases the known part that guides the estimation is relatively small. These results suggest that, in cross sections with two bones, further constraints or assumptions need to be added to the optimization objective function to further enhance the results.

We also faced a convergence problem in the lean images of the mid-femur using LI projections and in all lean images of the lower leg whether MPMD or LI were used. The DART algorithm did not converge after the initial ART steps. Since DART itself is a heuristic algorithm, there are no explicit conditions where algorithm convergence is guaranteed. However, an update to the original DART algorithm has been made [74], where they use a ―fixprobability" on each non-boundary pixel. According to this probability, this pixel can be included to or excluded from the next iteration. This value can be changed to insure convergence. We plan to implement this feature into our reconstruction algorithm SBART and test if this will improve the quality of the images derived from material decomposition.

Another modification that might enhance the estimated fat and lean tissue projection curves, would be to model them as splines rather than sums of sinusoids. Splines are smooth and can be used instead of higher order polynomials. However, the implementation is complex, especially due to the piecewise representation that requires numerous details to handle the matrices and variables.

In conclusion, the MPMD algorithm can be used in multi-projection three-material decomposition to estimate the bone shadowed missing parts of individual

projections. The results can be fed to the SBART or GC-SBART algorithms to reconstruct high quality cross sections from a small number of projections. Future work will include adding more constraints to the optimization function to improve the quality of the cross sections with two bones, testing splines as models for curves, and incorporating the fix probability parameter to ensure the convergence of the reconstruction algorithm.

Chapter 6

Femoral Neck Studies using DXA and CT

In this chapter, we present two clinical studies incorporating 2D engineering analysis on DXA scans of the hip and 3D CT-based study of cadaver femurs. The first study tests whether local buckling contributes to the strength of femoral neck cross-sections in the one-legged stance and the traumatic fall conditions. The second is a study of the effect of hormone therapy and physical activity on femur strength. The last study evaluates the relationship between mechanosensitivity and bone fracture. In the first study, we use the generated GEMs and FSMs from Chapter 3, while in the second and third, pre-acquired DXA scans of the hip are used.

6.1. Contribution of Local Buckling to Femoral Neck Failure

6.1.1. Background

Local buckling is a structural failure that occurs in thin-walled structures subjected to high compressive stresses. In this case, the actual compressive stresses at failure are smaller than the ultimate compressive stresses that the material is capable of withstanding. This kind of failure is due to elastic instability. In clinical orthopedics, fractures in the proximal femur are observed as compressive fractures that are often preceded by buckling and bending of microstructural elements or of the cortical shell [75-78].

Results of several studies suggest that the mechanism underlying the ability of DXA BMD to predict hip fracture is local buckling failure, but theoretical verification

using continuum FEA methods are problematic since continuum methods do not accommodate local buckling failure. A specialized version of FEA called Finite Strip Method (FSM) was designed to evaluate failure in pure elastic buckling in thin-walled structures [38, 39].

In chapter 3, we have developed a reliable method for deriving a smooth, geometrically accurate FSM model of the femoral neck cortex using CT scan data. In this study, we use these models to study mechanical stresses in the femoral neck bone in two situations. First, the one-legged stance mode, in which maximum load is imposed on the standing leg. This is a natural condition that happens in the normal gait cycle and it is expected that the bone is therefore adapted to it. Second, a fall with impact on the greater trochanter in which fractures could occur.

As described in the study workflow in Fig. 6.1, the stresses calculated from the last step are used in the buckling analysis of femoral neck cross sections under the same loading conditions. This determines if the local buckling contributes to failure or pure material yield is the only factor.

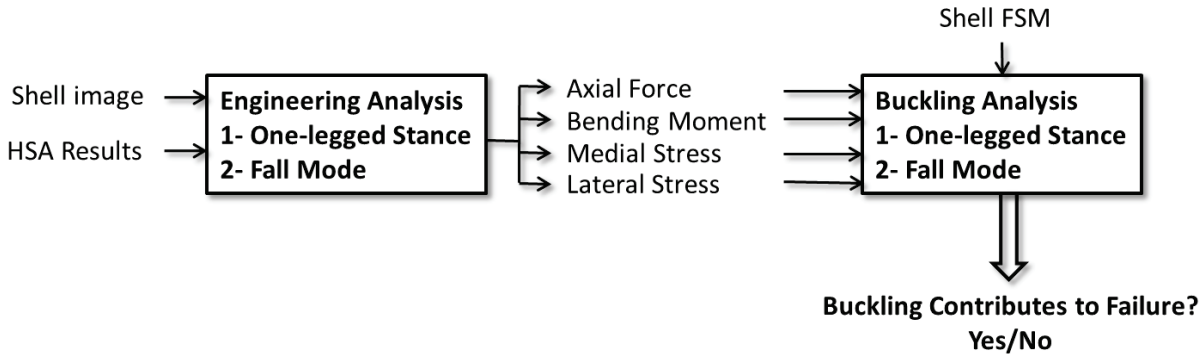

Fig. 6.1. Study workflow

6.1.2. Materials and Methods

6.1.2.1. Subjects

Six cadaver femurs from German subjects including 3 males aged 52, 66 and 93, and 3 females aged 65, 81 and 85 were scanned in a water bath using a 16 slice Siemens CT scanner with a slice spacing of 0.5 mm. Table 6.1 lists subjects data associated with their case number.

Specialized software was used to extract the cross-section at the minimum neck diameter and FSM models of the cortex were derived and evaluated in the plane of the neck-shaft angle as shown before in Chapter 3.

6.1.2.2. One-legged Stance Simulation

Simulation models are used to study the stress analysis over the femoral neck bone cross-section. Physiologic loads were simulated in a static one-legged stance as shown in Fig. 6.2, where three forces were employed with the femur shaft oriented with the shaft axis 10˚ to the vertical [79]. The acetabular joint reaction force F_J acts through the center of the femoral head. The ground reaction force at the knee F_K was equivalent to weight of the body minus that of the leg distal to the knee (~8/9 body weight) [80-82]. The abductor muscle force F_M was directed 70˚ to the vertical [79] and the magnitudes were adjusted to achieve static equilibrium (vector sums of all in-plane forces equal zero). A static equilibrium under a stance load generates a combination of axial compression and bending in the femoral neck, with maximum stresses in compression on the infero-medial surface of the narrow-neck cross-section.

Table 6.1. Subject Data

Case #	Sex	Age	Height (cm)	Weight (kg)
1	m	93	159	47
2	m	66	179	74
3	m	52	170	63
4	w	65	169	76
5	w	81	165	71
6	w	85	168	76

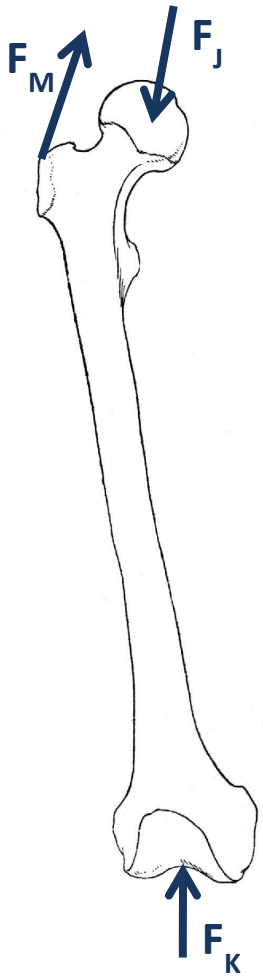

Fig. 6.2. Forces acting on Femur in case of One-legged Stance

6.1.2.2.1. Mechanical Model

A mechanical model of the femur, forces acting on it, and other parameters needed to define the geometry of the problem are shown in Fig. 6.3, where:

α: Neck-Shaft Angle (NSA)

θ : Angle of the resultant muscle force vector with the horizontal

Ø*:* Angle of the joint force vector with the horizontal

β: Angle of the femoral shaft with the vertical

NL: Neck Length

SL : Shaft Length

TL : Neck to Trochanter Length (assumed to be horizontal)

d: Neck to studied Cross-Section Length (at the narrowest point in the neck)

And the resolved forces and geometry are:

$F_{Mx} = F_M \cos\theta$ $F_{My} = F_M \sin\theta$

$F_{Jx} = F_J \cos\emptyset$ $F_{Jy} = F_J \sin\emptyset$

$SL_x = SL\cos(90^0 - \beta)$ $SL_y = SL\sin(90^0 - \beta)$

$NL_x = NL\sin(180^0 - \alpha - \beta)$ $NL_y = NL\cos(180^0 - \alpha - \beta)$

Forces and moments are balanced to achieve static equilibrium (i.e.$\sum F_x = 0$, $\sum F_y = 0$, $\sum M = 0$):

$$\sum F_x = 0 \qquad F_{Jx} = F_M \cos\theta \tag{6.1}$$

$$\sum F_y = 0 \qquad F_{Jy} = F_M \sin\theta + {}^{8}/_{9}\, W \tag{6.2}$$

$$\sum M = 0 \qquad F_M = \frac{8}{9} \cdot \frac{W}{TL} \cdot \frac{SL.\cos(90^o - \beta) - NL.\sin(180^o - \alpha - \beta)}{\sin\theta} \tag{6.3}$$

From(6.1), (6.2) and (6.3) F_{Jx}, F_{Jy} and F_M are computed, then we can get F_J and its angle Ø:

$$F_J = \sqrt{{F_{Jx}}^2 + {F_{Jy}}^2} \tag{6.4}$$

$$\text{Ø} = \tan^{-1}\frac{F_{Jy}}{F_{Jx}} \tag{6.5}$$

Given the values of α, *NL*, *W* and assuming that θ = 70° and β = 10°.

Femur shaft length SL (not measured in WHI) was inferred from the most widely used forensic formulae for US white and black adults *[83]* as

$$SL = \frac{height - 54.10}{2.47} \tag{6.6}$$

for white women, and as

$$SL = \frac{height - 59.76}{2.28} \tag{6.7}$$

for black women. For Asian/Pacific Islander women, forensic formula for Chinese [84] was used as:

$$SL = \frac{height - 61.72}{2.438} \tag{6.8}$$

For Hispanic and American Indian, forensic formula for Mesoamericans [85] *w*as used as:

$$SL = \frac{height - 47.25}{2.588} \tag{6.9}$$

All dimensions are in centimeters. Finally, the forensic formula for white women was used for women with unknown ethnicity.

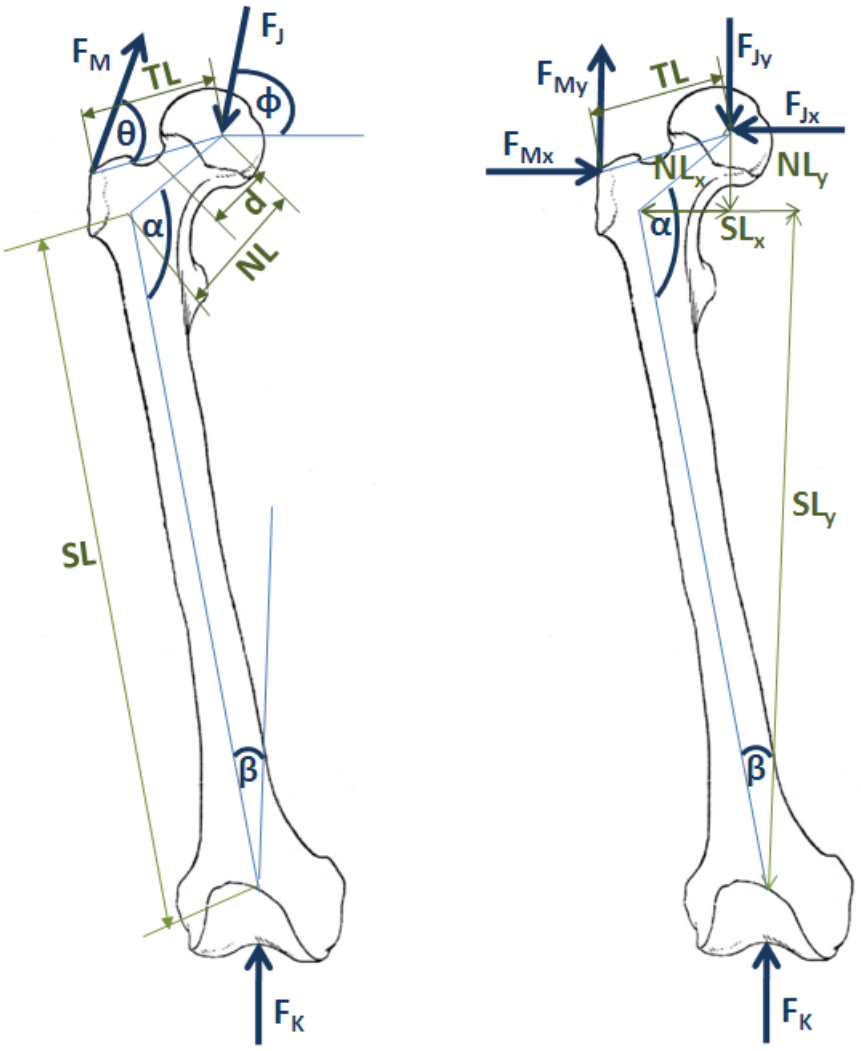

Fig. 6.3. Free-Body diagram of the Femur (a) forces in the original directions (b) forces resolved in x-y directions

6.1.2.2.2. Femoral Neck Free-Body Diagram

Internal Forces in the neck resulting from external forces F_M, F_J and F_K are shown in Fig. 6.4, where M_s, P_S and V are bending moment, axial load and shear force on the cortical cross-section. Shear forces are very small so that they were neglected in our calculations.

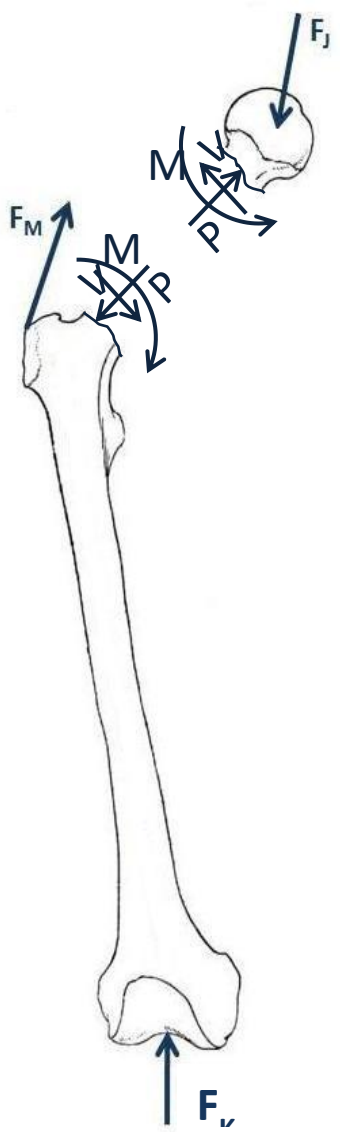

Fig. 6.4. Femur Internal Forces

Femoral neck free-body diagram is shown in Fig. 6.5. Bending moment M_S and axial force P_S are required to be calculated.

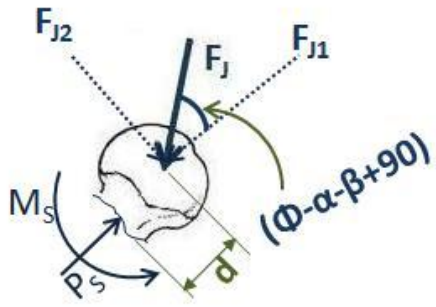

Fig. 6.5. Femoral neck Free-Body Diagram

$$P_S = F_{J1} = F_J \cos(\emptyset - \alpha - \beta + 90^O) \tag{6.10}$$

$$M_S = F_{J2}.d_x = F_J \sin(\emptyset - \alpha - \beta + 90^O).d \sin(180^o - \alpha - \beta) \tag{6.11}$$

6.1.2.2.3. Engineering Beam Theory

Axial stresses on the medial and lateral surface of the femoral neck are computed using simple beam theory:

$$\delta = \pm \frac{M_S.y}{I} + \frac{P_S}{A} \tag{6.12}$$

where M_S and P_S are the bending moment and axial load on the cortical cross-section (mentioned before), I and A are the cross-sectional moment of inertia, and the cortical area of the cross-section, and y is the perpendicular distance from the neutral axis of bending.

In our one-legged stance case:

$$\delta_{Medial} = +\frac{M_S . y_{Medial}}{I} + \frac{P_S}{A} \tag{6.13}$$

And

$$\delta_{Lateral} = -\frac{M_S . y_{Lateral}}{I} + \frac{P_S}{A} \tag{6.14}$$

where y_{Medial} and $y_{Lateral}$ are the perpendicular distances between medial and lateral surfaces, and the neutral axis.

In case of medial surface, bending moment and axial load produce compressive stresses (positive signs) while in case of lateral surface, bending moment produces tensile stress (negative sign) and axial load produces compressive stress.

6.1.2.3. Fall Mode Simulation

As shown in Fig. 6.6, The fall mode was simulated without muscle forces and with impact on the greater trochanter F_I, with the shaft at a fixed 10˚ angle from the impact surface. Equilibrium forces are F_H through the femoral head force and F_S acting on femoral shaft. F_I is assumed to be equal to body weight (W); F_H is approximately equal to 5/6 of the body weight or F_I, and F_S is approximately equal to 1/6 of the body weight or F_I..

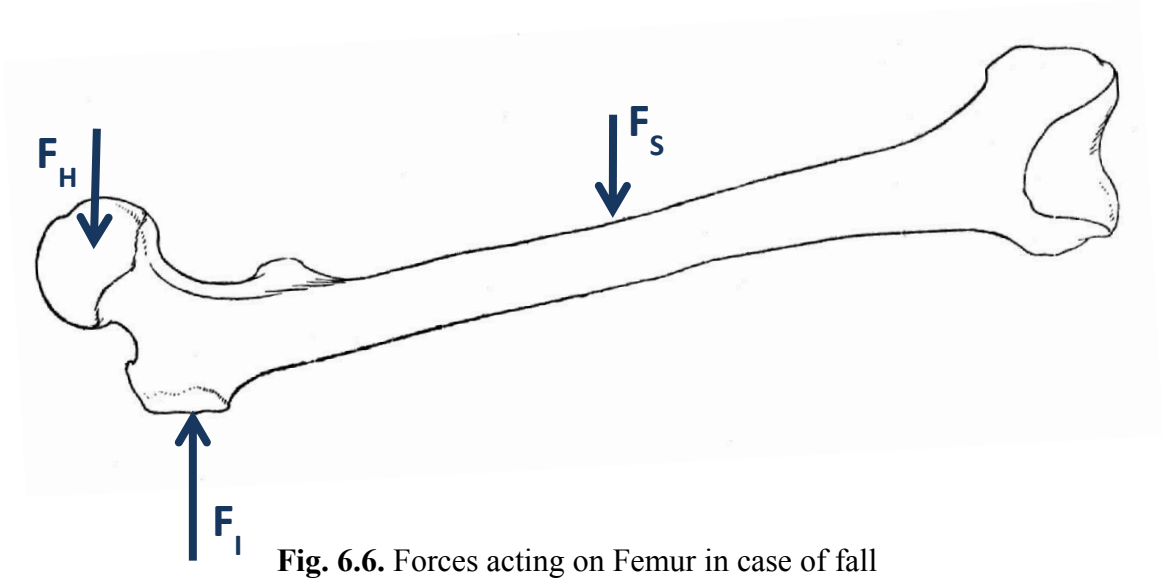

Fig. 6.6. Forces acting on Femur in case of fall

6.1.2.3.1. Mechanical Model

A mechanical model of the femur, forces acting on it, and other parameters needed to define the geometry of the problem are shown in Fig. 6.7, where:

α: Neck-Shaft Angle (NSA)

θ : Angle from the impact surface.

NL: Neck Length

d: Neck to studied Cross-Section Length (at the narrowest point in the neck)

Forces and moments are balanced to achieve static equilibrium (i.e.$\sum F_x = 0$, $\sum F_y = 0$, $\sum M = 0$):

where

$$l_1 = NL \cos\theta(180 - \alpha - \theta) \tag{6.15}$$

To find l_2 :

$$\sum M = 0 \qquad F_H\, l_1 = F_S\, l_2 \tag{6.16}$$

From(6.16), l_2 is computed**:**

$$l_2 = 5\, NL \cos\theta(180 - \alpha - \theta) \tag{6.17}$$

Given the values of α, *NL*, *W* and assuming that θ = 10°

6.1.2.3.2. Femur Neck Free-Body Diagram

Internal Forces in the neck resulting from external forces F_I, F_H and F_S are shown in Fig. 6.8, where M_F, P_F and V are bending moment, axial load and shear force on the cortical cross-section. Shear forces are very small so they were neglected in our calculations.

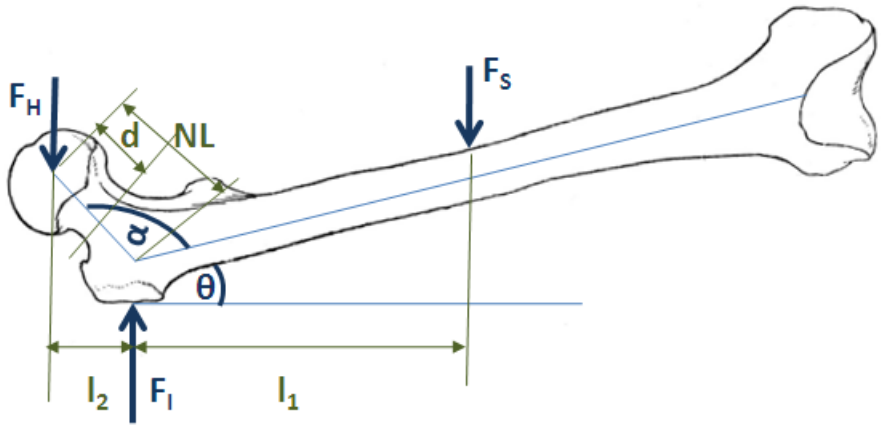

Fig. 6.7. Free-Body Diagram of the Femur

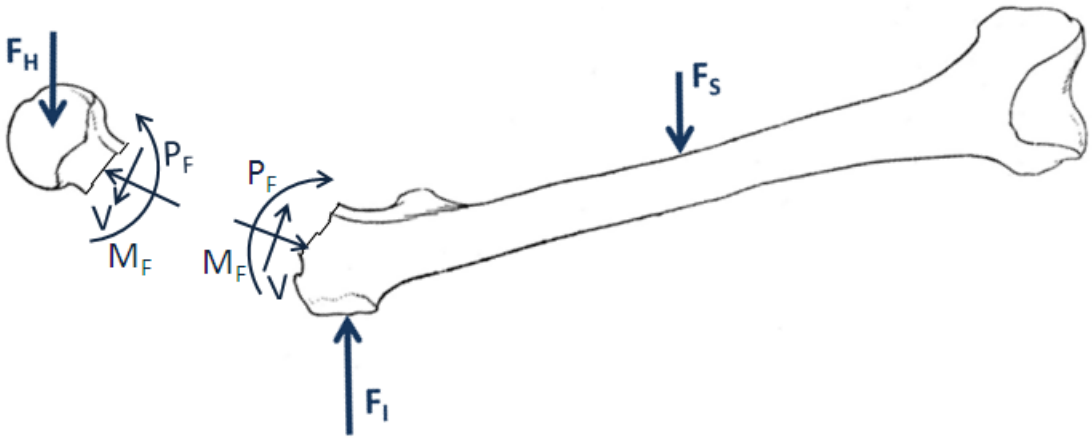

Fig. 6.8. Femur Internal Forces

Femoral neck free-body diagram is shown in Fig. 6.9. Bending moment M_F and axial force P_F are required to be calculated.

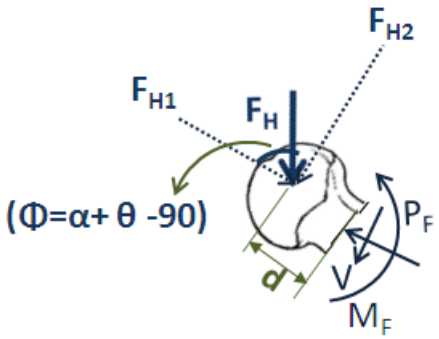

Fig. 6.9. Femoral Neck Free-Body Diagram

$$P_F = F_{H1} = \frac{5}{6} W \cos(\alpha + \theta - 90^O) \tag{6.18}$$

$$M_F = F_{H2} = \frac{5}{6} W \sin(\alpha + \theta - 90^O).d \quad (6.19)$$

6.1.2.3.3. Engineering Beam Theory

Axial stresses on the medial and lateral surface of the femoral neck are computed using simple beam theory:

$$\delta = \pm \frac{M_F.y}{I} + \frac{P_F}{A} \quad (6.20)$$

Where M_F and PF are the bending moment and axial load on the cortical cross-section (mentioned before), I and A are the cross-sectional moment of inertia, and the cortical area of the cross-section, and y is the perpendicular distance from the neutral axis of bending.

In our fall case:

$$\delta_{Medial} = -\frac{M_F.y_{Medial}}{I} + \frac{P_F}{A} \quad (6.21)$$

And

$$\delta_{Lateral} = +\frac{M_F.y_{Lateral}}{I} + \frac{P_F}{A} \quad (6.22)$$

where y_{Medial} and $y_{Lateral}$ are the perpendicular distances between medial and lateral surfaces, and the neutral axis.

In case of lateral surface, bending moment and axial load produce compressive stresses (positive signs) while in case of medial surface, bending moment produces tensile stress (negative sign) and axial load produces compressive stress.

6.1.2.4. Buckling Analysis

The objective of this analysis is to provide analytical evidence for local buckling failure. Presumably local buckling would be an unlikely failure mode at the femoral neck under stance loading since the bone geometry should be adapted to that loading condition. On the other hand the femur would not be expected to adapt its femoral neck geometry to the very different conditions encountered in a fall to the side impacting on the greater trochanter. Because the fall mode loads the femur with high compressive stresses in the thinner lateral regions of the femoral neck, one might expect that local buckling would be more likely. The finite strip model (FSM) of the shell along with the stress analysis results can be used to assess these two different conditions and the relative contributions of bucking to estimated failure.

Buckling analysis was performed using the open source program CUFSM developed by Professor Ben Schafer‘s thin-walled structures research group at Johns Hopkins University and described in details in [9]. CUFSM is software for exploring elastic buckling behavior, it calculates the buckling stress and buckling mode of arbitrarily

shaped, simply supported, thin-walled members. The finite strip method assumes longitudinal deformation occurs in half a sine wave (a half-wavelength), so the output half-wavelength is the length of the half sine wave assumed in the analysis. Analysis is performed for systematically increasing half-wavelengths to determine the behavior (mode shape and load factor) of a member. To perform finite strip analysis the member is loaded with a reference stress distribution. The product of load factor and the reference stress distribution yields the buckling stress. The load factor is the eigenvalue of the relevant eigenvalue buckling problem with the buckling mode as the eigenvector [9].

Shell FSM, axial compressive force (which serves as the reference stress distribution) and bending moments in the two simulation cases are used as input to the CUFSM program. The critical half-wavelength and load factor are the outputs from this program.

6.1.2.5. Buckling and Material Yield

We then use the output of the buckling analysis to predict the failure load and to determine failure results from pure material (bone tissue) yield, pure elastic instability (buckling) or a combination of both. Values of $\delta_{yt} = 115\ MPa$ and $\delta_{yc} = 182\ MPa$ were used for material yield in tension and compression respectively. Prediction of failure strength is attributed by Winter [86] as follows:

$$If\ \lambda \leq 0.673, where\ \lambda = \sqrt{F_y/F_{cr}}$$

$$F_n = F_y$$

$$Else$$

$$F_n = F_y(1 - \frac{0.22}{\lambda})/\lambda \quad (6.23)$$

Where F_n is the predicted failure load, F_y is the load required to cause material yield, F_{cr} is the critical elastic buckling load derived from CUFSM, and λ is the slenderness ratio.

6.1.3. Results

6.1.3.1. Stress Analysis of one-legged stance and fall

Fig. 6.10 shows FSM models in the 1st column along with stress distributions for the two simulated loading conditions (one legged stance and a fall with impact on the greater trochanter) in 2nd and 3rd columns. Compressive and tensile stresses are shown with red and blue lines respectively. The maximum stresses on the inferior (medial) and superior (lateral) surfaces in both simulated modes are plotted in Fig. 6.11 (a-b) respectively. In both modes, stresses are greatest in compression but the surfaces under greatest compression are reversed. In the one-legged stance the medial surface with the thickest cortex receives the greatest compressive stress. While in the fall mode the greatest compressive stress is on the relatively thin lateral cortex.

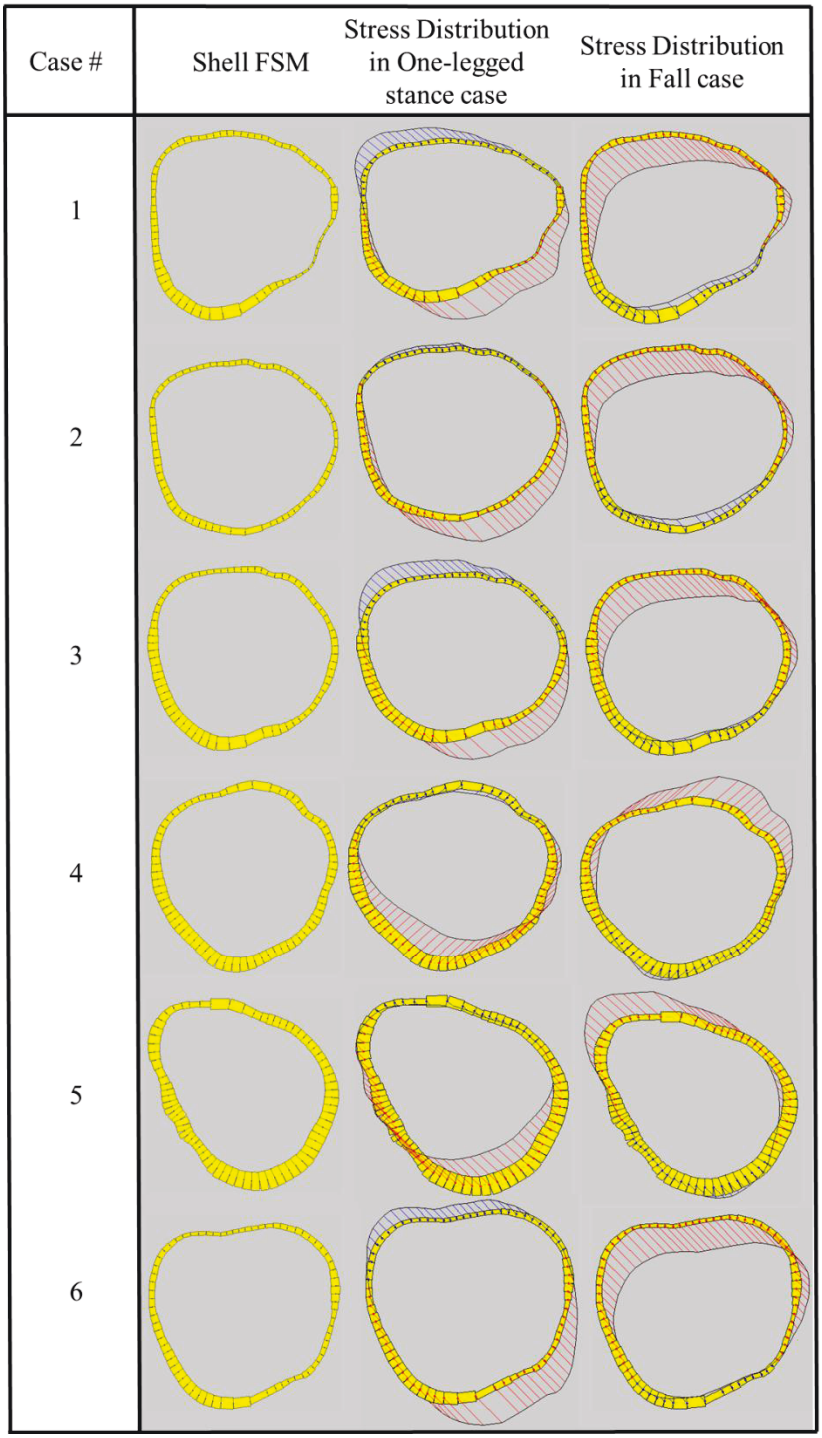

Fig. 6.10. FSM models shown in 1st column, and stress distributions for the two simulated loading conditions in 2nd and 3rd columns where compressive and tensile stresses are shown with red and blue lines, respectively.

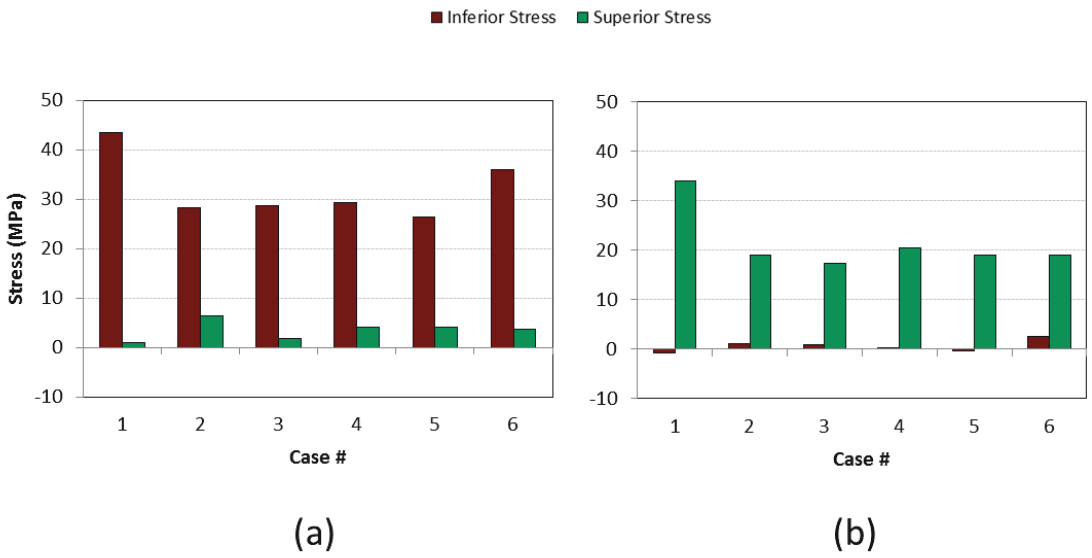

Fig. 6.11. Maximum stresses on inferior (medial) and superior (lateral) margins of the femoral neck cross-section in the plane of bending, under a) a one legged stance and b) a fall with impact on the greater trochanter.

6.1.3.2. Buckling Analysis

Fig. 6.12 shows the buckled shapes for the two simulation cases. Compared to Fig. 6.10, buckling occurred at the surface with compressive load whether in case of one-legged stance or in case of fall. Table 6.2 lists failure loads in material yield and pure local buckling as well as the predicted failure load using contributions from both, in one-legged stance and fall modes, respectively. Buckling loads were much lower in the fall mode where the thinner lateral cortex was under the greatest compression, compared to the stance mode. In the stance mode, local buckling did not contribute to femoral neck failure in any model so that the predicted failure load was equivalent to the material yield load as one would expect if the femur adapts to this condition. While in the fall mode,

buckling reduced strength (compared to pure material yield) in the 2nd , 3rd and 6th models from 13% to 40%.

In these three cases, slenderness ratio was $\lambda > 0.673$, as shown in Fig. 6.13 (b). According to Equation (6.23), this proves that these three bones encounter failure as a result of combined buckling and material yield. On the other hand, Fig. 6.13 (a) shows that slenderness ratio was $\lambda < 0.673$ in all cases. This agrees with the previous conclusion that the failure – if occur – will result from pure material yielding and buckling doesn‘t contribute to the predicted failure load.

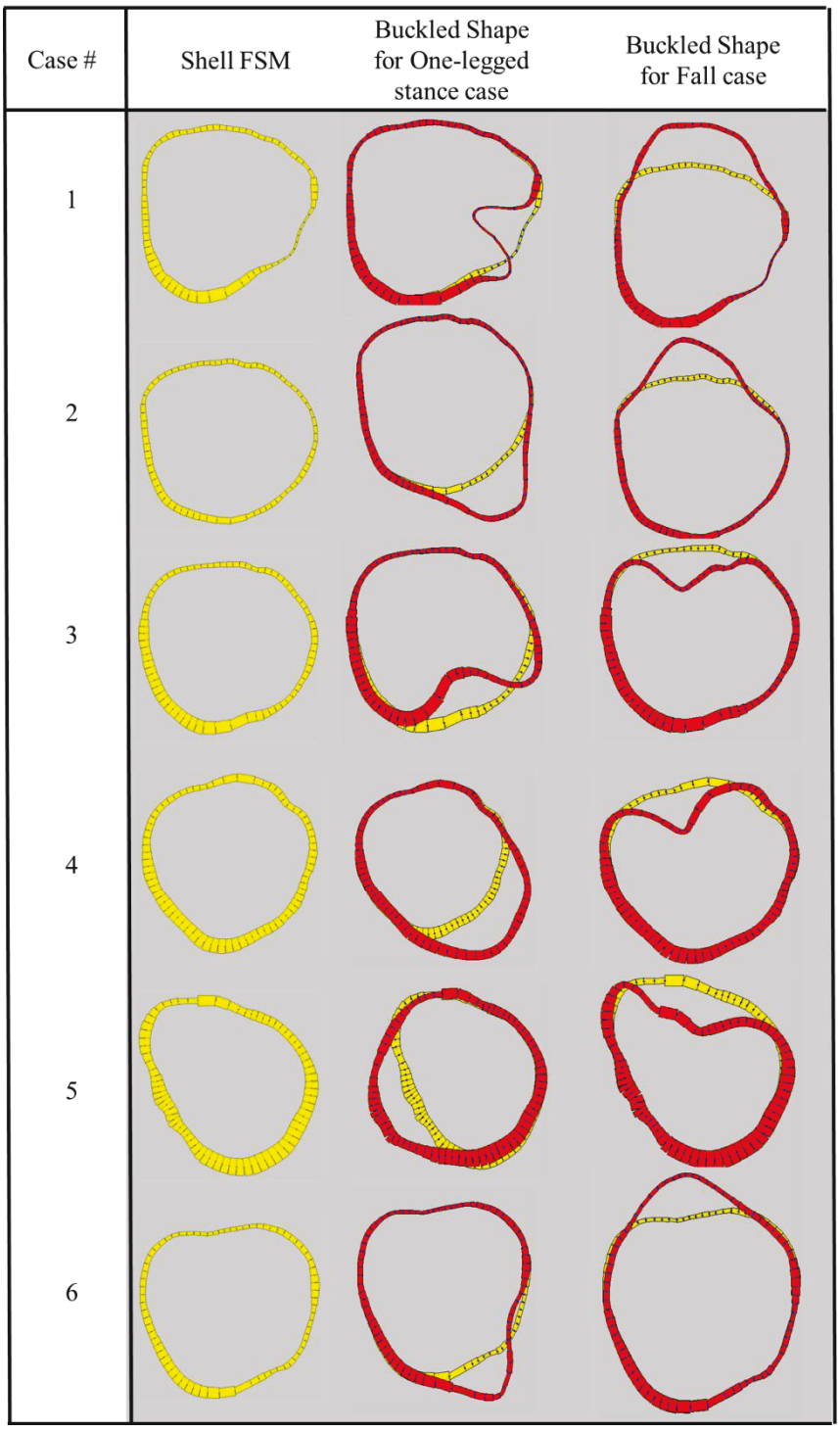

Fig. 6.12. FSM models shown in 1st column and buckled shapes for the two simulated loading conditions in 2nd and 3rd columns where buckled shapes (red elements) are superimposed over undistorted shapes

Table 6.2. Computed failure loads (N) required to produce pure material yield, pure local buckling and predicted failure considering both yield and local buckling for one-legged stance and a fall on the greater trochanter.

Case #	One Legged Stance			Fall on the Greater Trochanter		
	Material Yield	Pure Buckling	Predicted Failure	Material Yield	Pure Buckling	Predicted Failure
1	1931	11480	1931	2474	7218	2474
2	4656	28336	4656	**6923**	**8329**	**5761**
3	3911	45634	3911	**6479**	**11194**	**6053**
4	4621	95326	4621	6652	17484	6652
5	4790	91154	4790	6646	21528	6646
6	3772	19957	3772	**7124**	**5531**	**5061**

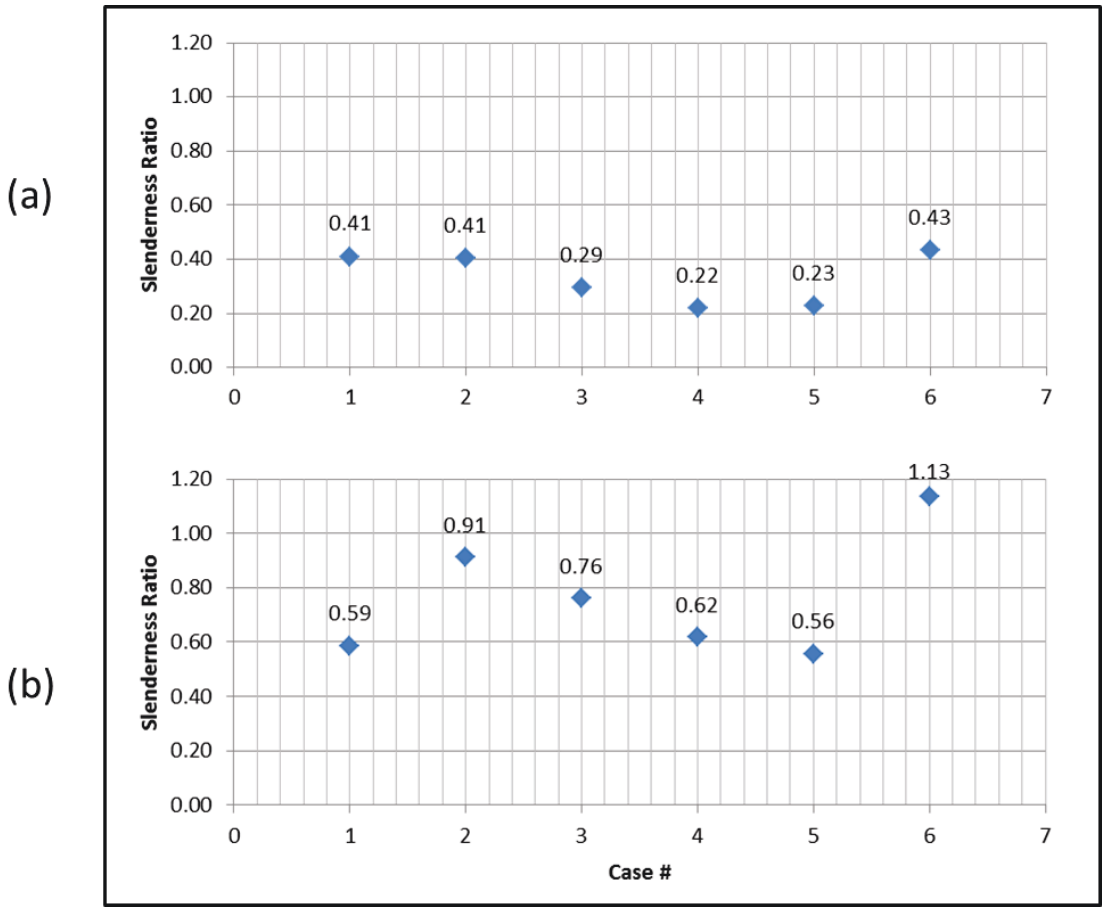

Fig. 6.13. Slenderness ratio in a) a one legged stance and b) a fall with impact on the greater trochanter

6.1.4. Discussion

It has been suggested that bone strength in elderly subjects may be very different when comparing normally accustomed loading conditions to which the bone adapts, and those unaccustomed conditions associated with traumas. The results of this preliminary analysis support the view that the cortical shell of the femoral neck is not susceptible to strength loss due to local buckling under physiologic loads but under the unaccustomed loads associated with a fall on the greater trochanter the geometry is less adapted.

Pure local buckling occurs in both loading configurations but requires a much smaller load in the fall mode than in the stance mode. However, when the thinner superior cortices are under compression, local buckling failure caused loss of strength in 3 of six femoral necks.

This preliminary analysis considered only the cortical shell, future versions of the simulations will incorporate internal support provided by the trabecular core. However, we did not expect that the results will vary too much since trabeculae are sparse in the elderly femur.

6.2. Effect of hormone therapy and physical activity on the femur bone

6.2.1. Background

In theory, bones adapt continuously throughout life to mechanical loads imposed by prevalent physical activities. Load stimuli take the form of dynamic, minute deformations (strains) of loaded bone tissue detected by osteocytes that initiate the signaling response [87, 88]. According to the Frost Mechanostat the resulting adaptation serves to ensure that the bone morphology is adjusted to keep strains generated by prevalent loads within certain minimum and maximum limits [89, 90]. It has long been postulated that estrogen enhances sensitivity to load stimuli [91] and work in cell cultures of human osteocytes support this view [92, 93]. Further evidence in genetically engineered mouse models suggest that the estrogen receptors α and β are critical components of mechanotransduction [94, 95]. This should mean that for equivalent skeletal load stimuli, bones in estrogen-replete women should be adapted to be mechanically stronger than in those who are deficient. We previously showed that women currently on hormone therapy have mechanically stronger proximal femur geometry than in never-treated women [96] and similar effects have been shown with women in clinical trials treated with estrogen [97] or with the selective estrogen receptor modulator raloxifene [98]. The biological evidence also suggests a more subtle effect, that the positive effects of physical activity should be greater in the presence of estrogen. This may have important ramifications for therapies employing the estrogen pathway since it would suggest that they should include mechanical loading. The purpose of the present study was to determine if exercise enhancement of hormone therapy (HT) could be detected in femurs

of women participating in the observational cohort of the Women‘s Health Initiative (WHI-OS).

Our analysis was based on the following logic. First we assumed that the femur geometry in individuals is adapted to their prevalent physiologic loading conditions. As shown in animal models [95], an estrogen effect on load sensitivity should mean that adaptation to increased loads produce a larger decrement in peak load strains than seen in an estrogen deficient state. Unfortunately strains cannot be determined non-invasively in vivo but assuming that the bone material is invariant, strains are proportional to stresses. Stresses can be computed using engineering methods incorporating knowledge of the bone geometry and of the load characteristics. Ideally maximum stresses would be computed under the prevalent physiologic loads that generated the adaptation. But load history cannot be easily determined with the type of data usually available in clinical studies. We therefore hypothesized that the maximum stress in the femoral neck generated in a one-legged stance under a fixed body weight load would be smaller in women treated with estrogen compared to never users. We further hypothesized that the decrement in maximum stress would be greater with increasing activity level with a greater decrement among HT users compared to non-users.

6.2.2. Materials and Methods

6.2.2.1. Subjects

This work arose as a part of ancillary study #153 of the Women‘s Health Initiative (WHI) which funded the analysis of the hip scans acquired by dual energy x-ray absorptiometry with the Hip Structure Analysis software. Although the interventional data were also analyzed in the ancillary study, the current report employs only baseline data from

subjects enrolled in the observational cohort. These include women over 50 of all races who had DXA scans of the hip and total body measured at one of four sites: the University of Alabama at Birmingham, the University of Pittsburgh, and the University of Arizona campuses at Phoenix and Tucson. A total of 6032 subjects had hip scans analyzed by HSA at baseline; after excluding 875 past users, 2457 current HT users were compared to 2697 never-users after division into activity tertiles. Recreational physical activity was assessed by questions on the frequency and duration of several types of recreational activity, and Metabolic Equivalent Task (MET) scores (defined as the ratio of work metabolic rate to a standard resting metabolic rate, with 1 MET roughly equivalent to the resting metabolism while sitting quietly) were computed as the product of days per week, minutes per day and MET value for each activity [99].

6.2.2.2. Engineering Analysis

Due to the 2-dimensional limitations of DXA scan data the engineering analysis was restricted to loads within the frontal plane defined by the axes of the femoral neck and shaft. The one-legged stance simulation described before in section 6.1.2.2 is used here.

The frontal plane cross-sectional moment of inertia I and the cross-sectional area A of the narrowest neck cross-section were derived from DXA data by the Hip Structural Analysis (HSA) method [100], as were the neck-shaft angle α, neck length NL, distance of the neck cross-section from the center of the femoral head d, and the distance from the center of the femoral head to the most lateral point on the greater trochanter TL. Femur shaft length SL (not measured in WHI) was inferred from the most widely used forensic formulae as shown in section 6.1.2.2.

6.2.2.3. Statistics

Group characteristics and comparisons of femur geometry measures were compared between groups by general linear model (ANCOVA) with and without lean mass fraction as a covariate. Welch's t-test was used to determine statistical differences between groups. All statistics were done using IBM SPSS Statistics for Windows version 20 (SPSS Inc., Chicago, IL, USA).

6.2.3. Results

6.2.3.1. Participant Characteristics

Participant characteristics are shown in Table 6.3. Age, Weight and BMI of never HT users are slightly higher than current HT users, while both have similar lean mass fractions. Lean mass fraction rises with increased level of reported activity in both HT user groups.

Table 6.4 shows the ethnicity characteristics of the participants. Most of were white, about 74% among the never HT users group, and 83% among the current HT users group. Blacks were the next most common ethnic group with 14% and 8% in never and current HT users respectively. Hispanic and American Indian accounted for 10% and 7% of both groups, while Asian or Pacific Islanders were less than 1% in both groups.

No correlation was found between age and lean mass fraction or age and load stress, indicating that it was unnecessary to add age as a covariate in the statistical analyses ($p > 0.2$).

Table 6.3. Participants characteristics for never HT users and current HT users divided into tertiles of physical activity

HT Category	Activity	N	Mean (SD)				
			Age (Years)	Weight (kg)	Height (cm)	BMI	Lean Mass Fraction
Never Users	Lowest	749	65.14 (7.29)	76.27 (16.79)	160.79 (6.39)	29.49 (6.25)	0.54 (0.067)
	Middle	700	65.29 (7.24)	72.08 (15.93)	160.99 (6.06)	27.79 (5.83)	0.55 (0.071)
	Highest	670	65.21 (7.16)	69.16 (14.40)	161.14 (6.11)	26.63 (5.30)	0.58 (0.077)
	Total	**2119**	**65.21 (7.23)**	**72.64 (16.05)**	**160.97 (6.19)**	**28.03 (5.94)**	**0.56 (0.074)**
Current Users	Lowest	614	61.61 (7.25)	72.46 (15.70)	161.81 (5.97)	27.72 (5.98)	0.55 (0.069)
	Middle	661	62.19 (7.06)	69.17 (12.74)	162.40 (6.24)	26.22 (4.59)	0.56 (0.064)
	Highest	740	62.32 (7.26)	69.97 (11.88)	162.32 (6.08)	25.40 (4.18)	0.59 (0.070)
	Total	**2015**	**62.06 (7.19)**	**69.37 (13.61)**	**162.19 (6.10)**	**26.38 (5.01)**	**0.57 (0.070)**

Table 6.4. Ethnicity characteristics for never HT users and current HT users divided into tertiles of physical activity

HT Category	Activity	N	Ethnicity (N (%))					
			White	Black	Hispanic	American Indian	Asian/Pacific Islander	Unknown
Never Users	Lowest	749	501 (66.89)	156 (20.83)	64 (8.54)	19 (2.54)	2 (0.27)	7 (0.93)
	Middle	700	540 (77.14)	79 (11.29)	62 (8.86)	13 (1.86)	2 (0.29)	4 (0.57)
	Highest	670	537 (80.15)	73 (10.90)	40 (5.97)	11 (1.64)	0 (0.00)	9 (1.34)
	Total	**2119**	**1578 (74.47)**	**308 (14.54)**	**166 (7.83)**	**43 (2.03)**	**4 (0.19)**	**20 (0.94)**
Current Users	Lowest	614	481 (78.34)	75 (12.21)	44 (7.17)	7 (1.14)	3 (0.49)	4 (0.65)
	Middle	661	565 (85.48)	48 (7.26)	40 (6.05)	4 (0.61)	2 (0.30)	2 (0.30)
	Highest	740	642 (86.76)	46 (6.22)	38 (5.14)	6 (0.81)	3 (0.41)	5 (0.68)
	Total	**2015**	**1688 (83.77)**	**169 (8.39)**	**122 (6.05)**	**17 (0.84)**	**8 (0.40)**	**11 (0.55)**

6.2.3.2. Association between tertile of activity and Hormone usage

Stresses for HT groups were broken down by tertile of activity level and compared to the least active tertile. Fig. 6.14 shows maximum medial neck stresses computed with body weight as load by tertile of physical activity. In both never and current HT users, stresses were significantly different between successive tertiles ($p<0.001$). When stresses were computed with body weight as load, they generally decline (indicating strength improvement) with increasing activity; the effect is greater among HT users ($p< 0.001$ for HT and activity effects).

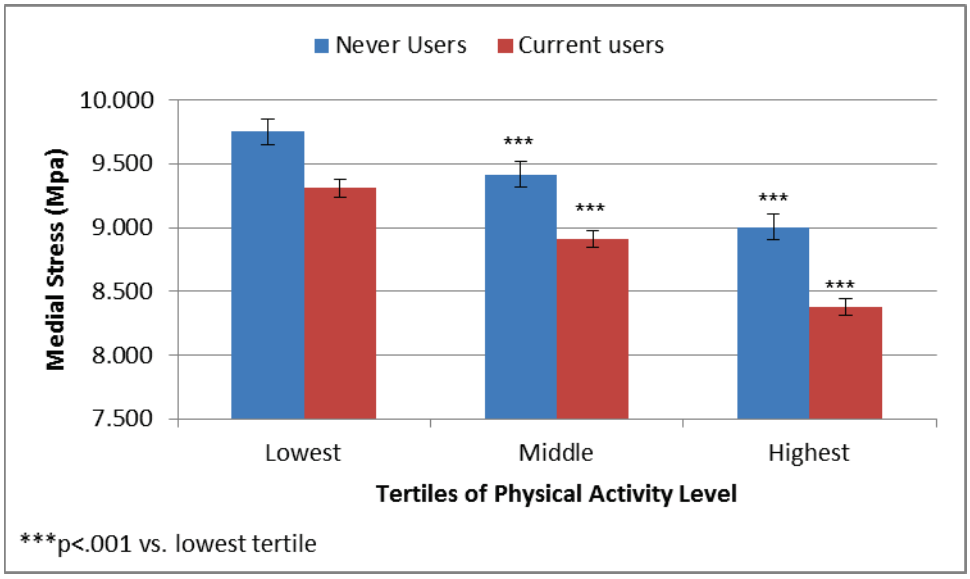

Fig. 6.14. Maximum medial neck stress by tertile of physical activity. All differences between tertiles and between never and current users $p<0.001$.

After adjustment for lean body mass (mostly muscle), the differences between activity tertiles became non-significant among non HT users indicating that increasing muscularity accounts for the activity effect on stress in this subgroup. Importantly, although differences were diminished among HT users, they remained significantly different between tertiles as shown in Fig. 6.15 ($p < 0.013$ middle vs. lowest activity level and $p < 0.001$ highest vs. lowest activity level). This result indicated that there is a significant interaction between activity level and estrogen such that activity effects on bone in the presence of estrogen are greater than expected from the greater muscularity alone.

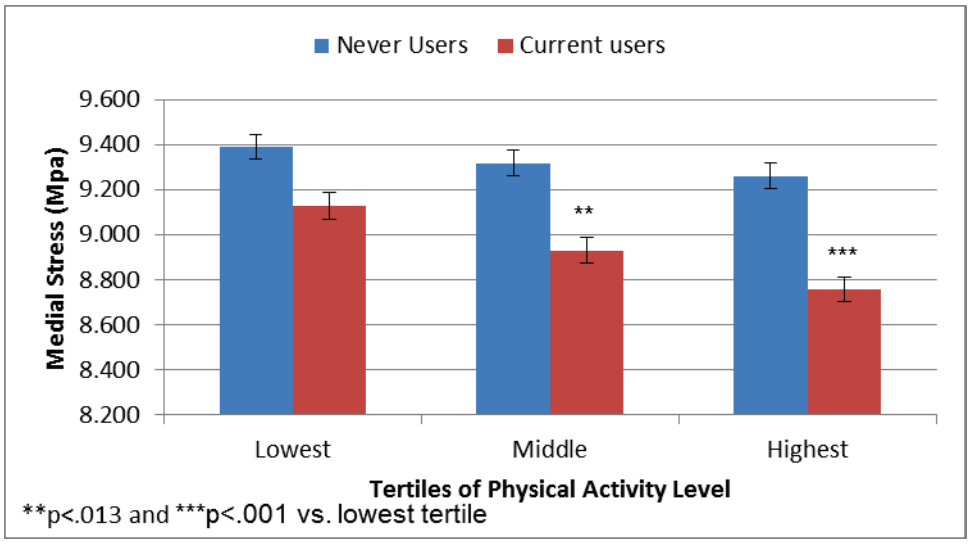

Fig. 6.15. Maximum medial neck stress by tertile of physical activity after adjustment for lean mass fraction. Differences between tertiles are non-significant in Never-users but are significant in current users ($p<0.013$ middle and $p<0.001$ highest versus lowest tertile).

6.2.4. Discussion

In a one-legged stance mode as occurs during ambulation, stresses are highest along the medial surface of the femoral neck. In an individual, the femur geometry should be adapted to the maximal physiologic loads that are routinely encountered so that these stresses do not exceed some limiting value. If all bones responded identically to load, the stresses generated under a maximal (physiologic) load should be identical. In truth we don‘t actually know the maximal loads, but since they are some function of body weight [101], we computed stresses using body weight as load. The geometry should be adapted to keep maximum stresses within physiologic limits by generating a formation response when load generated strains exceed a certain threshold. If estrogen influences the formation threshold, those with an estrogen deficiency should adapt their bones to have higher femur stresses compared to women on HT as we have observed. Note that the maximum loads that the femur will experience are a multiple of body weight, a factor that increases with intensity of exercise.

The effect of physical activity is somewhat subtle and it may not be readily obvious why the stress should decline with increased activity. Physiologic forces on the femur from ambulation are dominated by muscle action, typically rising to several times body weight during stance and ambulation with increasing multiples in more intense activities like running [101, 102]. The femurs in more active individuals adapt to higher loading forces, thus the stresses generated under a single body weight load should be relatively smaller, as we observe. More importantly, maximum stress goes down with increasing activity level among both HT users and non-users indicating that more active women have strengthened their femurs by adapting their geometry to the higher activity.

We cannot actually measure the muscle force magnitudes that have stimulated adaptation in an individual but because activity builds muscle mass one would expect that to a first order, muscle force should scale with total body lean mass. Thus if the effect on bone (stress) is eliminated by adjusting for muscularity (lean mass fraction of weight) this would suggest that the bone effect is entirely due to the greater muscle force in the more active groups. Indeed the differences between activity tertiles became non-significant in postmenopausal women who never took estrogen supplements. However it is critical to point out that the activity effect on bone was not entirely eliminated by adjustment for muscularity among women on HT. The observation that stresses are relatively lower in women using estrogen in all activity levels after adjusting for lean mass (Fig. 6.3) suggests that there is a more effective geometric adaptation to muscle forces when estrogen replete. This is further confirmed in our observation that stresses continued to significantly diminish with increased activity level after adjusting for lean body mass. Not only does the femur respond better to increased activity level in the presence of estrogen, but the effect is greater than that expected with increased muscularity alone. This finding is consistent with the speculations of Jarvinen [91] and with the human osteocyte cell culture observations of Joldersma [93]. The therapeutic implication is that estrogen treatment effects on bone appear to be enhanced by exercise suggesting that the same might be true for treatments with similar pharmacologic effects such as the selective estrogen receptor modulators (SERMs). We are not aware that such studies have been done to date.

Our observation that load stresses do not increase with age would seem to be completely inconsistent with the vast body of unequivocal evidence showing age declines

in BMD and bone mass associated with increasing fracture rates. Paradoxically it is consistent *in vitro* evidence indicating cellular response to mechanical stimuli does not appear to degrade with age. How can this conflicting evidence be reconciled? First our analysis evaluates hip stresses with forces oriented in directions normally encountered in ambulation and not those very different conditions encountered in a fall on the hip. In stance, forces concentrate on the thick inferomedial cortex that thins little with age (Mayhew, Iceland CT data). But in a fall to the side impacting on the greater trochanter, very high compressive forces are generated in the superior lateral cortex which clearly does thin with age, especially in those who go on to fracture. Secondly the observation that stresses computed with individual body weight do not increase with age does not mean that absolute bone strength is static. Strength tracks with load (~weight) and should adjust up and down as that load changes across the age span. Weight does tend to decline in older subjects; indeed body weights and femoral neck cross-sectional areas and section moduli, (indices of strength in axial compression and bending) do decline with age in this population (data not shown).

We conclude that physical activity effects in estrogen-deficient women improve both lean mass and femur strength, but there is an additional independent effect of activity on femur strength in HT users.

6.3. Relationship Between Reduced Mechanosensitivity and Fracture Incidence

6.3.1. Background

Bone tissue has evolved the remarkable capacity to restore and renew itself by remodeling; and because the mechanism appears to be imbalanced by aging and osteoporosis, research on causes of osteoporotic fragility has concentrated on restoring remodeling balance. But bone tissue also has the ability to adapt (model) its geometry and perhaps its material properties to changes in mechanical conditions imposed by normal physical activity [103]. The purpose of adaptation is to adjust the amount and distribution of the bone tissue within bones so that it is suited to resist the loading forces imposed by normal physical activities of daily life. This implies that except during adaptation to altered load, there is equilibrium between the loading forces or more properly the stimuli they generate within bones and the structural geometry resulting from adaptation.

Equilibrium is between the normal loading forces on bones produced by physical activity and the deformations (strains) of the bone tissue produced by those forces. Frost has articulated the mechanism as a 'Mechanostat' which functions to keep load-generated strains within a physiologic range by generating signals when average daily strains exceed those limits [104]. Strains exceeding the upper threshold stimulate new bone formation in regions where strains are too high while reduced loading stimulates resorption on bone surfaces where load strains fall below the lower threshold. Good examples of modeling response to increased loading can be seen in the small animal ulnar loading animal models of Turner [105]. The net effect of modeling should be that the

addition of bone material where strains increase and the removal where strains decline should continually alter the geometry so that strength remains in equilibrium with current demands.

The importance of the modeling mechanism is that it may not work equally well in all individuals and variability may have implications for fracture risk. Differences in sensitivity to load stimuli should mean that some individuals require higher strains to generate a response than others. In relative terms, this would mean that when subjected to the same load stimuli they adapt their bones to be relatively weaker. One should also expect that some individuals have heightened mechanosensitivity and they should generate relatively stronger bones under equivalent loads. If this is true, and if we further assume that exposure to trauma is uniformly distributed in the population, those with reduced mechanosensitivity should be more likely to suffer fractures.

Differences in load response should alter the equilibrium between the normally encountered load and maximum strains that the load induces within the bone. Although bone strains can‘t be measured non-invasively they should be proportional to load stresses so the equilibrium should be evident in the maximum stresses generated by the normally encountered load. In the present study we computed the stresses generated in a one-legged stance on the inferior- medial surface of the narrowest cross-section of the femoral neck. This is a site that is normally under compression, adapted to upright walking [106], and the cortex is relatively well preserved in both men and women with age [107].

We hypothesized that maximum stresses at this site would be higher in postmenopausal women with a history of either incident or prevalent fracture when

compared to women without fractures. Structural geometry for the model was derived from dual energy x-ray absorptiometry (DXA) scans using the HSA method in a subset of women from the observation cohort of the multi-center Women‘s Health Initiative (WHI). The engineering model was based on beam principles and was evaluated for loading constrained to the 2-dimensional plane of the DXA image.

6.3.2. Materials and Methods

6.3.2.1. Subjects

Same dataset was used as outlined in section 6.1.2.1. From the total of 6032 subjects, 3614 self-reported no fracture of any bone in their lifetime prior to enrollment and 2418 reported at least one fracture. These women were further subdivided into groups with and without incident fractures of any bone; a total of 809 women suffered an adjudicated fracture of one or more bones during the ~8.5 years of follow-up. In this study no distinction was made between type of fracture or the severity of trauma associated with its production. The final categories comprised women is shown in Table 6.5.

6.3.2.2. Engineering Analysis

Engineering analysis is performed on a femur as described before in sections 6.1.2.2 and 6.2.2.2.

6.3.2.3. Statistics

Group characteristics at baseline were compared using ANOVA. Comparisons of femur geometry measures were compared between groups by ANCOVA with subject age, height and weight at baseline as covariates.

Table 6.5. Subject Categories

Category	Description	Number of subjects (N)
Hx--	With neither prior nor incident fracture	3231
Hx+-	With prior but no incident fracture	1992
Hx-+	With no prior but with incident fracture	383
Hx++	With both prior and incident fractures	426

6.3.3. Results

The characteristics of the four study groups are listed in Table 6.6. Those with either prevalent (Hx+-), incident (Hx-+), or both fractures (Hx++) were slightly older than fracture-free (Hx--) with the oldest among those with Hx++. Interestingly women with Hx++ expended about 8% greater amount of energy from exercise compared to Hx-- or other groups. Somewhat discordant with this finding was that Hx++ women had slightly lower BMI compared to other groups. BMI and body composition differences however were slight and probably unimportant.

Ethnicity characteristics of the participants are listed in Table 6.7. Most of them were white, about 77% among all participants. Blacks and Hispanic follow next with 13% and 7% of all women respectively. American Indians and Asians or Pacific Islanders were only 1.5% and 0.4% respectively.

Table 6.6 Participants characteristics divided according fracture category

Fracture Category	N	Mean (SD)						
		Age (Years)	W (kg)	H (cm)	BMI	Fat Mass Fraction	Lean Mass Fraction	Total expenditure from physical activity (m)
Hx--	3231	63.14 (7.41)	71.87 (15.52)	161.61 (6.20)	27.53 (5.81)	0.42 (0.076)	0.56 (0.074)	15.33 (15.07)
Hx-+	1992	64.08 (7.35)	72.99 (15.88)	161.48 (6.07)	27.99 (5.91)	0.43 (0.075)	0.55 (0.073)	14.91 (15.13)
Hx+-	383	64.70 (7.38)	71.47 (14.87)	161.64 (6.47)	27.32 (5.28)	0.43 (0.074)	0.56 (0.070)	13.79 (13.31)
Hx++	426	65.64 (7.49)	70.86 (14.97)	161.54 (6.44)	27.15 (5.49)	0.43 (0.078)	0.56 (0.074)	15.89 (14.15)
Total	**6032**	**63.73 (7.43)**	**72.14 (15.57)**	**161.57 (6.19)**	**27.64 (5.79)**	**0.42 (0.076)**	**0.56 (0.073)**	**15.14 (14.92)**

Table 6.7 Ethnicity characteristics for participants divided according fracture category

Fracture Category	N	Ethnicity (N (%))					
		White	Black	Hispanic	American Indian	Asian/Pacific Islander	Unknown
Hx--	3231	2281 (70.6)	573 (17.73)	286 (8.85)	51 (1.58)	16 (0.50)	24 (0.74)
Hx-+	1992	1661 (83.38)	165 (8.28)	116 (5.82)	31 (1.56)	4 (0.20)	15 (0.75)
Hx+-	383	315 (82.25)	36 (9.40)	21 (5.48)	6 (1.57)	2 (0.52)	3 (0.78)
Hx++	426	385 (90.38)	13 (3.05)	18 (4.23)	5 (1.17)	1 (0.23)	4 (0.94)
Total	**6032**	**4642 (76.96)**	**787 (13.05)**	**441 (7.31)**	**93 (1.54)**	**23 (0.38)**	**46 (0.76)**

Stance mode stress showed no significant effect of age. However, the use of hormone therapy, greater lean mass fraction (from total body DXA) and weekly energy expended in physical activity suppressed stresses ($p < 0.01$). After correcting for these covariates, mean stresses in MPa (95% CI) are plotted in Fig. 6.16. Stresses in fracture groups are significantly higher than those who do not fracture and are highest among women with both past history of fracture and incident fracture (Hx++).

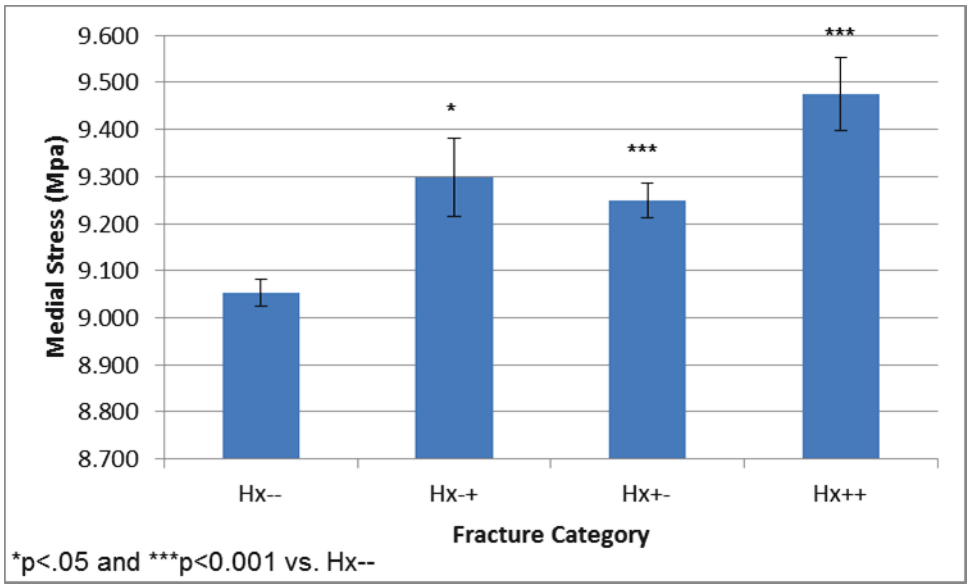

Fig. 6.16. Maximum stresses on the infero-medial cortex of the femoral neck at its narrowest point in a one-legged stance, adjusted for HRT use, lean mass fraction and physical activity score.

6.3.4. Discussion

If exposure to traumatic conditions were evenly distributed through the population, one would expect that fractures would be more likely in those with relatively weaker bones. In this study women who reported a prior fracture of any bone had measurably more _delicate' proximal femur structure than those who remained without fractures, independent of age and body size. All three femur cross-sections showed measurably smaller resistance to axial and bending loads compared to their fracture free counterparts.

Other studies have also shown that subjects with prevalent fractures are more likely to fracture again. For example a review of the literature by Klotzbuecher and colleagues showed that prior facture history in either men or women produced an approximate doubling of the risk of future fractures when all fracture types were included [108]. The risk of a vertebral fracture was four times greater if there is evidence of a prior vertebral fracture. These findings were borne out in a recent study of men and women in the Framingham cohort [109], where those with a prevalent moderate or severe vertebral fracture had five times the incidence of new vertebral fractures compare with those without an existing fracture.

We have shown that women who fracture have weaker bones independent of age and body size but have not speculated on why this is so. Conceivably women of the same size who get more exercise place more demands on their bones and conceptually bone strength should be adapted to the prevalent mechanical loading demands or in other words the strength is in equilibrium with them. One could have weaker bones in an absolute sense if they are proportionately adapted to diminished loading demands, and this could occur with a normal strength/load relationship. Interestingly we found that

fracture groups appeared to have an anomalous sense; bone may be weaker because these women may have an anomalous strength/load relationship.

One important question is how these findings can be used in the clinical setting. Some caution is clearly necessary here, while we have shown that the effect can be detectable in a large sample of women, it is another matter to do so in an individual. Bone density scanners were not designed to measure bone geometry, and the current level of precision with the HSA method used here is not yet good enough for clinical use [110]. Technological improvements should ultimately improve the level of precision but perhaps the message should be that there are apparent strength differences in those who fracture that can be measured. The best method for doing so is yet to be determined. We suspect that the concept behind the measurement should somehow evaluate the strength/skeletal load relationship. A similar concept has been used by Shoenau and colleagues using a CT scan through a limb to measure both the bone and the muscle in the cross-section [111-113].

Intended to be blank.

Chapter 7

Conclusions and Future Work

The research for this dissertation was mainly dedicated to the investigation of principles and methods that could be employed in a commercial multi-projection DXA scanner system that could provide an engineering analysis of patient limb bones rather than merely a density test. Ideally the scanner would automate 3D data acquisition and generation of the engineering model of the patient bone and do so in an instrument that is functionally as simple as a conventional 2D DXA scanner. There are however many technical challenges in meeting this goal and several important ones have been addressed in this dissertation.

One of the most important goals is to generate high quality geometrically accurate 3D images of the bone in a limb and to do so at a very low radiation dose. Since to a first approximation the radiation dose scales with the number of projections, the goal is to provide the most accurate reconstruction with the fewest number of projections. The reconstruction process can be greatly simplified by using DXA data and by limiting the number of materials (gray shades) to the bone, fat and lean in the human limb. The missing tissue projection data resulting from the two-material limitation of DXA methods can be addressed by using an improved interpolation algorithm to differentiate fat from lean in the shadows of bones. The design of the scanner system can be simplified and made less costly by limiting the angle of system rotation. The mapping of the 3D bone

data to an engineering model can be simplified to permit automation by the use of a geometrically equivalent model that corrects for blurring effects and does not resort to the problematic density modulus relationship that is difficult to automate. All of these issues were addressed in this dissertation.

The successive binary algebraic reconstruction technique (SBART) uses as few as three and we tested up to thirteen projections over a rotation angle limited to 90° to provide good quality reconstructions. This iterative method first reconstructs the bone cross-section and can do so accurately with as few as 5 projections even with a cross section with two distinctive bones such as the lower leg. This fashion ensures that the bone cross section – which is reconstructed first – is very accurate. Then the reconstruction of fat tissue to follow excluding the bone areas, and finally lean tissue is reconstructed in the same way. A major advantage is present if the skin line is known and introduced as a priori information to SBART algorithm. In this case the reconstructed cross sections are extremely enhanced. This also enables us to use fewer projections than we have to use if the skin boundary is unknown.

An advanced version of SBART is also introduced, where the second moment of area is used as a geometrical constraint. The geometrically-constrained SBART (GC-SBART) is proved to further enhance the reconstruction and keep the geometrical and mechanical properties as close to reality as possible. Even if the skin boundary is unknown, the images reconstructed using GC-SBART are found to have better quality overall and around the boundaries as well. GC-SBART is however, takes very long time to achieve the desired results.

In order to improve the operation of SBART and GC-SBART, the algorithm are needed to run using an efficient compiler such as C++. The use of GPU is also under consideration. Since these algorithms will be implemented on the scanner, the results should be real-time and that is the focus of our future work. Also, since the knowing skin boundary improves the reconstruction process and reducing the cost by reducing the number of projections required to achieve high quality image, determining it beforehand is preferable. This can be done by an independent method, then provided for the reconstruction as a priori information. Developing a method for skin boundary detection is also part of the future considerations.

Another issue is that the projections needed for the reconstruction using SBART, are required to be decomposed into individual tissue components, i.e. separated bone, lean and fat projections. Because of DXA physics, only two-material decomposition can be performed. Therefore, there are missing portions of the fat and lean projections that are needed to be estimated to form complete set of projections. To solve this problem, we proposed a multi-projection material decomposition (MPMD) algorithm. In this algorithm, the missing curves are to be estimated by optimizing an objective function with area and summation constraints. All available projections are simultaneously used to satisfy the equal area under the curve constraint among all projections. Fat and lean tissue curves in every projection must also sum to the known soft tissue curve.

The MPMD method gives remarkably better results than the literature method (linear interpolation). Estimating the missing curves and providing a complete set of projections to SBART yields high quality cross sections from as little as five projections and as high as 13 projections. This method however, did not perform that good in case of

cross sections that contains two bones, such as the lower leg. This can be because big portions are missing from every projections. We anticipate that more constraints or assumptions are needed to be added to the objective function in this case. This will be our focus in the future work regarding this project.

Geometrical modeling of bone cross sections are very important to be able to impose different structural and mechanical conditions on this model and study them. The model should be accurate and reliable as possible so we can be certain that the analysis results are applicable. In this dissertation, we provided a method for generating geometrically-equivalent bone models (GEM). This method yielded smooth and accurate models that preserved the geometrical parameters of the original cross section measured from CT image. Finite strip model (FSM) is then generated for the bone shell using shell GEMs. Shell FSMs were then used in a clinical research to test their eligibility. The research examines if the local buckling contributes to the fracture happens under physiologic and traumatic conditions.

The geometrically-equivalent and finite strip modeling provide a very useful tool in transforming bone cross sections from CT images into valid models that can be conveniently used in structural and engineering analyses. Adding the core model to the shell and checking its added effect to the bone strength is the future step to this work.

Several clinical studies can be performed using DXA data and their findings provide a venue for bone research. Here, we presented a study of the effect of hormone therapy accompanied with exercise on bone strength in postmenopausal women. The findings indicate that hormone therapy enhances the effect of exercise on bone strength.

Another study about the relationship between the mechanosensitivity and fractures, indicates that people with fracture incidence have reduced mechanical adaptive response to loads. In future, we plan to perform more studies on 3D bone models, especially stress and buckling analyses in 3D case.

Bibliography

[1] G. W. Jenkins, C. P. Kemnitz, and G. J. Tortora, *Anatomy and Physiology from Science to Life*: John Wiley & Sons, Inc., 2007.

[2] S. Grampp, *Radiology of Osteoporosis*, Second ed.: Springer, 2008.

[3] R. Lindsay, C. Christiansen, T. A. Einhorn, D. M. Hart, S. Ljunghall, C. A. Mautalen, P. J. Meunier, H. Morii, G. R. Mundy, and A. Rapado, "Who are candidates for prevention and treatment for osteoporosis?," *Osteoporosis International,* vol. 7, 1997.

[4] L. J. Melton, 3rd, E. J. Atkinson, M. K. O'Connor, W. M. O'Fallon, and B. L. Riggs, "Bone density and fracture risk in men," *J Bone Miner Res,* vol. 13, pp. 1915-23, Dec 1998.

[5] L. J. Melton, 3rd, E. J. Atkinson, M. K. O'Connor, W. M. O'Fallon, and B. L. Riggs, "Perspective. How many women have osteoporosis?," *J Bone Miner Res.,* vol. 7, pp. 1005-10, 1992.

[6] J. A. Kanis, O. Johnell, A. Oden, I. Sembo, I. Redlund-Johnell, A. Dawson, C. De Laet, and B. Jonsson, "Long-term risk of osteoporotic fracture in Malmo," *Osteoporos Int,* vol. 11, pp. 669-74, 2000.

[7] "Osteoporosis Progress and Promise," ed: NIAMS (National Institute of Arthritis and Musculoskeletal and Skin Diseases), 2011.

[8] K. L. Stone, D. G. Seeley, L. Y. Lui, J. A. Cauley, K. Ensrud, W. S. Browner, M. C. Nevitt, S. R. Cummings, and O. F. R. Group, "BMD at multiple sites and risk of fracture of multiple types: long-term results from the Study of Osteoporotic Fractures," *J Bone Miner Res.,* vol. 18, pp. 1947-54, 2003.

[9] S. A. Wainwright, L. M. Marshall, K. E. Ensrud, J. A. Cauley, D. M. Black, T. A. Hillier, and e. al., "Hip fracture in women without osteoporosis," *J Clin Endocrinol Metab.,* vol. 90, pp. 2787-93, 2005.

[10] R. W. Goulet, S. A. Goldstein, M. J. Ciarelli, J. L. Kuhn, M. B. Brown, and L. A. Feldkamp, "The relationship between the structural and orthogonal compressive properties of trabecular bone," *J Biomech,* vol. 27, pp. 375-89, 1994.

[11] U. Kini and B. N. Nandeesh, "Physiology of Bone Formation, Remodeling, and Metabolism," in *Radionuclide and Hybrid Bone Imaging*

I. Fogelman, G. Gnanasegaran, and H. Wall, Eds., ed: Springer-Verlag Berlin Heidelberg, 2012.

[12] S. L. Bonnick, *Bone Densitometry in Clinical Practice: Applications and Interpretation*, Third Edition ed.: Humana Press, 2010.

[13] S. B. Haymsfield, R. Smith, M. Aulet, B. Bensen, S. Lichtman, J. Wang, and R. N. J. Pierson, "Appendicular skeletal muscle mass: measurement by dual-photon absorptiometry," *Am J Clin Nutr,* vol. 52, pp. 214-8, 1990.

[14] L. Lehmann, R. Alvarez, A. Macovski, W. Brody, N. Pelc, S. Riederer, and A. Hall, "Generalized image combinations in dual KVP digital radiography," *Medical physics,* vol. 8, p. 659, 1981.

[15] "Dual Energy X-Ray Absorptiometry for Bone Mineral Density and Body Composition Assessment," vol. 15, ed: IAEA Human Health Series, 2010.

[16] S. Kolta, A. Le Bras, D. Mitton, V. Bousson, J. A. de Guise, J. Fechtenbaum, J. D. Laredo, C. Roux, and W. Skalli, "Three-dimensional X-ray absorptiometry

(3D-XA): a method for reconstruction of human bones using a dual X-ray absorptiometry device," *Osteoporos Int,* vol. 16, pp. 969-76, Aug 2005.

[17] S. Kolta, S. Quiligotti, A. Ruyssen-Witrand, A. Amido, D. Mitton, A. L. Bras, W. Skalli, and C. Roux, "In vivo 3D reconstruction of human vertebrae with the three-dimensional X-ray absorptiometry (3D-XA) method," *Osteoporos Int,* vol. 19, pp. 185-92, Feb 2008.

[18] C. M. Langton, S. Pisharody, and J. H. Keyak, "Generation of a 3D proximal femur shape from a single projection 2D radiographic image," *Osteoporos Int,* vol. 20, pp. 455-61, Mar 2009.

[19] L. Humbert, T. Whitmarsh, M. De Craene, L. M. del R o Barquero, K. rit scher, R. Schubert, F. Eckstein, T. Link, and A. F. Frangi, "3D reconstruction of both shape and Bone Mineral Density distribution of the femur from DXA images," *IEEE International Symposium on Biomedical Imaging: From Nano to Macro, 2010* pp. 456 - 459, 2010.

[20] C. R. Wilson, "Essentials of bone densitometry for the medical physicist
" presented at the 45th Annual Meeting of American Association of Physicists in Medicine, San Diego, USA., 2003.

[21] H. K. Genant, J. E. Block, P. Steiger, C. C. Glueer, and R. Smith, "Quantitative computed tomography in assessment of osteoporosis," *Semin Nucl Med,* vol. 17, pp. 316-33, Oct 1987.

[22] J. S. Bauer, S. Virmani, and D. K. Mueller, "Quantitative CT to assess bone mineral density as a diagnostic tool for osteoporosis and related fractures," Philips CT Clinical Science, Philips Healthcare, USA2010.

[23] C. E. Cann, H. K. Genant, F. O. Kolb, and B. Ettinger, "Quantitative computed tomography for prediction of vertebral fracture risk," *Bone,* vol. 6, pp. 1-7, 1985.

[24] M. Doblare, J. M. Garcıa, and M. J. Gomez, "Modelling bone tissue fracture and healing: a review," *Engineering Fracture Mechanics,* vol. 71, pp. 1809–1840, 2004.

[25] M. Viceconti, M. Davinelli, F. Taddei, and A. Cappello, "Automatic generation of accurate subject-specific bone finite element models to be used in clinical studies," *J Biomech,* vol. 37, pp. 1597-605, 2004.

[26] A. Templeton, D. Cody, and M. Liebschner, "Updating a 3-D vertebral body finite element model using 2-D images," *Med Eng Phys,* vol. 26, pp. 329-33, 2004.

[27] M. A. Liebschner, D. L. Kopperdahl, W. S. Rosenberg, and T. M. Keaveny, "Finite element modeling of the human thoracolumbar spine," *Spine,* vol. 28, pp. 559-65, 1976.

[28] R. Mootanah, P. Ingle, J. Dowell, K. Cheah, and J. Shelton, "An accurate three dimensional finite element model of the pelvic bone with geometry and material properties retrieved for CT-scan data," presented at the 7th International Symposium on Computer Simulation in Biomechanics, Italy, 2001.

[29] J. Galante, W. Rostoker, and R. D. Ray, "Physical properties of trabecular bone," *Calcified Tissue Research,* vol. 5, pp. 236-246, 1970.

[30] L. J. Gibson, "The mechanical behaviour of cancellous bone," *J Biomech,* vol. 18, pp. 317-28, 1985.

[31] X. E. Guo, "Mechanical properties of cortical bone and cancellous bone tissue," in *Bone Mechanics Handbook*, S. Cowin, Ed., ed Boca Raton, USA: CRC Press, 2001.

[32] J. H. Keyak, I. Y. Lee, and H. B. Skinner, "Correlations between orthogonal mechanical properties and density of trabecular bone: use of different densitometric measures," *J Biomed Mater Res,* vol. 28, pp. 1329-36, 1994.

[33] J. C. Lotz, T. N. Gerhart, and W. C. Hayes, "Mechanical properties of trabecular bone from the proximal femur: a quantitative CT study," *J Comput Assist Tomogr,* vol. 14, pp. 107-14, 1990.

[34] J. C. Lotz, T. N. Gerhart, and W. C. Hayes, "Mechanical properties of metaphyseal bone in the proximal femur," *J Biomech,* vol. 24, pp. 317-29, 1991.

[35] B. Helgason, E. Perilli, E. Schileo, F. Taddei, S. Brynjólfsson, and M. Viceconti, "Mathematical relationships between bone density and mechanical properties: A literature review," *Clinical Biomechanics,* vol. 23, pp. 135–146, 2008.

[36] M. J. Ciarelli, S. A. Goldstein, J. L. Kuhn, D. D. Cody, and M. B. Brown, "Evaluation of orthogonal mechanical properties and density of human trabecular bone from the major metaphyseal regions with materials testing and computed tomography," *J Orthop Res,* vol. 9, pp. 674-82, 1991.

[37] E. F. Morgan, H. H. Bayraktar, and T. M. Keaveny, "Trabecular bone modulus-density relationships depend on anatomic site," *J Biomech,* vol. 36, pp. 897-904, 2003.

[38] Y. K. Cheung and L. G. Tham, "A review of the finite strip method," *Prog. Struct. Eng. Mater.,* vol. 2, pp. 369-375, 2000.

[39] B. W. Schafer and S. Adany, "Buckling analysis of cold-formed steel members using CUFSM: conventional and constrained finite strip methods," presented at the 18¬th International Specialty Conference on Cold-Formed Steel Structures, 2006.

[40] J. Canny, "A Computational Approach to Edge Detection," *IEEE Transactions on Pattern Analysis and Machine Intelligence,* vol. PAMI-8, pp. 679-698, 1986.

[41] F. P. Beer, E. R. Johnston, E. Eisenberg , D. Mazurek, and P. Cornwell *Vector mechanics for engineers* vol. 1: Tata McGraw-Hill Education, 2006.

[42] R. R. Craig, *Mechanics of Materials*: John Wiley & Sons, 1996.

[43] L. Piegl and W. Tiller, *The Nurbs Book*, Second Edition ed.: springer, 1997.

[44] *Handbook of Biomaterial Properties*. London; New York: Chapman & Hall, 1998.

[45] J. Y. Rho, R. B. Ashman, and C. H. Turner, "Young's modulus of trabecular and cortical bone material: ultrasonic and microtensile measurements," *J Biomech,* vol. 26, pp. 111-9, 1993.

[46] F. Aurenhammer, "Voronoi diagrams—a survey of a fundamental geometric data structure," *ACM Computing Surveys (CSUR),* vol. 23, pp. 345-405, 1991.

[47] G. T. Herman and A. Kuba, *Discrete Tomography: Foundations, Algorithms, and Applications*: Birkhauser, 1999.

[48] X. Liu, A. K. Jain, and G. Fichtinger, "Prostate implant reconstruction with discrete tomography," *Med Image Comput Comput Assist Interv,* vol. 10, pp. 734-42, 2007.

[49] T. Wu, A. Stewart, M. Stanton, T. McCauley, W. Phillips, D. B. Kopans, R. H. Moore, J. W. Eberhard, B. Opsahl-Ong, and L. Niklason, "Tomographic mammography using a limited number of low-dose cone-beam projection images," *Medical physics,* vol. 30, p. 365, 2003.

[50] A. Kuba, L. Ruskó, L. Rodek, and Z. Kiss, "Preliminary studies of discrete tomography in neutron imaging," *Nuclear Science, IEEE Transactions on,* vol. 52, pp. 380-385, 2005.

[51] A. C. KAK and M. Slaney, *Principles of Computerized Tomographic Imaging*: SIAM, 2001.

[52] H. Yu and G. Wang, "SART-type image reconstruction from a limited number of projections with the sparsity constraint," *Journal of Biomedical Imaging,* vol. 2010, p. 3, 2010.

[53] Y. Zhang, H. P. Chan, B. Sahiner, J. Wei, M. M. Goodsitt, L. M. Hadjiiski, J. Ge, and C. Zhou, "A comparative study of limited-angle cone-beam reconstruction methods for breast tomosynthesis," *Medical physics,* vol. 33, p. 3781, 2006.

[54] V. Singh, L. Mukherjee, P. M. Dinu, J. Xu, and K. R. Hoffmann, "Limited view CT reconstruction and segmentation via constrained metric labeling," *Computer Vision and Image Understanding,* vol. 112, pp. 67-80, 2008.

[55] K. Batenburg and J. Sijbers, "DART: a fast heuristic algebraic reconstruction algorithm for discrete tomography," in *Proceedings of the IEEE International Conference on Image Processing (ICIP)*, 2007, pp. IV-133-IV-136.

[56] S. Vilsmeier and S. Frhlich, "Method and apparatus for positioning a body for radiation using a position sensor," US 6,611,700 B1, 2003.

[57] S. A. Nehmeh and Y. E. Erdi, "Respiratory motion in positron emission tomography/computed tomography: a review," *Seminars in nuclear medicine,* vol. 38, pp. 167-176, 2008.

[58] Y. Tsunashima, T. Sakae, Y. Shioyama, K. Kagei, T. Terunuma, A. Nohtomi, and Y. Akine, "Correlation between the respiratory waveform measured using a respiratory sensor and 3D tumor motion in gated radiotherapy," *International Journal of Radiation Oncology* Biology* Physics,* vol. 60, pp. 951-958, 2004.

[59] T. M. Buzug, *Computed Tomography: From Photon Statistics to Modern Cone-Beam CT*: Springer, 2008.

[60] K. Batenburg and J. Sijbers, "DART: A Practical Reconstruction Algorithm for Discrete Tomography," *IEEE TRANSACTIONS ON IMAGE PROCESSING,* vol. 20, pp. 2542-2553, 2011.

[61] J. L. Prince and J. M. Links, *Medical Imaging: signals and systems*, 1 ed.: Prentice Hall, 2005.

[62] A. Macovski, *Medical Imaging Systems*: Prentice Hall, 1983.

[63] K. Taguchi and H. Kudo, "Motion compensated fan-beam reconstruction for nonrigid transformation," *IEEE Trans Med Imaging,* vol. 27, pp. 907-17, 2008.

[64] A. E. H. Emery, *Muscular Dystrophy (The Facts)*: Oxford University Press, USA, 2008.

[65] P. Johanson, *Muscular Dystrophy (Genetic and Developmental Diseases and Disorders)*: Rosen Publishing Group, 2008.

[66] R. H. Nord and R. K. Payne, "Body Composition by dual energy X-ray absorptiometry: a review of the technology," *Asian Pacific J Clin Nutr,* vol. 4, pp. 167–171, 1995.

[67] J. A. Sorenson, P. R. Duke, and S. W. Smith, "Simulation studies of dual-energy x-ray absorptiometry," *Med Phys,* vol. 16, pp. 75-80, 1989.

[68] T. F. Lang, "Bone Mineral Assessment of the Axial Skeleton: Technical Aspects," in *Osteoporosis: Pathophysiology and Clinical Management*, R. A. Adler, Ed., 2nd ed: Humana Press, 2011.

[69] ICRU, "Tissue Substitutes in Radiation Dosimetry and Measurement, Report 44 of the International Commission on Radiation Units and Measurements," ed. Bethesda, MD, 1989.

[70] L. A. Lehmann, R. E. Alvarez, A. Macovski, W. R. Brody, N. J. Pelc, S. J. Riederer, and A. L. Hall, "Generalized image combinations in dual KVP digital radiography," *Med Phys,* vol. 8, pp. 659-67, 1981.

[71] E. L. Gingold and B. H. Hasegawa, "Systematic bias in basis material decomposition applied to quantitative dual-energy x-ray imaging," *Med Phys,* vol. 19, pp. 25-33, 1992.

[72] P. T. Boggs, "Sequential Quadratic Programming," *Acta Numerica,* 1996.

[73] M. S. Bazaraa, H. D. Sherali, and C. M. Shetty, *Nonlinear Programming: Theory and Algorithms*, 3rd ed.: Wiley-Interscience, 2006.

[74] K. J. Batenburg and J. Sijbers, "DART: A Practical Reconstruction Algorithm for Discrete Tomography," *IEEE Transactions on Image Processing,* vol. 20, pp. 2542 - 2553, 2011.

[75] S. Ramtani and M. Abdi, "Buckling of adaptive elastic bone-plate: theoretical and numerical investigation," *Biomech Model Mechanobiol,* vol. 3, pp. 200-8, 2005.

[76] D. R. Carter and W. C. Hayes, "Bone Compressive Strength: The Influence of Density and Strain Rate," *Science,* vol. 194, pp. 1174-1176, 1976.

[77] J. C. Lotz, E. J. Cheal, and W. C. Hayes, "Stress distributions within the proximal femur during gait and falls: implications for osteoporotic fracture," *Osteoporos Int,* vol. 5, pp. 252-61, 1995.

[78] R. Muller, S. C. Gerber, and W. C. Hayes, "Micro-compression: a novel technique for the nondestructive assessment of local bone failure," *Technol Health Care,* vol. 6, pp. 433-44, 1998.

[79] V. H. Frankel, "Biomechanics of the hip joint," *Instr Course Lect,* vol. 35, pp. 3-9, 1986.

[80] V. H. Frankel and A. H. Burstein, *Orthopaedic biomechanics: The application of engineering to the musculoskeletal system*: Lea & Febiger (Philadelphia), 1970.

[81] R. D. McLeish and J. Charnley, "Abduction forces in the one-legged stance," *J Biomech,* vol. 3, pp. 191-209, Mar 1970.

[82] N. Ozkaya and M. Nordin, *Fundamentals of Biomechanics: Equilibrium, Motion, and Deformation*, second edition ed.: Springer-Verlag New York, 1999.

[83] M. Trotter and G. C. Gleser, "Estimation of stature from long bones of American Whites and Negroes," *Am J Phys Anthropol,* vol. 10, pp. 463-514, Dec 1952.

[84] P. Stevenson, "On racial differences in stature long bone regression formulae, with special reference to stature reconstruction formulae for the Chinese.," *Biometry,* vol. 21, pp. 303-318, 1929.

[85] A. Angel and H. B. Cisneros, "Technical note: modification of regression equations used to estimate stature in Mesoamerican skeletal remains," *American Journal of Physical Anthropology,* vol. 125, pp. 264-265, 2004.

[86] G. Winter, *Strength of Thin Steel Compression Flanges*, 1947.

[87] M. Pead, R. Suswillo, T. Skerry, S. Vedi, and L. Lanyon, "Increased 3H-uridine levels in osteocytes following a single short period of dynamic bone loadingin vivo," *Calcified tissue international,* vol. 43, pp. 92-96, 1988.

[88] T. M. Skerry, L. E. Lanyon, L. Bitensky, and J. Chayen, "Early strain-related changes in enzyme activity in osteocytes following bone loading in vivo," *Journal of Bone and Mineral Research,* vol. 4, pp. 783-788, 1989.

[89] H. M. Frost, "The Utah paradigm of skeletal physiology: an overview of its insights for bone, cartilage and collagenous tissue organs," *J Bone Miner Metab,* vol. 18, pp. 305-16, 2000.

[90] H. M. Frost, "From Wolff's law to the Utah paradigm: insights about bone physiology and its clinical applications," *Anat Rec,* vol. 262, pp. 398-419, Apr 1 2001.

[91] T. L. Jarvinen, P. Kannus, and H. Sievanen, "Estrogen and bone--a reproductive and locomotive perspective," *J Bone Miner Res,* vol. 18, pp. 1921-31, Nov 2003.

[92] J. Klein-Nulend, J. G. Sterck, C. M. Semeins, P. Lips, M. Joldersma, J. A. Baart, and E. H. Burger, "Donor age and mechanosensitivity of human bone cells," *Osteoporos Int,* vol. 13, pp. 137-46, 2002.

[93] M. Joldersma, J. Klein-Nulend, A. M. Oleksik, I. C. Heyligers, and E. H. Burger, "Estrogen enhances mechanical stress-induced prostaglandin production by bone

cells from elderly women," *Am J Physiol Endocrinol Metab,* vol. 280, pp. E436-42, Mar 2001.

[94] H. L. Jessop, R. F. L. Suswillo, S. C. F. Rawlinson, G. Zaman, K. Lee, V. Das-Gupta, A. A. Pitsillides, and L. E. Lanyon, "Osteoblast-Like Cells From Estrogen Receptor α Knockout Mice Have Deficient Responses to Mechanical Strain," *J Bone Miner Res,* vol. 19, pp. 938-46, 2004.

[95] L. K. Saxon, A. G. Robling, A. B. Castillo, S. Mohan, and C. H. Turner, "The skeletal responsiveness to mechanical loading is enhanced in mice with a null mutation in estrogen receptor-beta," *Am J Physiol Endocrinol Metab,* vol. 293, pp. E484-91, 2007.

[96] T. J. Beck, K. L. Stone, T. L. Oreskovic, M. C. Hochberg, M. C. Nevitt, H. K. Genant, and S. R. Cummings, "Effects of Current and Discontinued Estrogen Replacement Therapy on Hip Structural Geometry: The Study of Osteoporotic Fractures," *J Bone and Mineral Res,* vol. 16, pp. 2103–2110, 2001.

[97] S. L. Greenspan, T. J. Beck, N. M. Resnick, R. Bhattacharya, and R. A. Parker, "Effect of hormone replacement, alendronate, or combination therapy on hip structural geometry: a 3-year, double-blind, placebo-controlled clinical trial," *J Bone Miner Res,* vol. 20, pp. 1525-32, Sep 2005.

[98] K. Uusi-Rasi, T. J. Beck, L. M. Semanick, M. M. Daphtary, G. G. Crans, D. Desaiah, and K. D. Harper, "Structural effects of raloxifene on the proximal femur: results from the multiple outcomes of raloxifene evaluation trial," *Osteoporos Int,* vol. 17, pp. 575-86, 2006.

[99] B. E. Ainsworth, W. L. Haskell, A. S. Leon, D. R. Jacobs, Jr., H. J. Montoye, J. F. Sallis, and R. S. Paffenbarger, Jr., "Compendium of physical activities: classification of energy costs of human physical activities," *Med Sci Sports Exerc,* vol. 25, pp. 71-80, Jan 1993.

[100] R. B. Martin and D. B. Burr, "Non-invasive measurement of long bone cross-sectional moment of inertia by photon absorptiometry," *J Biomech,* vol. 17, pp. 195-201, 1984.

[101] F. Pauwels, "Principles of construction of the lower extremity. Their significance for the stressing of the skeleton of the leg.," in *Biomechanics of the locomotor apparatus: Contributions on the functional anatomy of the locomotor apparatus*, F. Pauwels, Ed., ed: Springer-Verlag (Berlin and New York), 1980, pp. 193-204.

[102] K. F. Janz, S. Rao, H. J. Baumann, and J. L. Schultz, "Measuring children's vertical ground reaction forces with accelerometry during walking, running, and jumping: The Iowa bone development study," *Pediatric Exercise Science,* vol. 15, pp. 34-43, 2003.

[103] J. Bonadio, K. J. Jepsen, M. K. Mansoura, R. Jaenisch, J. L. Kuhn, and S. A. Goldstein, "A murine skeletal adaptation that significantly increases cortical bone mechanical properties. Implications for human skeletal fragility.," *J Clin Invest.,* vol. 92, pp. 1697-1705, 1993.

[104] H. M. Frost, "Bone "mass" and the "mechanostat": a proposal," *Anat Rec,* vol. 219, pp. 1-9., 1987.

[105] C. H. Turner, "Three rules for bone adaptation to mechanical stimuli," *Bone,* vol. 23, pp. 399-407, 1998.

[106] C. Lovejoy, "The Evolution of Human Walking," *Sci Am.,* vol. 259, pp. 118-25, 1988.

[107] P. Mayhew, C. Thomas, J. Clement , N. Loveridge, T. Beck, W. Bonfield, C. Burgoyne, and J. Reeve, "Relation between age, femoral neck cortical stability, and hip fracture risk," *Lancet,* vol. 366, pp. 129-35, 2005.

[108] C. Klotzbuecher, P. Ross, P. Landsman, T. r. Abbott, and M. Berger, "Patients with prior fractures have an increased risk of future fractures: a summary of the literature and statistical synthesis," *J Bone Miner Res.,* vol. 15, pp. 721-39, 2000.

[109] E. Samelson, M. Hannan, Y. Zhang, H. Genant, D. Felson, and D. Kiel, "Incidence and risk factors for vertebral fracture in women and men: 25-year follow-up results from the population-based framingham study*

" *J Bone Miner Res.,* vol. 21, pp. 1207-14, 2006.

[110] B. Khoo, T. Beck, Q. Qiao, Q. Parakh, L. Semanick, R. Prince, K. Singer, and R. Price, "In vivo short-term reproducibility of hip structure analysis variables in comparison with bone mineral density using paired dual-energy x-ray absorptiometry scans from multi-centre clinical trials," *Bone,* vol. 37, pp. 112-21, 2005.

[111] E. Schoenau and H. M. Frost, "The "muscle-bone unit" in children and adolescents," *Calcif Tissue Int,* vol. 70, pp. 405-7., 2002.

[112] E. Schoenau, C. M. Neu, B. Beck, F. Manz, and F. Rauch, "Bone mineral content per muscle cross-sectional area as an index of the functional muscle-bone unit," *J Bone Miner Res,* vol. 17, pp. 1095-101., 2002.

[113] Z. Sumnik, C. Land, S. Coburger, C. Neu, F. Manz, K. Hrach, and E. Schoenau, "The muscle-bone unit in adulthood: influence of sex, height, age and gynecological history on the bone mineral content and muscle cross-sectional area.," *J Musculoskelet Neuronal Interact.,* vol. 6, pp. 195-200, 2006.

Vita

Alia Khaled was born in Giza, Egypt in 1981. She received her B.Sc. and M.Sc. degrees in Systems and Biomedical Engineering from Cairo University, Egypt in 2003 and 2006, respectively. She also received MSE degree in Electrical and Computer Engineering from Johns Hopkins University in 2009. She joined the Electrical and Computer Engineering Ph.D. program at Johns Hopkins University in 2007. Her research interests include signal and image processing, medical imagining, biomechanics, and image reconstruction.